Non-Radial Oscillations in Rotating Intermediate Mass Stars

by

Catherine Lovekin

A Thesis Submitted to Saint Mary's University, Halifax, Nova Scotia in Partial Fulfillment of the Requirements for the Degree of

DOCTOR OF PHILOSOPHY

in

Astronomy

(Department of Astronomy and Physics)

September 8, 2008, Halifax, Nova Scotia

Approved: Dr. R.G. Deupree
Supervisor

Approved: Dr. C.I. Short
Examiner

Approved: Dr. D. Guenther
Examiner

Approved: Dr. A. Cox
External Examiner

Date: August 14, 2008

Canada

Contents

List of Figures

List of Tables

Acknowledgements

Thank you to my parents for all their support, and especially my Dad for invaluable debugging and advice on writing computer code.

I would also like to thank my fellow grad students over the last three years; Jon, Jon, Chris, Nick, Dan, Dave, Mike, Tomomi, Aaron, Kathleen and Bobby. You have all been an amazing source of laughter and support. Thanks especially to Jon, for all the times you've debugged my code for me. A special thank you is also due to Bobby, without whom I would probably not have survived the last six months. Thank you for being a shoulder to cry on, for being so reassuring and having so much faith in me when I was losing mine, and for making sure I was properly fed while writing.

Abstract

Non-Radial Oscillations in Rotating Intermediate Mass Stars

by Catherine Lovekin

In this work I investigate the influence of rotation on pulsation frequencies in upper main sequence stars. I use 2D stellar structure models and a 2D linear adiabatic pulsation code to calculate pulsation frequencies for both uniformly and differentially rotating 10 $M_\odot$ ZAMS models. Current techniques for these calculations often assume that the pulsation mode can be modelled using a single spherical harmonic and that the rotation rate is slow enough for second order perturbation theory approaches to be valid. These techniques require the rotation rate to be small enough to be considered a small linear perturbation. Using my 2D models, I am able to determine independent limits on the rotation rates for which these techniques are valid. These limits depend strongly on the mode and property in question, and range from 50-400 km s^{-1}. In general, uniform rotation decreases both the frequencies and the large separations, but produces increases in the small separations. In differentially rotating models, the frequencies may either increase or decrease, depending on the mode. Since these variations move in opposite directions, it may be possible to constrain the interior angular momentum distribution from stellar pulsations. Unfortunately, the differences are small, and the observational challenges may be insurmountable. Finally, I investigate how the distortion in the shape of the eigenfunction influences photometric mode identification techniques. Increasing rotation increases the variation in photometric mode identification as a function of inclination, with the result that it may be impossible to rule out certain modes.

September 8, 2008

Chapter 1

Introduction

The basic equations governing stellar structure have been understood by astronomers for nearly 100 years. Initially, these equations were studied using models which could be solved semi-analytically, such as polytropes and the Cowling approximation. These remained the primary tools for the study of stellar structure until the development of computers, which made it possible to solve the equations of stellar structure numerically. A more in depth understanding of stellar structure and evolution came rapidly, and very soon the entire life cycle of a star was understood. By 1967, nearly uninterrupted sequences of models covered stellar evolution from the early stages of pre-main sequence contraction through and somewhat beyond shell helium burning, thanks to the work of many researchers (see review in Iben, 1967). Pre-main sequence evolution was studied extensively by Henyey *et al.* (1955); Hayashi (1961) and Iben (1965). Main sequence evolution came to be understood through the work of, among others, Kushwaha (1957) and Kippenhahn *et al.* (1965) for intermediate mass stars (5-7$M_\odot$) and Schwarzschild & Härm (1958) for very massive stars. Evolutionary tracks for lower mass stars were carried out by Hoyle & Schwarzschild (1955) and Iben & Ehrman (1962). Astronomers soon turned to objects with non-solar metallicity, and the first investigations of Population II stars (Demarque, 1960, 1962; Demarque *et al.*, 1972) came soon after the basic structure and evolution of models at solar metallicity began to be understood.

As a result of this work, the structure and evolution of non-rotating spherical stars was well understood for all phases of evolution, and for a wide range of masses and metallicities. Using computers, integrating the stellar structure equations for a spherically symmetric, non-rotating star is straightforward. In a spherically symmetric star the equations of stellar structure can be written in terms of a single independent variable, most commonly the mass interior to a shell of radius r (M_r). Of course, many details remain to be explored, and many challenges remain (eg., convection,

opacities, equation of state).

1.1   Modelling Rotating Stars

Once the basic structure and evolution of spherically symmetric models were reasonably well understood, a new challenge was to understand the physics of rotating stars to the same level of detail. At first glance, this seems easy, because the only new equation introduced to solve for the structure is Poisson's equation for the gravitational potential. In practice, the same physics can behave in different ways (eg., rotational mixing, meridional circulation), and the numerics of the problem become much more difficult. The problem is no longer spherically symmetric, and must be modelled in (at least) two dimensions. Initial attempts at modelling rotating stars treated rotation as a first order perturbation to one dimensional models. For example, Sweet & Roy (1953) calculated first order perturbations to produce a rotating Cowling model. This approach gave some useful answers for slowly rotating models, but breaks down when the ratio of the centrifugal to gravitational forces exceeds 0.29, as the perturbations become too large to be valid under a first order approximation (Sweet & Roy, 1953). Monaghan & Roxburgh (1965) investigated more rapid rotation using polytropes, integrating inward and outward and matching the solutions at some interface. Although a first order approximation is valid in the interior, the outer regions must be treated differently. This allowed them to investigate a wider range of rotation. Although this was important ground work, to truly understand the structure of rotating stars, more realistic structure models are required.

More realistic stellar models of uniformly rotating stars were first used by Roxburgh *et al.* (1965). These models divide the star into two regions, as shown in Figure 1.1. The majority of the mass of the star is concentrated in a spherical central region. This is surrounded by a low density region, in which the gravitational potential is primarily due to the inner region, and appears as a point mass (Roche) potential. Once the potential is known, the equations of stellar structure can be solved as for a spherically symmetric star. This creates a model which can be treated as though it is one dimensional, and is suitable for slowly rotating stars. In principle, this method can be used for conservative rotation laws, but works best for uniformly rotating stars. Conservative rotation laws

require that the rotation rate can be written as the gradient of a potential. One can show (eg. Tassoul, 2000) that this means that Ω, the angular rotation rate, is a function only of distance from the rotation axis ($\varpi = r\sin\theta$, where r is the radius and θ is the polar angle.) These models were subsequently improved to include more realistic opacities and improved nuclear generation rates (Faulkner *et al.*, 1968). This type of model was also used by Sackaman & Anand (1969), this time including convection and the effects of radiation pressure.
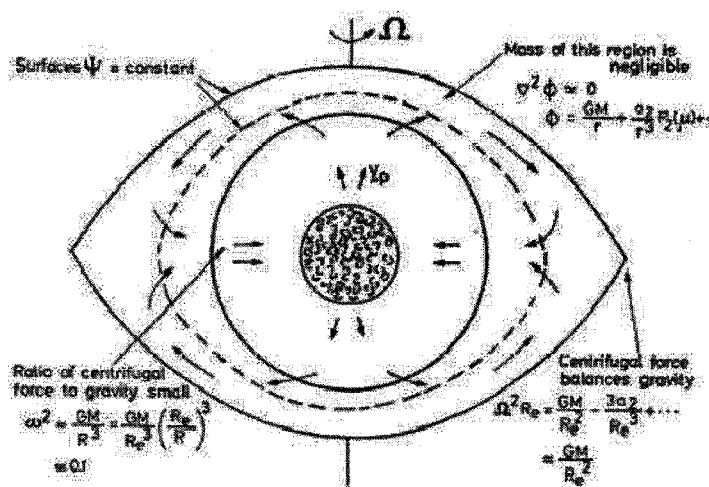
Figure 1.1: The structure of the models used by Roxburgh *et al.* (1965) and Sackaman & Anand (1969). In the outer region, the density is low and the gravitational potential is that of a point mass at the centre of the star. In the inner region, the distortions must be small enough to be handled using a first order approximation. From Roxburgh *et al.* (1965), with kind permission of Springer Science and Business Media.

Two dimensional models of rotating stars have also been produced using the self-consistent field (SCF) method (Ostriker & Mark, 1968). This method uses an iterative approach to solve for hydrostatic equilibrium and the gravitational potential. This method was extended by Jackson (1970) to solve all the equations of stellar structure. As originally formulated, this method encountered

convergence difficulties for models below 9 $M_\odot$, although more recent versions of this seem to avoid the problem (Jackson *et al.*, 2005; MacGregor *et al.*, 2007).

Differential rotation was first investigated by Schwarzschild (1947); Roxburgh (1964); Clement (1969) and Harris & Clement (1971). All of these studies were restricted to relatively slow rotation rates. More rapid rotation, combined with meridional circulation, was investigated by Clement (1972). Further studies on rapidly rotating stars were done throughout the 1970s (Clement, 1974, 1978, 1979).

By the end of the 1970s several methods were in existence for calculating the structure of a rotating star, with some restrictions. Most of the techniques described above require the rotation rate to be relatively modest. These techniques also worked best with either uniform rotation or a modest amount of conservative differential rotation. Some of these were capable of modelling stellar evolution, some were not. The real challenge remained realistic stellar evolution, particularly for more rapidly rotating or extremely differentially rotating models. To do this requires 2D stellar models such as those produced by Deupree (1990, 1995).

The evolution of rotating stars has been studied by Endal & Sophia (1976, 1978, 1979) in a one dimensional framework. They found that over the course of stellar evolution, a rotating star will develop various instabilities, both hydrodynamic and secular. In this work I ignore these instabilities, restricting myself to zero-age main sequence (ZAMS) models. I use the 2D stellar structure and evolution code, ROTORC (Deupree, 1990, 1995, 1998) to calculate both uniformly and differentially rotating models over a variety of rotation rates.

ROTORC is a fully implicit 2.5D stellar evolution code which solves the equations of mass conservation, three components of momentum conservation, energy conservation and Poisson's equation. The 0.5 D means the the model may change in the azimuthal direction, as long as it remains azimuthally symmetric. Instead of M_r as an independent variable, as is done in 1D codes, ROTORC uses the fractional radius, $x = r/R$, and colatitude, θ. In 2D, M_r is an awkward choice for the independent variable, as calculating it would require taking an average over the horizontal density distribution. The equatorial radius, R, is a scale factor determined by forcing the integral of the

density over the volume to equal the total mass, solved simultaneously with the other equations. In the following equations, V_o is the radial flow velocity of the coordinate system. This is set to zero in our ZAMS models.

In two dimensions, the mass conservation equation becomes

$$R\frac{\partial \rho}{\partial t} + (v_r - V_o)\frac{\partial \rho}{\partial x} + \frac{v_\theta}{x}\frac{\partial \rho}{\partial \theta} + \frac{\rho}{x^2}\frac{\partial}{\partial x}(x^2 v_r) + \frac{\rho}{x sin\theta}[(sin\theta)v_\theta] = 0.$$ (1.1)

The three components of momentum are

$$R^2\frac{\partial v_r}{\partial t} + R(v_r - V_o)\frac{\partial v_r}{\partial x} + \frac{Rv_\theta}{x}\frac{\partial v_r}{\partial \theta} + \frac{R}{\rho}\frac{\partial P}{\partial x} + R\frac{\partial \Phi}{\partial x} - R\frac{v_\phi^2}{x} - R\frac{v_\theta^2}{x} = 0$$ (1.2)

$$R^2\frac{\partial v_\theta}{\partial t} + R(v_r - V_o)\frac{\partial v_\theta}{\partial x} + \frac{Rv_\theta}{x}\frac{\partial v_\theta}{\partial \theta} + \frac{R}{\rho x}\frac{\partial P}{\partial \theta} + \frac{R}{x}\frac{\partial \Phi}{\partial \theta} - R\frac{v_\phi^2}{x}cot\theta + R\frac{v_r v_\theta}{x} = 0$$ (1.3)

$$R^2\frac{\partial v_\phi}{\partial t} + R(v_r - V_o)\frac{\partial v_\phi}{\partial x} + \frac{Rv_\theta}{x}\frac{\partial v_\phi}{\partial \theta} + R\frac{v_r v_\phi}{x} + R\frac{v_\theta v_\phi}{x} = 0$$ (1.4)

for the radial (r), colatitudinal (θ) and azimuthal (ϕ) components respectively. The factor of R, which appears in front of every term, allows the code to include eddy viscosity terms. I do not use eddy viscosity, and so these are omitted from the above equations.

The next equation, energy conservation, contains both radiative transport and convective transport in a single equation. This allows ROTORC to carry out both evolution calculations and hydrodynamic simulations.

$$R^2\frac{\partial E}{\partial t} + R(v_r - V_o)\frac{\partial E}{\partial x} + \frac{Rv_\theta}{x}\frac{\partial E}{\partial \theta} - \frac{R^2 P}{\rho x^2}\frac{\partial}{\partial x}(x^2 v_r) - \frac{R^2 P}{\rho x sin\theta}\frac{\partial}{\partial \theta}[(sin\theta)v_\theta]$$
$$-R^2\epsilon - \frac{4\sigma}{3\rho x^2}\frac{\partial}{\partial x}\left(\frac{x^2}{\rho\kappa}\frac{\partial T^4}{\partial x}\right) - \frac{4\sigma}{3\rho x^2 sin\theta}\frac{\partial}{\partial \theta}\left(\frac{sin\theta}{\kappa\rho}\frac{\partial T^4}{\partial \theta}\right) = 0$$ (1.5)

This is done by replacing the opacity by the effective opacity, κ_{eff}, such that

$$\kappa_{eff} = \kappa \cdot \frac{\nabla_{ad}}{\nabla_{rad}} \quad if \quad \nabla_{ad} \geq \nabla_{rad}$$ (1.6)

where κ_{eff} is the opacity used in equation 1.5 and κ is the actual radiative opacity. This approach is only applied in the convective cores, which are the only significant convective regions in the models I will consider.

Poisson's equation in two dimensions becomes

$$\frac{1}{x^2}\frac{\partial}{\partial x}\left(x^2\frac{\partial \Phi}{\partial x}\right) + \frac{1}{x^2 sin\theta}\frac{\partial}{\partial \theta}\left(sin\theta\frac{\partial \Phi}{\partial \theta}\right) - 4\pi G R^2 = 0. \tag{1.7}$$

All three components of the momentum equation are used, but the motion in the azimuthal direction (ϕ) is constrained to be azimuthally symmetric, making ROTORC 2.5 D. These equations are solved using the Henyey method (Henyey *et al.*, 1964).

In ROTORC, the composition is solved simultaneously with the stellar structure equations. This is for stability reasons, since if they are not included, the location of the convective core boundary can fail to converge. For hydrogen, the 2D composition equation is

$$R\frac{\partial X}{\partial t} + (v_r - V_o)\frac{\partial X}{\partial x} + \frac{v_\theta}{x}\frac{\partial X}{\partial \theta} + Rq = 0 \tag{1.8}$$

In this set of equations, P is the pressure, E is the specific internal energy, T is the temperature, ρ is the density, X is the hydrogen mass fraction and q is the nuclear destruction rate of hydrogen. For the ZAMS models I use, $v_r = v_\theta = V_o = 0$, and the time derivatives are set to zero. This renders the composition, mass and azimuthal momentum equations trivial.

Recent work (Gillich *et al.*, 2008) has extended this code to allow for accurate modelling of both uniform rotation and conservative differential rotation laws. The surface of these models is an equipotential surface, defined by

$$\psi = \Phi - \frac{1}{2}v_\phi^2 + \int_0^\varpi \varpi'^2\Omega(\varpi')\frac{d\Omega(\varpi')}{d\varpi'}d\varpi' \tag{1.9}$$

where ψ is the total potential. The integral term is required for nonuniform rotation. The total potential is calculated at the equator for $x = 1$, and the surface at other latitudes is taken to be the

radial zone with the value of ψ which is closest to the equatorial value at each angle. The location of the surface is chosen to be the point where $\tau = 2/3$ in an Eddington grey atmosphere. The local effective temperature is calculated as the value to transmit the flux through the local surface of the star and is calculated at each latitude.

As well as investigating uniformly rotating models, I have computed models with differential rotation, in which the rotation increases inwards. As described in Chapter 3, differential rotation increasing inwards is required if the rotation is to have any significant impact on the core structure. The differential rotation law I use comes from Jackson *et al.* (2005), and is given by

$$\Omega(\varpi) = \frac{\Omega_o}{1 + (a\varpi)^\beta} \tag{1.10}$$

where Ω is the angular velocity, and β is a parameter ranging from 0 (uniform rotation) to 2, the maximum allowed by stability. The parameters a and Ω_o fix the desired surface equatorial velocity and the shape of the rotation law at small ϖ. In our models, we have fixed $a = 2$ and allowed Ω_o to vary.

1.2 Changes in Apparent Stellar Properties with Inclination

The most basic change in stellar models produced by rotation is the distortion introduced by the centrifugal force. The star becomes oblate in shape, and both temperature and emitted flux vary from pole to equator. This effect was first quantified by von Zeipel (1924), who found that the effective temperature is proportional to the fourth root of the effective gravity. As the emitted flux varies across the surface of the star, the flux as seen by an observer will vary with the inclination angle, i, between the rotation axis and the line of sight to the observer. Inclination is not measured directly, but through Doppler broadening of spectral lines, which gives the component of the velocity along the line of sight, $v\sin i$. Although there are techniques which can decouple v and i (Stoeckley, 1968, 1987; Reiners, 2003), these depend on very accurate spectroscopy and accurate synthetic line profiles. The synthetic and observed profiles are compared, and differences are thought to indicate

the details of the rotation. This technique has mixed success. Reiners (2003) found that while the width of the line was related to $v\sin i$, the shape of the line profile depended on v_{eq}. Unfortunately, the distortions are marginal for $v_{eq} \leq 200$ km s^{-1}, so this technique does not appear to work well for slowly rotating stars. There has also been some indication that information about the rotation profile can also be found from this method (Stoeckley, 1987). One of the objectives is to use the line profile to determine the surface angular momentum distribution, and it is not obvious that we can do both from the line profiles.

The variation in flux across the surface, and corresponding dependence on inclination of the flux reaching the observer, makes it difficult to assign an exact effective temperature and luminosity to the star. The magnitude one would observe becomes a function of inclination, and the star would be observed as a point on a curve whose variable is the inclination in the Hertzsprung-Russell Diagram. This effect has been known since the work of Collins (1963, 1966), Hardorp & Strittmatter (1968) and Maeder & Peytremann (1970). Early work studying this included only continuum opacity, with line opacity first included by Maeder & Peytremann (1970). Both structure and atmosphere models have improved up to the most recent work by Linnell & Hubeny (1994); Frémat *et al.* (2005); Lovekin (2005) and Gillich *et al.* (2008).

Recently, Gillich *et al.* (2008) investigated the variation in deduced temperature and luminosity with changing inclination in rotating stars. Using ROTORC, they investigated a wide range of rotation rates for both uniform and differential rotation. This was done using model atmospheres generated by PHOENIX (Hauschildt & Baron, 1999) combined using the spectral synthesis code CLIC (Lovekin, 2005; Lovekin *et al.*, 2006). These codes can be used to calculate either spectral energy distributions (SEDs) or line profiles, including Doppler shift. Gillich (2007) considered both of these, but in this work, I focus on broad band spectral properties, and hence on the SEDs.

Our spectrum synthesis code, CLIC (Lovekin, 2005; Lovekin *et al.*, 2006), takes the variation in radius, temperature, effective gravity, and rotational velocity produced by ROTORC as functions of colatitude and maps this on to a grid on the surface of the stellar model. For each grid zone, the code uses the effective temperature and gravity to determine the four appropriate models from the

log T_{eff}, log g grid produced by PHOENIX (discussed below). CLIC then performs an interpolation among intensities for these four models in temperature, log$g$ and angle relative to the surface normal. This determines the flux emitted from each zone in the direction of the observer. Depending on the mode of operation, these fluxes can either be added directly to produce an SED, or Doppler shifted according to the local surface velocity to create a line profile.

When calculating a SED, CLIC evaluates the following integral

$$F_\lambda = \int_\theta \int_\phi \frac{I_\lambda(\xi(\theta, \phi))}{d^2} dA_{proj} \tag{1.11}$$

where I_λ is the intensity at wavelength λ, $\xi(\theta, \phi)$ is the angle between the local surface normal and the direction to the observer, θ and ϕ are the colatitudinal and azimuthal coordinates respectively, d is the distance, and dA_{proj} is the projected area of each surface element. This integral is performed for inclination angles $i = 0°$ to $90°$ in steps of $10°$.

The first step in this process is to determine ξ. This is complicated by the oblateness of the stellar model, as the surface normal is not in the radial direction. The geometry required to determine ξ is shown in Figure 1.2. The angles in this case are greatly exaggerated. This angle is then used to interpolate between the intensities at the appropriate effective temperature and gravity to find the flux from each zone. This process is repeated for each grid point and wavelength to produce the total flux at each wavelength for the model. Only zones for which ξ is greater than zero are included in the total flux, as zones with $\xi < 0$ do not have a direct line of sight to the observer. This allows me to calculate spectra for a distorted stellar model, provided the range of temperatures and gravities is within the available intensity grid. Another limitation concerns extreme differentially rotating models, which may develop a bulge at mid-latitudes. In this case, zones near the pole which have $\xi > 0$ may be blocked by regions of the star at lower latitude. CLIC currently has no way to account for such a configuration.

CLIC has also been extended to calculate Doppler shifted line profiles, as was done by Gillich (2007). In SED mode, CLIC falls into the category of 'embarrassingly parallel' problems, as each wavelength is independent of the others. Thus, a range of wavelengths can be sent to each pro-
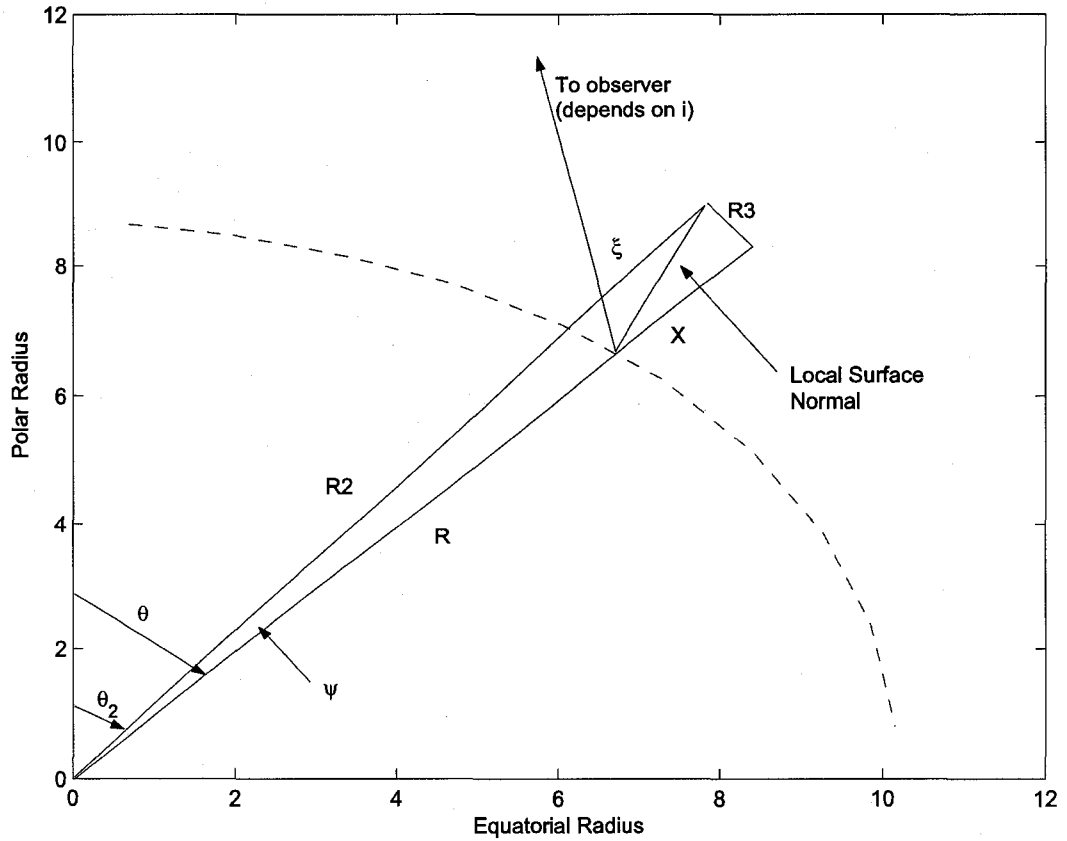
Figure 1.2: The geometry required to determine the normal to the surface. The distance from the model centre to the surface at the location of interest is R. This vector is extended by an arbitrary length X. R3 is perpendicular to X and is bounded by the vector X and the surface normal. The vector R2 runs from the model centre to the intersection of R3 with the surface normal. Note that the vector in the direction of the observer could have a component outside the plane of the image.

cessor and the integral computed without any further interaction with the other processors. When calculating a line profile, the assumption of wavelength independence is no longer justified and the wavelengths are now coupled. In line mode, CLIC circumvents this coupling by creating a series of wavelength bins. Each contribution to the flux at each wavelength is processed individually and shifted into the appropriate bin. At the end of the calculation, the master processor sums all of the results into a single line profile. Aside from the treatment of the Doppler broadening, the calculation proceeds as for the SEDs. The only other difference between the two modes is the range of wavelengths that can be processed. In SED mode, CLIC can calculate an arbitrary number of wavelengths. In line mode, the code is restricted by the number of bins (currently 4000), so the wavelength range is restricted by the desired output wavelength spacing. Of course, this can be changed as needed.

I have used results from the PHOENIX code (Hauschildt & Baron, 1999) as one of the inputs to CLIC. PHOENIX provides intensity as a function of angle to the surface normal of the plane parallel atmosphere at each wavelength. We calculate atmospheres at a range of temperatures and log$g$. More details on PHOENIX can be found in Chapter 4. Here I will summarize some of the assumptions used in the atmospheric models we use.

In LTE matter and radiation are assumed to be in equilibrium with each other locally, and the energy levels of the elements are populated according to Maxwell-Boltzmann statistics. NonLTE does not make this assumption, and calculates the population of the energy levels with the temperature of the matter decoupled from the radiation temperature. LTE can be a reasonable approximation in some cases, but in the hot stars we consider, the departures from LTE can be large, so we use nonLTE atmospheres with as many elements as possible included in nonLTE. The version of PHOENIX we use was extended by Short *et al.* (1999) to allow at least two ionization stages of 24 elements and the lowest six ionization stages of the 20 most important elements. This includes many of the Fe group elements. Much of the work done with PHOENIX has focused on solar type stars, as in Short & Hauschildt (2005). Gillich *et al.* (2008) encountered difficulties converging models with temperatures below 24000 K, largely due to convergence difficulties with silicon and phosphorus. In

this work then, these elements are treated in LTE for model atmospheres with temperatures below 24000 K.

Another potential significant factor in the atmospheres of hot stars is the contribution of radiation pressure to hydrostatic equilibrium. When radiation pressure is included, gas pressure decreases to maintain hydrostatic equilibrium. Gillich (2007) found that for temperatures greater than 24000 K, radiation pressure became so large that the gas pressure dropped below zero in some atmospheric layers. This is, of course, unphysical, and causes PHOENIX to fail. Fortunately, radiatively driven winds are not critically important for the B stars considered here, so, following Gillich (2007), we do not include radiation pressure in our atmospheric models.

Our atmosphere models are computed using the plane-parallel approximation, in which the atmosphere is treated as a semi-infinite slab in which the physical parameters vary only with depth. This assumption is valid provided the horizontal mean path of the photons is small compared to the horizontal distance over which the atmosphere changes, and if the thickness of the atmosphere is much less than the stellar radius. These assumptions are generally true, as the radius of the star is so large that the surface is effectively flat and the atmosphere will appear homogeneous horizontally. For our rotating models, these assumptions are least true at the equator, where the effective gravity is lowest and the curvature of the surface is greatest. However, the equator is also where the local effective temperature, and hence the flux, is lowest, and the equatorial region is not expected to contribute significantly to the integrated flux of the star once the curvature becomes large. Even if the plane-parallel approximation begins to break down at this point, the effect on the overall SED is expected to be small.

Using CLIC, model atmospheres from PHOENIX and the rotating stellar structure from ROTORC, I can calculate individual lines or spectra as a function of inclination. Lovekin (2005) found that it was not possible to determine inclination from the overall spectrum of a star. Gillich (2007) used the same methods to calculate inclination curves, which determine the range of deduced effective temperature and luminosity for a given mass and rotation rate. Even if the spectra cannot be used to determine the inclination, it is important to be aware of this variation and take it it into consideration when

interpreting photometric observations. This is another way in which rapid rotation complicates our ability to understand rapidly rotating stars.

1.3 Stellar Pulsation

Pulsations in the β Cephei stars were first detected over 100 years ago, with the prototype discovered by Frost (1902). There are currently close to 100 known β Cephei type pulsators, all of which are thought to be main sequence objects (Stankov & Handler, 2005). These stars usually have one or more periods close to the radial fundamental mode or the first nonradial p-mode, with periods on the order of several hours. They are generally considered to be early B type stars, with a peak in their mass distribution at 12 $M_\odot$. The definition of this class was first stated by Lesh & Aizenman (1978): "These stars have the same short period for their light variation and radial velocity variation." Stankov & Handler (2005) have suggested a somewhat clearer definition: "The β Cephei stars are massive nonsupergiant variable stars with spectral type O or B whose light, radial velocity and/or line profile variations are caused by low-order pressure and gravity mode pulsations." In practice, this means a β Cephei star shows convincing evidence for more than one period too short to be consistent with rotation or binarity. Although the majority of β Cephei stars are probably slow rotators (average $v\sin i \approx 100$ km s^{-1},) projected rotation rates as high as 300 km s^{-1} are observed (Stankov & Handler, 2005). Rapidly rotating β Cephei stars have also been detected by Balona & Evers (1999). Based on these results, 10 $M_\odot$ ZAMS models, while at the low edge of the mass range, seem reasonable for comparison with β Cephei stars. Our rotation range, 0 km s^{-1} to 400 km s^{-1} also seems realistic.

Although β Cephei stars have been known to pulsate for over 100 years, it is relatively recently that their pulsation mechanism has been understood. In fact Cox (1976) listed eight different proposed mechanisms for the β Cephei pulsation. Of these, all but two failed to account for the observed variability. Of the two successful mechanisms, one does not agree with observations. The other mechanism (an instability produced by a rapidly rotating core), while successful, seemed very contrived. A few years later, the first indications that the pulsation could be driven by the edge of

the He$^+$ zone were found by Stellingwerf (1978, 1979). This was soon followed by the prediction that the β Cephei stars should occupy an instability strip roughly parallel to the main sequence, and that they should obey a period-luminosity (Π-L) relation (Cox & Stellingwerf, 1979). Pulsation frequencies and stability analysis were performed by Saio & Cox (1980). However, Lee & Osaki (1982) argued that the He$^+$-ionization mechanism suggested by Stellingwerf (1978) was not large enough to destabilize the stars as a whole. Instead, they argued the pulsations were driven by line opacity. Not until the OPAL opacities (Iglesias *et al.*, 1987, 1990; Iglesias & Rogers, 1996) were released was it determined that β Cephei pulsations were driven by the κ mechanism, with a bump in opacity at T $\sim$ 2 x 10^5 K (Moskalik & Dziembowski, 1992; Dziembowski *et al.*, 1993). Their theoretical instability strip agreed closely with the observed location of these pulsators.

As indicated above, stars can pulsate either radially or non-radially. Radial pulsations are the simplest form, and the entire star expands and contracts in unison. In non-radial pulsations, the amplitude varies across the surface of the star. The details of this were first worked out by Pekeris (1938) for uniform density, nonrotating models. At the time this work was undertaken, it was believed that non-radial modes were unlikely to be observed, as they were thought to be subject significantly more damping than radial modes. Pekeris (1938) showed that these assumptions do not hold for g-modes or the low order p-modes. Unlike the radial modes, models exist which are unstable for all values of the adiabatic index, γ. These results indicated that stars could pulsate non-radially, and these modes must be considered. These results were extended to non-rotating polytropes by Cowling (1941).

Various other analytic techniques for determining pulsation frequencies were investigated over the next few decades, for example the variational principle (Chandrasekhar & Lebovitz, 1962; Chandrasekhar, 1964). In this technique, the pulsation equations are written as a linear operator, L, acting on the eigenfunction, such that

$$\sigma\xi = L\xi \qquad (1.12)$$

which can be solved for the frequency by mulitplying both sides by ξ^*, the complex conjugate of ξ,

and integrating over the volume (V)

$$\sigma = \frac{\int \xi^* L \xi dV}{\int \xi * \xi dV}. \tag{1.13}$$

The correct values of σ occur when this equation is minimized. This is done by assuming a form of ξ with dependence on some number of parameters. The equation can then be minimized by setting the derivative with respect to each parameter to zero, solving for the parameters, and using the resulting ξ to evaluate σ.

The first numerical solution of the pulsation equations was done by Hurley, Roberts & Wright (1966). Again, this was restricted to non-rotating polytropes. The development of non-radial pulsation analysis is discussed in more detail in Chapter 2.

Non-radial modes fall into two general classifications; the p-modes and the g-modes. The p-modes are predominantly radial modes, with relatively large Eulerian density and pressure perturbations (δP and $\delta \rho$). These modes are sometimes called *acoustic* modes. The g-modes are predominantly transverse modes, and generally have small variations in δP and $\delta \rho$. They are often called *gravity* modes. In this work, I focus on p-modes in upper main sequence stars. These modes are classified according to three quantum numbers; the radial order n, the angular degree l and the azimuthal order m. When discussing the p-modes, they are classified by their l value, followed by p_n, where n is the number of radial nodes. Hence, the $l = 2$, $n = 3$ p-mode would be given as the $l = 2$, p_3 mode. The $n = 0$ mode is a special case, called the f mode. The radial modes are also a special case, as they are neither p nor g-modes. The radial fundamental is called the F mode, and the overtones are classified as 1H, 2H, 3H, etc. The azimuthal order, m, is generally not given for any mode, as in non-rotating stars, all modes with the same l and m are degenerate. Rotation does lift this degeneracy, an effect called mode splitting, which can be calculated using first order perturbation theory. In this work, I restrict myself to axisymmetric modes ($m = 0$), so mode splitting is not considered.

The non-radial pulsation equations are derived from the three components of the linearized momentum equation, the linearized mass conservation equation, the adiabatic relation between the density and pressure, and the linearized Poisson's equation. The variables in these equations are the

three components of the linearized displacements (ξ_r, ξ_θ and ξ_ϕ), the linear (Eulerian) perturbations to the density ($\delta\rho$) and pressure (δP), and the linear perturbation of the gravitational potential ($\delta\phi$):

$$\sigma^2 \rho \vec{\xi} + 2i\sigma\rho(\vec{\xi} \times \vec{\Omega}) + \vec{g}\,\delta\rho - \vec{\nabla}\delta P + \rho\vec{\nabla}\delta\phi = 0 \tag{1.14}$$

$$\delta\rho = -\vec{\nabla}\cdot\rho\vec{\xi} \tag{1.15}$$

$$\delta P = -\Gamma_1 P\vec{\nabla}\cdot\vec{\xi} - \vec{\xi}\cdot\vec{\nabla}P \tag{1.16}$$

$$\nabla^2\delta\phi = -4\pi G\delta\rho. \tag{1.17}$$

In the above equations, $\vec{g}$ is the effective gravity, given by the gradient of the total potential, Ψ.

Hurley, Roberts & Wright (1966) derived two equations to describe the behaviour of the pulsational perturbations. One equation was taking $\vec{\nabla}\cdot$ the momentum equation, and the other was obtained by taking $\vec{r}\cdot(\vec{\nabla}\times$ the momentum equation). With suitable vector manipulation, one can show that the angular derivatives of these two equations are in the form of the angular parts of ∇^2, for which the solution is the spherical harmonic, Y_l^m. The angular dependence of the equations gives terms depending on l since

$$\nabla^2 Y_l^m = \frac{l(l+1)}{r^2}Y_l^m \tag{1.18}$$

This allows the angular and radial terms to separate, and the radial (ξ_r) and angular (ξ_θ) components of the displacement of the final solution have the form

$$\xi_r(r,\theta) = r^{l-1}XY_l^m(cos\theta) \tag{1.19}$$
$$\xi_\theta(r,\theta) = Q\frac{dY_l^m(cos\theta)}{d\theta}$$

where X and Q are functions only of r. The radial and angular components of the solution depend on r and θ, and the amplitude of the mode varies horizontally, along the surface from the pole to equator. This horizontal variation introduces a non-spherical component to the model structure at any particular instant during the pulsation, even in non-rotating stars.

As stated, I have restricted my studies to axisymmetric ($m = 0$) modes, which reduces the spherical harmonics to Legendre Polynomials. Theoretically, there is no limit to the order l of a pulsation mode, and indeed, modes of high l have been observed in the Sun. In more distant stars, practical limitations restrict which modes are observable. Photometrically, amplitude changes are expected to cancel out when integrated across the disk for $l \gtrsim 3$. As l increases, the amplitude of the mode decreases, and the modes become more difficult to detect both photometrically and spectroscopically.

Pulsations in rotating stars are often calculated using a perturbation approach, as developed by Saio (1981). This approach treats the rotation as a perturbation to the structure of the star,

$$r = a[1 + \epsilon(a, \theta, \phi)].\tag{1.20}$$

The linearized pulsation equations are then expanded in a series in powers of the rotation rate. The zeroth power gives the nonrotating eigenvalues and eigenfunctions, and each eigenfunction can be written in terms of a single spherical harmonic. For higher order powers the coefficients of the perturbations in the pulsation equations, which depend on the static model, will have latitudinal dependence if the model is rotating. As discussed above, pulsation also introduces a non-spherical component to the stellar structure, even in the case of a non-rotating star. Both the variation from pulsation and rotation can be expressed in terms of spherical harmonics, and when combined, the eigenfunctions will depend on the products of spherical harmonics. Using recursion relations, these can be rewritten in terms of a sum of spherical harmonics. For this technique to work the structural perturbations, and hence the rotation rate, must be small. Unfortunately, it is not clear exactly how small is small enough. In Chapter 2, I present one of the first investigations into the limits of second order perturbation theory.

My pulsation calculations have been performed using the 2D linear adiabatic pulsation code NRO (Clement, 1998). This code solves the linearized non-radial pulsation equations on a 2D grid within the star. One of the primary advantages of this code is that it uses a 2D stellar structure model, such as that produced by ROTORC, and thus does not depend on approximations such as perturbation

theory or von Zeipel's law (von Zeipel, 1924). To solve the pulsation equations, NRO transforms the physical variables into ones which are smooth and well defined on the boundaries (the origin, the surface, the rotation axis, and equatorial plane). These variables are

$$
\begin{aligned}
y_1 &= \frac{\xi_r}{r^{|k-1|}sin^m\theta}, \\
y_2 &= \frac{\xi_\theta}{r^{|k-1|}}sin^{|m-1|}\theta cos\theta, \\
y_3 &= \frac{\delta p}{r^k sin^m\theta}, \\
y_4 &= \frac{\delta\phi}{r^k sin^m\theta}, \\
y_5 &= \partial_r y_4.
\end{aligned}
\tag{1.21}
$$

The solutions for ξ_r, ξ_θ, pressure perturbation (δp) and perturbation to the gravitational potential ($\delta\phi$) make up the eigenfunction. The exponent k comes from one possible expression for the pressure perturbation

$$
\delta P(r,\theta,\phi;l,m,n) = e^{im\phi}\sum_{k=m}^{\inf}A_k^m(r,\theta;n,l)r^k
\tag{1.22}
$$

In this expression, rather than writing the pressure perturbation as a mixture of spherical harmonics, it is written as a mixture of radial components of different exponent k (Clement, 1998). Solutions are then found for a range of k by direct finite difference integration on the grid. This should not be confused with the order of the mode (l), which is not a unique number for pulsations of a rotating star, and is used by NRO only to determine the *parity* of the mode. Odd modes are scaled by a factor of $cos\theta$, making them symmetric, so the same method of solution can be used either way. The factor of $cos\theta$ is then added back in at the end of the calculation. The equations are solved along N radial lines, one for each spherical harmonic included. For axisymmetric modes, NRO includes the first N even spherical harmonics, starting with $l = 0$. If the mode is odd, the scaling by $cos\theta$ makes this equivalent to the first N odd harmonics, starting with $l = 1$.

The solution to the linear, nonadiabatic, nonradial pulsation equations can be written in terms of the y_is. Using the r component of motion as an example, each of the four equations has the

following form:

$$r\partial_r y_3 = A_1 y_1 + A_2 y_2 + A_3 y_3 + A_c y_c \qquad (1.23)$$

where the coefficients in this case are given by

$$
\begin{aligned}
A_1 &= (\sigma^2 - 4\Omega^2 sin^2\theta) r^K, \\[2mm]
A_2 &= -4\Omega^2 r^K sin^M\theta cos^2\theta, \\[2mm]
A_3 &= -(k + m\alpha) \\[2mm]
A_c &= -\frac{A g_r}{c^2}.
\end{aligned}
\qquad (1.24)
$$

In this, $K = 2\delta_{k0}$ and $M = 2\delta_{m0}$, $\alpha = 2\Omega/\sigma$, and $A = c^2 dln\rho/d\phi$ - 1. This form of the equation of motion introduces a new variable,

$$y_c = g_r r^K y_1 + g_s r^K sin^M\theta cos^2\theta y_2 + r y_3 + r y_4. \qquad (1.25)$$

where $g_s = g_\theta/(sin\theta cos\theta)$.

Writing the other equations (θ component of equation of motion, the divergence equation, and Poisson's equation) in the same format gives expressions for $\partial_r y_i$ ($i = 1..5$) which can be integrated in radius at all angles. The coefficients of these equations form a band diagonal matrix, which can be solved directly. In NRO, the matrix is not solved directly, but uses a technique which allows for more rapid solution. These equations are integrated both inward from the surface and outward from the centre. The inward and outward integrations are required to be continuous at some intermediate fitting surface. Once given an initial guess of the eigenfrequency, the coefficients in all the equations have been evaluated, a matrix of the coefficients around the fitting surface can be inverted to solve for the perturbations at the fitting surface and the radial zone either directly above or below. These values are then used to step through the mesh both backwards and forwards, solving for the remaining perturbations. One of the perturbations is forced to be a constant, typically $\delta r/r = 1$ at some point on the surface, to eliminate the trivial solution (zero everywhere). This leaves one

unused condition, making the problem an eigenvalue problem. This unused condition can be used to evaluate a discriminant. This discriminant will be satisfied (equal to zero) if an eigenvalue has been located. In practice, the code steps through frequency space looking for zero crossings of the discriminant. Once the crossing has been found, the code will iterate on the frequency until the discriminant is zero within some specified tolerance, returning the eigenfrequency and eigenfunction of the mode. This method does sometimes miss frequencies when two modes are quite close together. This can usually be remedied by reducing the frequency step size.

Although adiabatic oscillations like those calculated by NRO are somewhat unrealistic, they do provide a good dynamical description of pulsating stars (Cox, 1980). Linear adiabatic theory can give good pulsation periods and amplitudes relative to some normalization point within the star. However, it cannot tell us anything about the thermal behavior of the star. Linear adiabatic theory will not tell us the amplitudes of the pulsations. Also, the linear adiabatic approximation will not tell us anything about whether a perturbation will grow or decay. To determine if a given mode can be excited in a star requires nonadiabatic calculations. Nonadiabatic oscillations are mathematically more difficult, as there are five complex variables (vs. four real variables in the adiabatic case.) Nonadiabatic calculations have been performed by several groups, including Saio & Cox (1980); Pesnell (1990); Dupret (2001); Dupret *et al.* (2002) and Suran (2007), but these do not include realistic modelling of rotation.

To determine the general properties of the mode, adiabatic calculations are usually sufficient. Although there are many nonadiabatic, nonradial pulsation codes in existence, none has the flexibility to model the range of rotation rates that can be modelled using NRO.

1.4   Current Work

When trying to understand a pulsating, rotating star, observations can give us some basic quantities, assuming high resolution spectra are available: the metallicity ([Fe/H]), the acceleration due to gravity (g), the effective temperature (T_{eff}), the luminosity (L) and $v\sin i$. If the star is pulsating, the collection of pulsation frequencies and amplitudes may be available. Based on these observational

quantities, we must come up with a theoretical understanding of the star. As discussed above, the uncertainty in the effective temperature and luminosity produced by changing the inclination of the star, as well as our inability to reliably disentangle rotational velocity and inclination makes this interpretation significantly more difficult.

In order to better understand rotating stars, I have used a 2D stellar pulsation code and a 2D stellar structure code capable of modelling both uniform and differential rotation. Using the stellar structure code, ROTORC, I have calculated the variation in radius, local effective temperature and gravity as a function of both r and θ for 10 $M_\odot$ zero-age main sequence (ZAMS) models without resorting to approximations such as von Zeipel's law or assuming the surface distortion has a specific form. This gives me both 2D stellar structure models and the radius, local effective temperature and effective gravity as a function of colatitude. The stellar structure models are then used by NRO to calculate pulsation frequencies and the horizontal and radial Lagrangian displacements. Because I am not interested in a specific stellar model, I use the pulsation frequencies normalized by the frequency of the non-rotating model to investigate the trends with rotation rate. As NRO also gives the horizontal variation of the eigenfunction, I can use this to calculate the physical perturbations and apply them to the radius, local effective temperature and effective gravity found using ROTORC. This perturbed stellar surface structure is used by CLIC to calculate spectra of a star deformed by both rotation and pulsation as a function of inclination, without making any assumptions about gravity darkening. Since the pulsations vary with time, I calculate two spectra for each model, one at maximum compression and one at maximum expansion. Using these spectra I can test some current assumptions about photometric mode identification techniques.

In this work, I have investigated the relationships between rotation and pulsation. In Chapter 2, I investigate the numerics of calculating pulsations in rotating stars. Pulsations are most commonly calculated using a perturbation theory approximation. As discussed, this assumes that the rotation rate is small, so the structural perturbations introduced by rotation can be modelled as a first order linear perturbation. As discussed briefly above, this assumption is not always true, but the limitations on this method have not previously been well defined.

Once I established how many spherical harmonics are required to accurately model pulsation in rapidly rotating stars, I turn my attention to the trends rotation produces in the pulsation frequencies in both uniformly and differentially rotating stellar models. These results are discussed in Chapter 3.

Of course, for any of the observed pulsation frequencies to be useful tools in understanding the stellar structure, we must be able to identify them. In Chapter 4, I examine photometric mode identification techniques, and how these are affected by rotation.

While asteroseismology does have the potential to greatly increase our understanding of stars, it is important to understand all the factors that can influence the frequencies when trying to interpret them. There are many factors to be taken into account when studying rotating stars, such as composition, age, convective overshooting, as well as rotation rate and angular momentum distribution, not all of which are considered here. If we are to use observed pulsation frequencies to constrain rotating stars, mode identification is very important. Mode identification is sometimes estimated based on the calculated frequency of the radial fundamental mode for a model with the same luminosity and effective temperature as the observed star. As discussed above, the observed luminosity and effective temperature of a rotating star is not unique, but depends on the angle of inclination at which the star is observed. This complicates determination of the fundamental parameters of the star. Rotation will change the pulsation frequencies, and this must also be taken into account. If we want to identify a mode based on its observed effective temperature, luminosity and pulsation frequency, it is important to understand how these are affected by rotation. Rotation also distorts the horizontal variation of the mode, increasing the contribution from higher order spherical harmonics. Current photometric mode identification techniques rely on models using pure spherical harmonics, and using these models to identify modes in rotating stars may result in misidentification of the modes. In this work, I investigate some of these rotational effects in an effort to improve our understanding of rotation in pulsating stars.

Chapter 2

Pulsations of Uniformly Rotating Stars[1]

Radial and nonradial oscillations offer the opportunity to investigate the interior properties of stars. We use 2D stellar models and a 2D finite difference integration of the linear pulsation equations to calculate non-radial oscillations. This approach allows us to directly calculate the pulsation modes for a distorted rotating star without treating the rotation as a perturbation. We are also able to express the finite difference solution in the horizontal direction as a sum of multiple spherical harmonics for any given mode. Using these methods, we have investigated the effects of rotation and the number of spherical harmonics on the calculated eigenfrequencies and eigenfunctions and compared the results to perturbation theory. In slowly rotating stars, current methods work well, and we show that the eigenfunction can be accurately modelled using 2nd order perturbation theory and a single spherical harmonic. We use 10 $M_\odot$ models with velocities ranging from 0 to 420 km s^{-1} (0.89 Ω_c) and examine low order p modes. We find that one spherical harmonic remains reasonable up to a rotation rate around 300km s^{-1} (0.69 Ω_c) for the radial fundamental mode, but can fail at rotation rates as low as 90 km s^{-1}(0.23 Ω_c) for the 2H mode or $l = 2$ p$_2$ mode, based on the eigenfrequencies alone. Depending on the mode in question, a single spherical harmonic may fail at lower rotation rates if the shape of the eigenfunction is taken into consideration. Perturbation theory, in contrast, remains valid up to relatively high rotation rates for most modes. We find the lowest failure surface equatorial velocity is 120 km s^{-1}(0.30 Ω_c) for the $l = 2$ p$_2$ mode, but failure velocities between 240 and 300 km s^{-1}(0.58-0.69 Ω_c)are more typical.

---

[1]The contents of this chapter originally appeared as Lovekin, C.C. & Deupree, R.G. 2008. The Astrophysical Journal, 679, 1499

2.1 Introduction

Stellar oscillations provide us with a probe of the internal structure of stars. The oscillations depend on the stellar structure, and are modified by factors such as rotation, magnetic fields and tidal forces. In theory, if we have sufficiently accurate parameters for a star, we can produce models which will constrain the internal structure. Unfortunately, due to the uncertainties on the temperature and luminosity of the star and the large number of free parameters (mass, rotation rate, age, etc.), this process is much more difficult in practise. Accurate modelling also requires enough observed modes to actually place some constraints on the star. The more modes available, the tighter these constraints can be, but we must be sure that all the modes used are real. Artificial or extraneous modes can make it impossible to produce a matching model. In recent years, the number of stars with multiple modes has increased greatly, both thanks to the ground based networks such as STEPHI (Belmonte *et al.*, 1993) and WET (Nather *et al.*, 1990), as well as space-based observations such as WIRE (Hacking *et al.*, 1999) and MOST (Walker *et al.*, 2003). Current and upcoming space missions, such as Kepler (Basri, Borucki & Koch, 2005) and COROT (Baglin & *et al.*, 2001) are expected to further increase the number of multiperiodic variables. Unfortunately, the theory still lags behind the observations, particularly for rotating stars.

The first investigation of non-radial oscillations was undertaken by Pekeris (1938). This paper derived the linearized, adiabatic equations for nonradial oscillations of non-rotating stars, and then solved the equations for models of uniform density. At the time, it was assumed that non-radial modes would be subject to significant amounts of damping, more so than the purely radial modes. As a result, non-radial oscillations were generally not studied extensively. However, these assumptions do not hold for the low order p modes or for all g modes. Unlike radial oscillations, which are unstable only for $\gamma < \frac{4}{3}$, there are some non-radial oscillations of a uniform density sphere which are unstable for all values of γ. Based on these results, Pekeris (1938) concluded that non-radial oscillations must be considered. Using these results, Cowling (1941) calculated the periods of non-radial oscillations for non-rotating polytropes.

Before the advent of numerical techniques, these equations had to be solved using analytical

methods. Much of this work was done by Chandrasekhar, who explored the variational principle as a method of solving the linear adiabatic pulsation equations (Chandrasekhar & Lebovitz, 1962; Chandrasekhar, 1964). This method depends on an arbitrary guess at the form of the eigenfunction, and the resulting eigenvalues depend on the guess. Fortunately, even marginal guesses at the eigenfunction can produce reasonable results for the eigenfrequencies with this method. This approach is largely unused today, as it has been superseded by computational work using more efficient and accurate numerical techniques.

The first direct numerical integration of the linearized equations for nonradial oscillations was performed by Hurley, Roberts & Wright (1966). In this work, they calculated oscillation frequencies for non-rotating, polytropic stellar models, for comparison with the earlier analytic approaches discussed above. Although they restricted themselves to polytropic models, their method can relatively easily be extended to more realistic stellar models.

All of these approaches depend on perturbations to a non-rotating (i.e., spherical) stellar model. In this case, the calculations are relatively straight forward. Rotation, even moderate rotation, can significantly complicate the calculation, and many attempts have been made over the years to solve the problem with varying degrees of success. These will be discussed in more detail below.

In spherical stars, the solution to the linear adiabatic pulsation equations is separable, and can be written as

$$\xi_r = X(r)Y_l^m(\theta, \phi) \tag{2.1}$$

The angular variation can be characterized by a single spherical harmonic, Y_l^m, and both l and m are legitimate quantum numbers. Once a star becomes distorted, e.g. through tidal effects or rotation, the situation becomes more complex and several problems arise. The eigenfunction can no longer strictly be described by a single spherical harmonic, and thus l is no longer a valid quantum number. As long as the star remains axisymmetric, m remains valid. As well as changes in the structure of the eigenfunction, the pulsation frequencies themselves will change. It is this change in eigenfrequency that has been of most interest to researchers, particularly as observations continue to find more and more rotating and pulsating stars, many with multiple frequencies.

One of the earlier attempts to solve the linear adiabatic pulsation equations for rotating stars was made by Chandrasekhar & Lebovitz (1962), who applied the virial theorem to rotating incompressible fluids. The variational principle has also been extended to include slowly rotating stars by Clement (1964, 1965). Further attempts at improving the method through a better choice of basis vectors have also been made by Clement (1986). Although the variational equations themselves can be applied to a star with an arbitrary rotation rate (Ω), the method also depends on being able to model the structure of the star. The structure of rotating stars has generally been modelled as a perturbation to the non-rotating structure. Because the structural perturbations are limited to modelling slowly rotating stars, the variational method was also limited to slowly rotating stars.

An approach used more frequently now is based on a perturbation approach, as developed by Saio (1981). In this framework, the rotation is treated as a perturbation on the structure of the star. For example, the radial location in a rotating model would be written as

$$r = a[1 + \epsilon(a, \theta, \phi)] \qquad (2.2)$$

The linearized pulsation equations are expanded in a series in powers of the rotation rate. The zeroth power merely gives the nonrotating eigenvalues and eigenfunctions. Each non-rotating eigenfunction can be written in terms of a single spherical harmonic, and the eigenfunction can be characterized by three quantum numbers relating to the number of radial nodes and the two angular quantum numbers, l and m, associated with the spherical harmonics. The first order in the expansion in powers of the rotation rate lifts the $2l+1$ fold degeneracy in the eigenvalues, while the eigenfunctions that correspond to this order are still characterized by a single spherical harmonic.

We note that this will not be true in the general set of linearized pulsation equations of a rotating star. The coefficients of the perturbations in the pulsation equations, composed of terms based on the static rotating model, will have latitudinal variations. The eigenfunctions will also have a latitudinal variation, so that the equations can be expressed as products of spherical harmonics, which in turn can be written as sums of spherical harmonics through appropriate recursion relations.

In perturbation theory the rotation rate is assumed to be much smaller than the frequency being

calculated. This keeps the rotational perturbation small so that including only the first one or two terms in the power series expansion is satisfactory. Small is, of course a vague term, and it is not clear how small is small. Based on discussions at the Workshop on the Future of Asteroseismology held in Vienna in September 2006, estimates of the limiting rotation rate ranged from 50 to 300 km s^{-1}. Of course, the limiting surface equatorial velocity will be dependent on the mass of the star in question.

Efforts to more accurately include rotation have been developed. These methods require 2D calculations, so are more time consuming and complex. As a result, previous studies have all faced restrictions and limitations. For example, Espinosa *et al.* (2004) calculated the adiabatic oscillations of rapidly rotating stars with uniform rotation. To succeed, they applied the Cowling approximation, neglected the Coriolis force and neglected the Brunt-Väisälä frequency in the adiabatic equation. Yoshida & Eriguchi (2001) have modelled quasi-radial modes at a range of rotation rates in rotating neutron stars using the relativistic Cowling approximation. Other methods, such as that employed by Lignières, Rieutord & Reese (2006) and Reese, Lignières & Rieutord (2006) have fewer physical restrictions, but have so far been restricted to explorations of polytropic models.

The effects discussed in this paper are only expected to matter for stars undergoing moderate to rapid rotation. A recent study of OB stars (Daflon, 2007) found that 50 % of OB stars have rotation velocities greater than 100 km s^{-1}. At least some of these stars are expected to pulsate. For example, β Cephei-type pulsations have been detected in Spica (Sterken, Jerzykiewicz & Manfroid, 1986), which is also rotating with a vsin$i \sim 160$ km s^{-1}. For the β Cephei stars as a category, the projected rotation velocities range from 0 to 300 km s^{-1} (Stankov & Handler, 2005). The average vsin$i \sim 100$ km s^{-1}, although this could be a selection effect, as the highest amplitude pulsators are the more slowly rotating stars. Another category of pulsating stars, the low amplitude δ Scuti stars (LADS) have been detected with vsin$i$ up to 250-300 km s^{-1} (Breger, 2007). The models we consider in this paper are 10 M$_\odot$ ZAMS models with solar (Z = 0.02) metallicity. Although β Cephei stars have evolved along the main sequence, the trends produced by these models should be comparable to typical β Cephei stars. One effect which may be important is mode bumping, which will appear

in real β Cephei stars, but does not appear in our unevolved models. Our models include uniform rotation at rates from 0 to 0.89 Ω_c. Our method also allows us to consider differential rotation, and this will be discussed in a future paper.

Clement (1998) has developed a finite difference method for directly evaluating the eigenfunctions on a 2D grid. In this paper, we combine this method with 2D stellar models produced by ROTORC (Deupree, 1990, 1995). The combination of these two approaches bypasses many of the restrictions faced by previous approaches. Our numerical methods and models are described in more detail in §2.2. We investigate the effects of rotation on the calculated eigenfrequencies (§2.3) and eigenfunctions (§2.4), with the aim of establishing the range of validity of modes calculated with one spherical harmonic. In §2.5 we compare our results with those predicted by second order perturbation theory.

2.2 Method

Our stellar models are calculated using the 2D stellar evolution code ROTORC (Deupree, 1990, 1995), allowing us to self-consistently model the surface and structure of the star for rotation rates from zero up to near-critical rotation. In this paper we focus on uniformly rotating 10 $M_\odot$ZAMS models with X=0.7, Z=0.02. We use the OPAL opacities (Iglesias & Rogers, 1996) and equation of state (Rogers, Swenson & Iglesias, 1996) in these calculations. These models are fully 2D, with 10 angular zones from pole to equator and 349 radial zones. The small number of angular zones is acceptable for these models because the horizontal variation is so smooth. We have computed a few rotating models using 20 angular zones and find differences in the horizontal variation of the density to be only about 0.1%. The pulsation code uses Fourier transform interpolation to convert from our angular zoning to its own angular zoning, and we feel the ROTORC angular zoning is not a major source of error in the calculations and use 10 angular zone models in this work.

The location of the surface of the stellar model is found by assuming it lies on an equipotential surface. The value of the equipotential is determined by the value of the total potential in the angular zone which has the largest radius (for uniformly rotating models, this is always at the equator). The radial zone which has this value of the total potential is found at each angular zone and the surface

boundary conditions applied there. One source of inaccuracy is that a radial zone is either completely interior or exterior to the surface, so that the surface is defined as the radial zone interface which is closest to the location of the equipotential. Our rotating models are made by imposing a surface equatorial velocity and an internal angular momentum distribution (in this case, uniform rotation) and allowing the surface to change as needed. This can lead to small differences between the imposed (target) surface equatorial velocity and the actual surface equatorial velocity, typically less than 2 km s^{-1}. Throughout this paper, we refer to models by the target surface equatorial velocity.

For our pulsation calculations, we use the non-radial oscillation code (NRO) developed by Clement (1998). Instead of expressing the solution as a sum of spherical harmonics, the code solves the perturbation equations on a 2D spherical grid. In ROTORC, the stellar model is defined on a spherical polar grid, with the stellar surface location being an equipotential surface as discussed above. NRO transforms this into a model defined on surfaces of constant density. The 2D nature of the code allows us to account for the effect of the centrifugal distortion, but the Coriolis force is neglected. The pressure perturbation can be expressed in two ways:

$$\delta P(r,\theta,\phi;l,m,n) \;=\; e^{im\phi} \sum_{l=m}^{\infty} a_l^m(r;n,l) P_l^m(cos\theta)$$

$$\text{or}$$

$$=\; e^{im\phi} \sum_{k=m}^{\infty} A_k^m(r,\theta;n,l) r^k.$$

In this code, the second form of this general equation is used. Keeping this general solution in mind, the linear adiabatic pulsation equations can be recast using 5 variables, related to the radial and angular velocity perturbation, the pressure and gravity perturbations, and the radial derivative of the gravitational perturbation. These variables are defined as follows:

$$y_1 \equiv \frac{\xi_r}{r^{k-1}sin^m\theta},$$

$$y_2 \equiv \frac{\xi_\theta}{r^{k-1}sin^{m-1}\theta cos\theta},$$

$$y_3 \equiv \frac{\delta p}{r^k sin^m\theta}, \qquad\qquad (2.3)$$

$$y_4 \equiv \frac{\delta\phi}{r^k sin^m\theta},$$

$$\text{and } y_5 \equiv \partial_r y_4$$

where k is the radial exponent, m is the azimuthal quantum number, and $k = 0$ and $m = 0$ are special cases. If k-1 and m-1 are negative, they are replaced by 1. This form of the equations allows the boundary conditions to be applied while avoiding singularities. With these variables, the relevant linearized equations can be expressed in the general form

$$\partial_r y_i = f(y_i, \partial_r y_{j\neq i}, \partial_\theta y_i) \qquad\qquad (2.4)$$

The full form of the equations and their derivations can be found in Clement (1998).

The coefficients of the finite difference expressions of the equations (as represented in Eqn. 2.4) covering the entire 2D grid can be put in a band diagonal matrix. Each element of this band diagonal matrix is itself a matrix, containing the coefficients at each zone in the 2D grid. The solution of the finite difference pulsation equations proceeds in two steps, from the center outwards and from the surface inwards. Each integration also requires an initial guess of the eigenfrequency.

The inward and outward integrations of the eigenfunctions are required to be continuous at some intermediate fitting surface. Once all of the coefficients of the equations have been evaluated, a subset of the matrix, including the fitting surface and the radial zones immediately surrounding it can be inverted to solve for the perturbations at the fitting surface and the radial zone either directly above or below the fitting surface. These values can then be used to step inwards and outwards through the mesh to solve for the perturbations throughout the rest of the grid. At some point on

the surface,one of the perturbations is forced to be a constant (typically, $\delta r/r = 1$) to eliminate the trivial solution of all variables being zero everywhere. As a result of this, there is one condition that has not been used. This can be used to evaluate a discriminant, which will only be satisfied (equal to zero) if an eigenvalue has been located. Using this method, we can step through eigenfrequency space, solving the matrix, evaluating the discriminant and looking for zero crossings. Once a crossing has been located, various convergence schemes can be used to calculate the exact eigenfrequency. This method can miss frequencies when two eigenfrequencies are quite close together, although these can usually be avoided by reducing the frequency step size.

The code can include up to nine angular zones in the solution for the eigenfunctions, performing one radial integration for each angle included. At the end of the calculation, the solution is known at N angles, which can subsequently be decomposed into the contributions of individual spherical harmonics. This is done with Fourier transforms, which transform the N discrete points into coefficients of the appropriate cosine series. After some algebraic manipulation, this series is converted into a Legendre series, which gives us the relative contribution of each Y_l^m(or Legendre Polynomial for the case where $m = 0$). Because each radial integration contains angular derivatives, also evaluated using finite differencing, the resultant coupling among spherical harmonics arises naturally. Thus, this method allows us to directly model the coupling among spherical harmonics in a single pulsation mode for rotating stars in a natural way.

Because l is not a legitimate quantum number for rotating models, specifying l is not necessary. In the pulsation code the input value of l is used to specify the parity of the mode, not the exact value of l. Based on the parity of l, the code includes the first k even or odd basis functions, where k is the input value of the number of angular zones to be included. We limit ourselves to small input values of l because those are expected to be the most easily observable. We also restrict ourselves to axisymmetric modes (m=0), although this is not a constraint intrinsic to the method. We have also restricted ourselves to modes with small radial quantum number (n).

Because l is no longer a valid quantum number, we need a new designation for mode identification. We have chosen to identify the mode with a quantum number, l_0, which is the value of l of the mode

in the nonrotating model to which a given mode can be traced back. This tracing back is based on examining both the eigenfrequency and the angular shape of the eigenfunction (the modes at different radial quantum number are easy to resolve; no mode bumping is exhibited in these ZAMS models). This is quite easy up to moderate rotation rates because one spherical harmonic tends to dominate. This method fails for rotation velocities above 420 km s^{-1} because no spherical harmonic dominates. For rotation velocities above 360 km s^{-1}, we find this method becomes somewhat uncertain and produces an irregular progression in frequency for some modes. We thus consider the pulsation properties for models up to 420 km s^{-1}, but regard the frequencies above 360 km s^{-1} as uncertain. Although we only consider pulsation up to 420 km s^{-1}, our static models go up to near critical rotation.

2.3   Accuracy of Eigenfrequencies

As described in the above section, NRO, combined with 2D structure models from ROTORC, allows us to calculate the eigenfrequencies for a rotating star without making any *a priori* assumptions about the structure of the star. The method of solution of NRO allows for the inclusion of multiple spherical harmonics. As a result, we can calculate eigenfunctions for distorted stars including the coupling between spherical harmonics. In contrast most current calculations and observations generally assume that pulsation frequencies and observed modes can be characterized by a single spherical harmonic. It is therefore of interest to determine at what surface equatorial velocity modes can no longer be adequately described by a single spherical harmonic.

One of the issues arising out of the following discussion is where a difference between two calculated modes becomes significant. Both ground-based and space-based observations continue to improve, as new projects are continuously launched (figuratively and literally). As an example, COROT is expected to measure frequencies to a precision of less than 0.01μHz for the long runs, and better than 0.065μHz for a faint object during short runs (Michel *et al.*, 2007). Based on these numbers, calculated frequencies do not need to change by much to be outside the observational uncertainties. However, we must ask ourselves whether it is reasonable to expect our models to

match this accuracy. The linear adiabatic pulsation code uses 10^{-6} as the convergence criterion on the discriminant described in §2.2. There will be other sources of error on the final eigenfrequency, such as from the finite difference representation of the pulsation equations. Neglecting these other sources of error, NRO converges modes to an accuracy of about 10^{-6}, or about 0.001 μHz, more than sufficient to match the predicted COROT accuracy. However, there are inaccuracies that result from the finite difference zoning in the static models. When we change the surface equatorial velocity from one model to the next, we change the distribution of material in the star, although the radial zoning (fractional surface equatorial radius) remains the same. The changes become larger as the rotation rate increases. This is equivalent to changing the radial zoning, which experience from the early calculations of linear radial pulsation indicated has a sensitivity on about the one percent level. We have also fairly dramatically rezoned a couple of our models and found that the eigenfrequencies changed on about the one percent level, or about 8.5 μHz for our models. The higher radial order p modes are slightly more affected because the outer layers of the model, where the gradients of model quantities are steeper, play a larger role. Clearly, our ability to measure observational frequencies to high precision is irrelevant until models improve enough to match them. Until then, for changes induced by rotational effects to be considered significant, they must be larger than our model uncertainties.

Another uncertainty consideration is the angular resolution of our pulsation calculations. As described above, the number of spherical harmonics used in NRO determines the number of radial integrations performed. There are several ways we can assess the effects of this changing angular resolution. Firstly, we would expect the slowly rotating modes to be relatively unaffected by angular resolution. This is indeed what we find. In the case of slow rotation, the coefficients for the higher order spherical harmonics are small, typically not more than a percent up to 120 km s^{-1}. Over these same rotation ranges, we also expect the frequency to be relatively unaffected by angular resolution, and this is indeed what we find. The frequencies shown in Fig. 2.1 differ by less than a quarter of a percent over this rotation range.

In the majority of our plots, we show our results as a function of surface equatorial velocity, as

Table 2.1: Summary of model parameters

target v_{eq} (km s^{-1})	actual v_{eq}	Ω (x10^{-3}) (s^{-1})	Ω/Ω_c	R_{eq} (R$_\odot$)	R_p/R_{eq}	T_p/T_{eq}
0	0	0.0000	0.00	3.973	1.000	1.000
10	9.97	0.0036	0.03	3.973	1.000	1.000
30	29.91	0.0108	0.08	3.976	0.999	1.001
50	49.85	0.0180	0.13	3.981	0.997	1.003
90	89.72	0.0322	0.23	4.000	0.991	1.008
120	119.63	0.0428	0.30	4.021	0.986	1.013
150	149.54	0.0531	0.37	4.048	0.977	1.021
180	179.45	0.0632	0.44	4.082	0.967	1.032
210	209.35	0.0729	0.51	4.125	0.953	1.051
240	239.26	0.0824	0.58	4.175	0.924	1.065
270	269.17	0.0913	0.64	4.237	0.908	1.082
300	299.08	0.0998	0.69	4.307	0.887	1.100
330	328.98	0.1076	0.76	4.393	0.866	1.125
360	358.89	0.1148	0.81	4.491	0.846	1.149
390	388.80	0.1215	0.85	4.600	0.821	1.173
420	418.71	0.1272	0.89	4.729	0.796	1.203

this is the unit most easily compared to observations. However, for comparison with other models, it is more useful to show results as a function of angular rotation rate expressed as a fraction of critical rotation (Ω/Ω_c). Critical rotation was calculated using a model rotating at 575 km s^{-1}, with an equatorial radius of 5.792 R$_\odot$. This model is quite close to critical rotation. We have summarized the conversion between these two frames of reference, as well as some other parameters of our models in Table 2.1.

2.3.1 Frequency Changes

The simplest way to determine where the assumption that a single Y_l^m can be used is to compare the frequencies as calculated with different numbers of spherical harmonics. This is illustrated in Fig. 2.1, which shows the normalized frequencies for the $l_0 = 0$ and $l_0 = 1$ fundamental modes, as calculated using 1, 2, 3 and 6 spherical harmonics. At some cut off surface equatorial velocity, the eigenfunctions calculated with only a few spherical harmonics begin to deviate significantly from those calculated using 6 spherical harmonics. For the $l_0 = 0$ mode, the frequencies calculated with 1 spherical harmonic are in reasonably good agreement to quite high velocities, remaining within approximately 0.5 % of the frequencies calculated with more spherical harmonics. The $l_0 = 1$ mode as calculated with 1 spherical harmonic rapidly diverges from the frequencies as calculated with

multiple basis functions. In this case, the single spherical harmonic frequency reaches a difference of 1% at a surface equatorial velocity of 210 km s^{-1}(0.51 Ω_c).

Similar results are found for higher order modes. These results are summarized in Table 2.2. To determine the location of the cut off surface equatorial velocity, as described above, we take a difference of 1% to be significant, as discussed in §2.3.

Although the periods are expected to change depending on the details of the model, period differences and ratios are expected to be much more stable. Hence, in the next two sections we will consider the large separation and period ratios of our frequency calculations.

2.3.2 Large Separations

We have studied the large separation between the $n = 0$, 1 and 2 modes for $l_0 = 0$-3. We have calculated the large separations in the usual way

$$\Delta\nu = \nu_{l,n+1} - \nu_{l,n}. \tag{2.5}$$

Before comparing these for the effects of the number of spherical harmonics included, we need to account for rotation, which can change the large separation by changing the model structure. First, we normalize these large separations with respect to the non-rotating model

$$D\nu = \Delta\nu(v = 0) - \Delta\nu(v). \tag{2.6}$$

We can then use these normalized large separations to look for the effects of the number of spherical harmonics included in the calculation (N)

$$\mathcal{D}\nu = D\nu_N - D\nu_{N=6}. \tag{2.7}$$

For this calculation, we have assumed that the frequencies calculated with 6 Y_l^ms are closest to the true pulsation frequencies, so the smaller the differences between this and other calculations, the
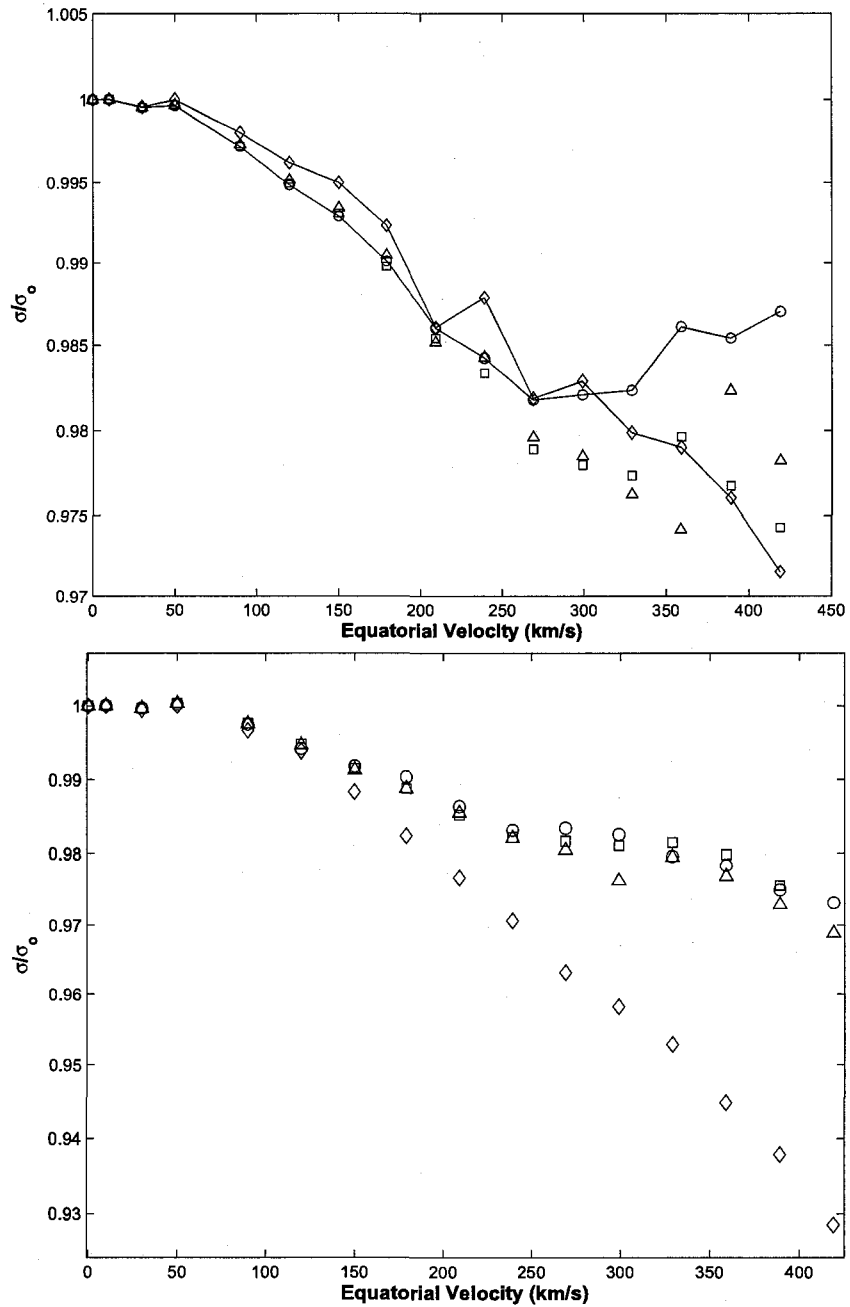
Figure 2.1: The frequency changes as a function of surface equatorial velocity for the fundamental mode for $l_0 = 0$ (top) and $l_0 = 1$ (bottom). Frequencies shown are calculated with ($\Diamond$) - 1 Y_l^m, $\circ$ - 2 Y_l^m, ($\Box$) - 3 Y_l^m, and ($\triangle$) - 6 Y_l^m.
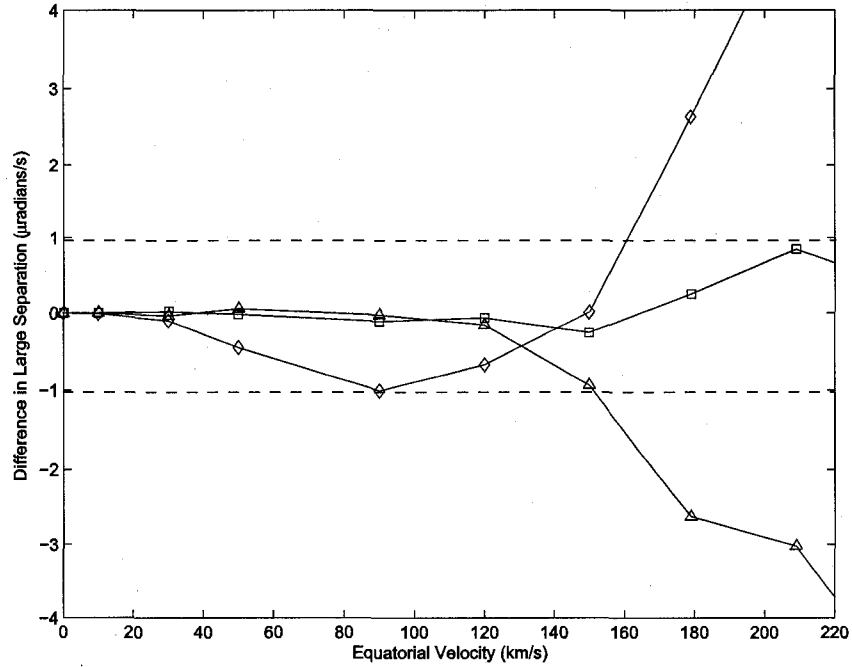
Figure 2.2: The relative large separation (Eqn. 2.7) as a function of surface equatorial velocity between the $l_0 = 0$ fundamental and first harmonic. Symbols are as follows: ($\Diamond$) - 1 spherical harmonic, ($\triangle$) - 2 spherical harmonics ($\circ$) - 3 spherical harmonics, all relative to 6 spherical harmonics. Dashed lines indicate the significance criterion adopted in this work.

more accurate the smaller number of spherical harmonics. This is illustrated in Fig. 2.2, which shows the results of Eqn. 2.7 as a function of surface equatorial velocity for the separation between the l_0 = 0 fundamental and first harmonic.

The uncertainty in the theoretical calculations of large separation is inversely proportional to the uncertainty in the radius of the stellar model in question. Taking the uncertainty in radius to be the size of one radial zone, for our models, this is approximately 0.04μHz. Observationally, large separations are well determined for solar type stars, with uncertainties typically less than 1μHz. As a conservative estimate, we have chosen 1μHz as our significance criterion, as shown by the dashed lines in Fig. 2.2. It should be noted that once the large separations with 1 and 2 spherical harmonics begin to diverge, they do so quite rapidly, so unless the cut off criterion is appreciably smaller ($\lesssim$ 0.5μHz), the cut off surface equatorial velocity is not an extremely sensitive function of the cut off criterion. The limiting rotational velocities estimated using the large separations are summarized in

column 4 of Table 2.2.

2.4 Accuracy of Eigenfunctions

So far, the limiting rotation rates entered in Table 2.2 have been for the $l_0 = 0$ and 1 modes only. This is a result of the way spherical harmonics are included in NRO. To calculate the $l_0 = 2$ mode, for example, the code will select even Y_l^ms starting with $l_0 = 0$, so at least 2 Y_l^ms are required. This is true for any mode with $l_0 \geq 2$. As a result, we cannot directly compare eigenfrequencies calculated with several spherical harmonics to those calculated with a single spherical harmonic.

We can still compare the eigenfunctions, and in this section this is what we will do. One of the advantages of including several spherical harmonics is the ability to study the effect of rotation not only on the eigenfrequencies, but also on the shapes of the eigenfunctions. For a non-rotating object, regardless of how many spherical harmonics are included, the eigenfunction remains a pure Y_l^m, as it should. As the rotation rate increases, neighbouring spherical harmonics begin to contribute progressively more to the shape of the eigenfunction. These effects could be quite important for mode identification, and need to be considered in rapidly rotating stars. One technique for mode identification uses the pulsation amplitudes in different colors as determined by single spherical harmonics. With rotation significantly altering the modes by coupling spherical harmonics, it could alter these color amplitudes and change the mode identification. We find that the effects of the coupling can become significant, even at very moderate rotation rates.

We have used a combination of the value of the eigenfrequency and the angular variation of the eigenfunction at the surface to identify the modes as we progressed from one rotating model to the next. Of course, with the finite difference approach the angular variation of the eigenfunction can vary with depth. Fig. 2.3 presents this variation for several rotation rates for the radial fundamental mode. Each plot contains the variation at several different depths. As expected, the variation with depth is small for slowly rotating models, and grows as the rotation rate increases. Despite this growth in variation, the profile remains recognizably the same until the most rapid rotation rate presented. This occurs at a rotation rate at which we are already beginning to have trouble tracing
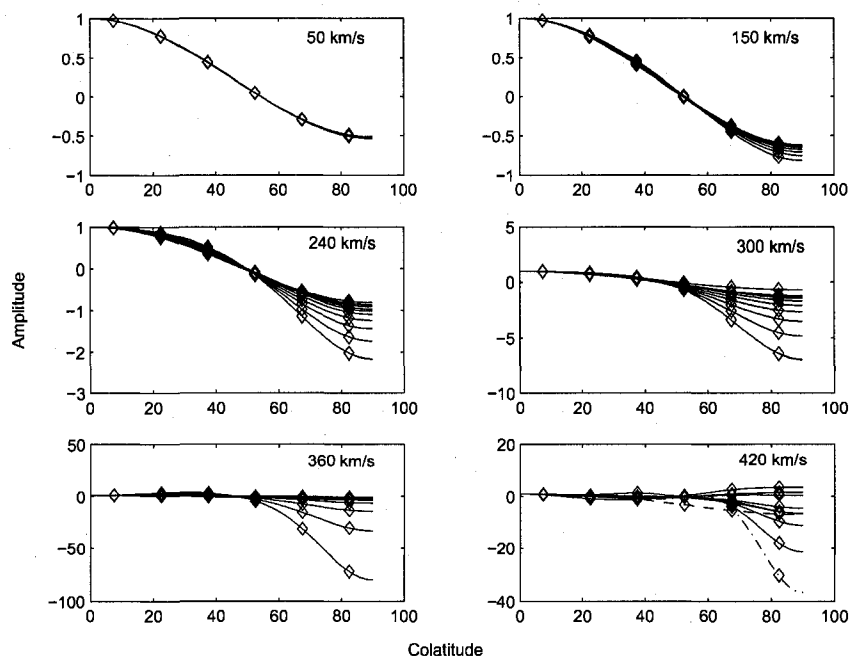
Figure 2.3: Variation in the radial eigenfunction for the $l_0 = 2$ mode as a function of colatitude at various depths (fractional surface equatorial radii of approximately 0.1, 0.2, 0.3, 0.4, 0.5, 0.6, 0.7, 0.8, 0.9 and 1.0) for models rotating at 50, 150, 240, 300, 360, and 420 km s^{-1}. The convective boundary is located between 0.2 and 0.3 R_{eq}. The variation at each depth is normalized to be unity at the pole for purposes of comparison. The variation is smallest at the center of the star, and increases towards the surface. On the plot of the 420 km s^{-1}, the layer closest to the center is indicated with a dashed line, and the layer closest to the surface is indicated by a dot-dashed line. In most cases, 420 km s^{-1} is the most rapidly rotating model considered, as mode identification becomes difficult.

the modes from one rotation rate to the next as we have previously mentioned.

Fig. 2.4 shows the angular variation at the surface in the radial component of the $l_0 = 0$ fundamental mode at 90 and 270 km s^{-1}. At 90 km s^{-1}, the distorting effects of rotation are negligible, although the differences are visible. In contrast, by 270 km s^{-1} the differences between the numbers of spherical harmonics are quite significant, and 1 spherical harmonic is clearly not sufficient to model the horizontal shape of the mode. In comparison, the eigen*frequencies* were considered to be accurate using one spherical harmonic up to rotation rates of 300 km s^{-1}. This highlights the truism that even marginal eigenfunctions can give reasonable eigenfrequencies. By 270 km s^{-1}, the mode no longer looks like an $l = 0$ mode, nor even an $l = 2$, but is beginning to distinctly show the characteristics of the $l = 4$ contribution. These two velocities were chosen based on the relative
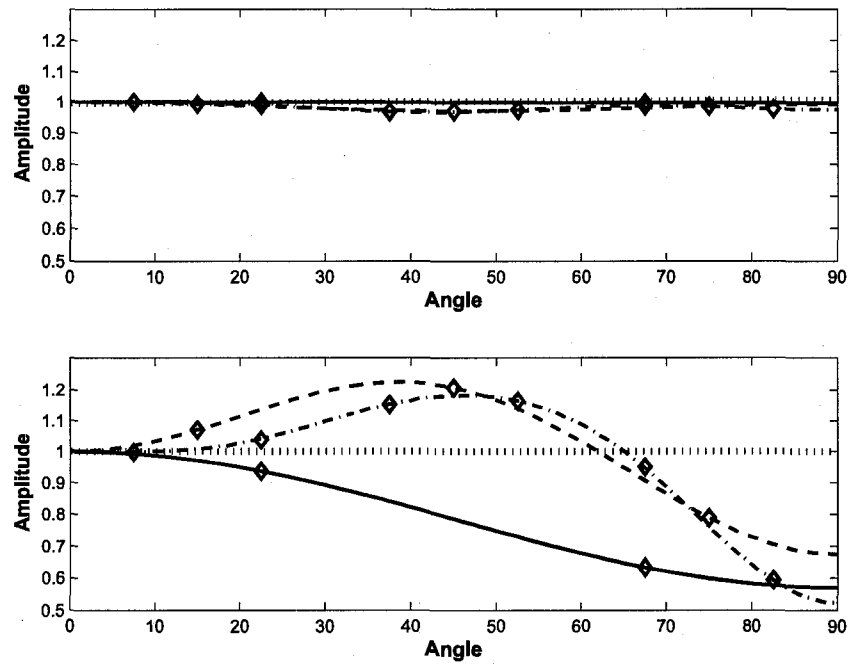
Figure 2.4: Angular variation in the radial eigenfunction for the radial fundamental mode of a model rotating at 90 (top) and 270 km s^{-1}(bottom). On both plots, the shape of the eigenfunction is shown as calculated using 1 (dotted), 2 (solid), 3 (dashed) and 6 (dot-dashed) spherical harmonics.
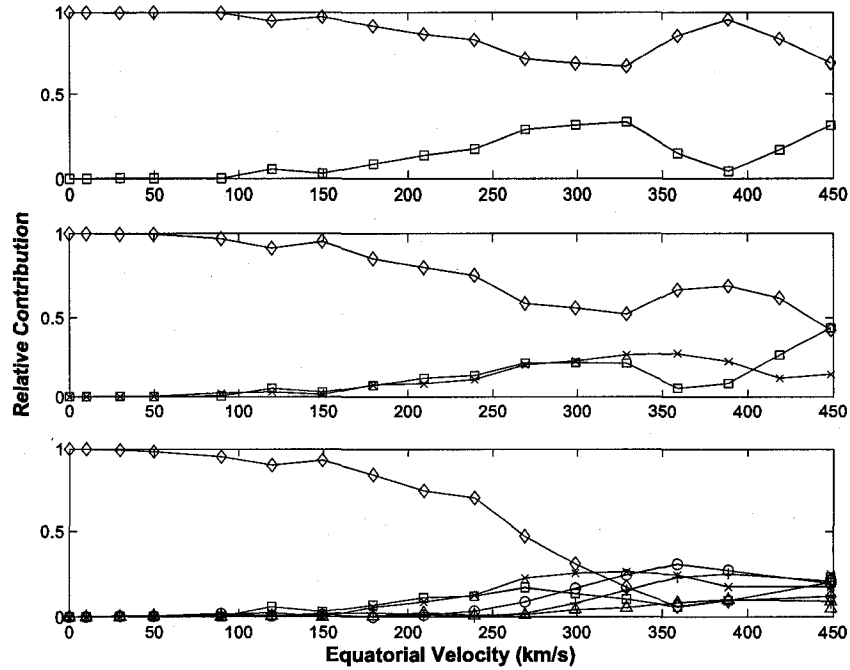
Figure 2.5: The relative contribution to the F mode of each spherical harmonic for 2 (top) 3 (middle) and 6 (bottom) spherical harmonics. In the top plot, after v $\sim$ 150 km s^{-1}, the contribution from $l_0 = 0$ drops below $\sim$ 90% and we say that you need more spherical harmonics to be able to model the mode. Symbols are defined as follows: $\diamond$ - $l = 0$, $\square$ - $l = 2$, x - $l = 4$, $\circ$ - $l = 6$, + - $l = 8$, $\triangle$ - $l = 10$.

contribution of each Y_l^m, shown for the radial fundamental mode in Fig. 2.5. At 90 km s^{-1}, with all three sets of basis functions, the $l = 0$ component contributes nearly 100%, while at 270 km s^{-1}, the contribution of the same component drops below 50% when 6 spherical harmonics are considered.

From Fig. 2.5, we can see that with two and three spherical harmonics, all of the spherical harmonics contribute a relatively significant amount by the time the model is rotating at intermediate speeds. In contrast, with six spherical harmonics, the contribution from the highest order spherical harmonics ($l = 10$) remains small out to at least 300 km s^{-1}. Although the contribution starts to become significant at very high rotation rates (v $\gtrsim$ 350km s^{-1}), it still remains a factor of 2-3 lower than the main contributors. From this, we have taken the shape of the eigenfunction with six spherical harmonics as being the most correct and have used it as a basis of comparison.

Based on the results shown in Fig. 2.4, we know that one spherical harmonic ceases to be sufficient somewhere between 90 and 270 km s^{-1}. From Fig. 2.5, we can see that the relative contribution of
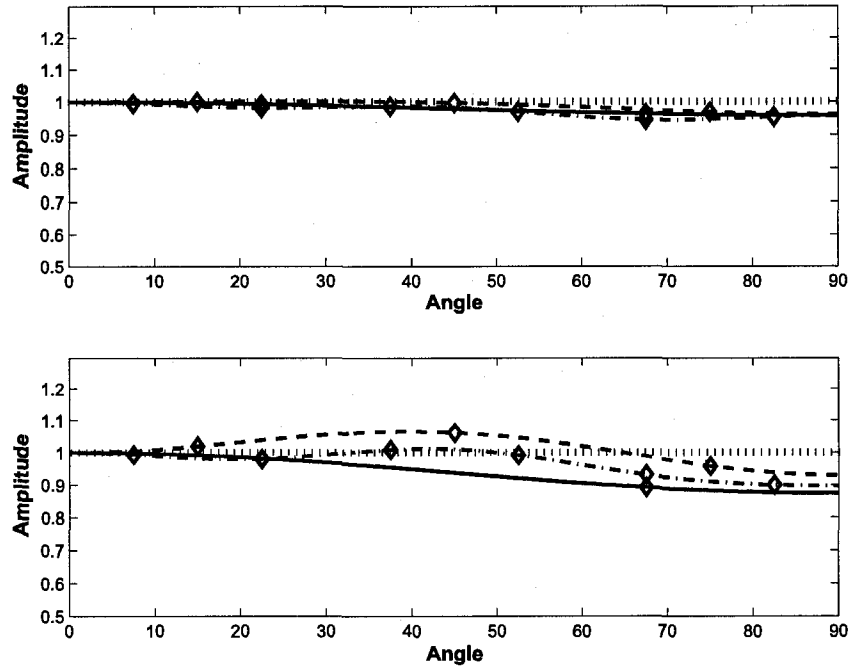
Figure 2.6: As for Fig. 2.4, but for the velocities on either side of the cut off surface equatorial velocity. At the lower velocity (150 km s^{-1}, top), the shape can be calculated reasonably well using one Y_l^m, but at the higher velocity (180 km s^{-1}, bottom), 2 or more are needed to accurately reproduce the horizontal variation in the eigenfunction. Symbols are the same as in Fig. 2.4.

the Y_0^m drops below 90% at a surface equatorial velocity between 150 and 180 km s^{-1}. The angular variation of the eigenfunctions for these two velocities are shown in Fig. 2.6. It is at this point that we would say multiple spherical harmonics are required to accurately reproduce the shape of the mode (cf. Fig. 2.6).

We have developed a quantitative measure of how the shapes of the eigenfunction differ from that calculated using six spherical harmonics. This estimate is calculated by taking the absolute value of the difference between the 6 basis function eigenfunction (standard) and one of the other eigenfunctions (comparison) at 9 points. These points are equally spaced across the surface of the model, with $\theta = 10i$. The point at $\theta = 0$ is excluded, as all the eigenfunctions are normalized to one at this point. These differences are then squared and summed. The square root of the sum is
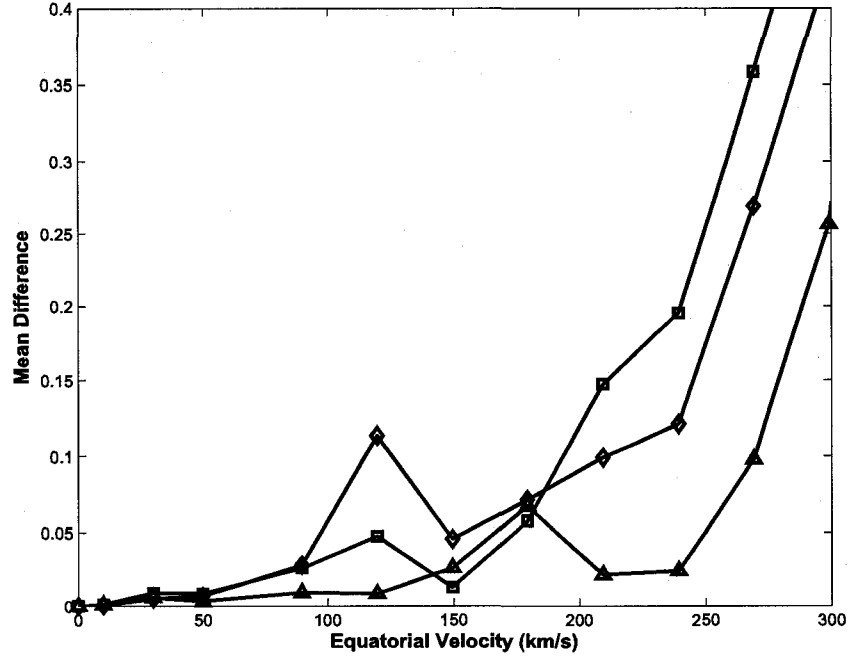
Figure 2.7: The mean difference between the shape of the radial fundamental eigenfunction with 6 spherical harmonics and a pure P_0 mode ($\diamond$), 2 spherical harmonics ($\square$) and 3 spherical harmonics ($\triangle$). Although there is some variation, all three curves show a sharp rise beyond 200 km s^{-1}. See text for the definition of the mean difference.

normalized by the number of points to give a measure of how different the two curves are:

$$\text{mean difference} = \frac{1}{n}\sqrt{\sum_{i=1}^{n}(a_i - b_i)^2}. \tag{2.8}$$

This difference as a function of surface equatorial velocity is shown in Fig. 2.7. The differences between the eigenfunctions calculated with 1, 2 and 3 spherical harmonics relative to 6 spherical harmonics rises sharply starting at a surface equatorial velocity of 180 km s^{-1}. Based on this rise and the eigenfunctions shown in Fig. 2.6, we estimate that when the mean difference rises above 0.06, more spherical harmonics are needed to accurately reproduce the shape of the mode.

For the other modes, the results are qualitatively similar, although the extent of the differences varies. The results for all four l_0 values considered in this paper are summarized in Table 2.2. Overall, one spherical harmonic remains a good approximation out to at least 90 km s^{-1} (0.23 Ω_c).

Table 2.2: Summary of velocities at which 1 Y_l^m fails to accurately reproduce the mode.

l_0	n	Frequency[a]	$\mathcal{D}\nu$[b]	Eigenfunction[c]
0	0	>360	-	165
0	1	240	160	60
0	2	180	24	25
1	0	210	-	110
1	1	210	140	105
1	2	180	30	85
2	0	-	-	75
2	1	-	-	60
2	2	-	-	45
3	0	-	-	70
3	1	-	-	85
3	2	-	-	-

[a]Limiting surface equatorial velocity based on frequency differences larger than 1%
[b]Limiting surface equatorial velocity based on difference in the large separation greater than 1μHz
[c]Limiting surface equatorial velocity based on eigenfunctions with mean differences larger than 0.06

For some modes, such as the radial fundamental, this approximation remains valid to much higher rotation rates (270 km s^{-1}, 0.64 Ω_c). As both the angular and radial order of the mode increase, the limiting surface equatorial velocity decreases. In most cases, we find that the differences among calculations with different numbers of spherical harmonics grow quickly as a function of surface equatorial velocity once the differences become sizeable. We can conclude that our results are not particularly sensitive to the exact value of the cutoff criterion we have chosen, as long as it is not significantly lower than what we have used. We also find that comparing frequencies or frequency differences produce approximately the same results. Based on our results for a 10 $M_\odot$ model, a single spherical harmonic is never a good approximation for rotation rates above 0.64 Ω_c, appears to always be a good approximation for rotation rates below 0.23 Ω_c, and must be used with caution for rotation rates between these two values. Although there may be some mass effects, we do not expect these results to change significantly for masses close to 10 $M_\odot$.

2.5 Comparison with Perturbation theory

Second order perturbation theory is routinely used to compute linear pulsation modes for rotating stars in which the centrifugal forces are expected to affect the pulsation frequencies. It has been

difficult to comment on when second order perturbation theory can be expected to fail because there have been few calculations of eigenfrequencies using other methods. Our approach will allow placing some limits on the range of applicability of second order perturbation theory, but again these limits will be a product of the accuracy obtainable or required.

Second order perturbation theory shows that, for axisymmetric modes as we consider here, the change in eigenfrequency is a linear function of the square of the rotation rate (e.g., Saio 1981). We shall compare our results with this linear relation in two separate ways, both of which determine the failure of perturbation theory by a deviation from this linear relation. Of course, the result will depend on the quantitative value as to when the deviation becomes significant, a point we will discuss at the end of this section. We shall use the results we believe most accurately reflect the true values of the pulsation frequencies, the results with six angular zones in the 2D pulsation grid for our comparison of eigenfrequencies.

The first method starts with the first four models in the rotation sequence (surface equatorial rotation velocities from 0 to 90 km s^{-1}. We calculate the best fit to the linear relationship as given by perturbation theory, and the standard deviation. We repeat this exercise, each time adding one more model to the analysis, until all rotation velocities are included. As long as the linear relation is satisfied, we expect the standard deviation to be approximately constant as we add results for more rapidly rotating models. At some point, as the rotation becomes more rapid, the standard deviation will become larger and at some threshold value will be declared no longer to be an adequate representation of a straight line. Thus second order perturbation theory would no longer be considered reliable. We plot this standard deviation as a function of the rotation rate of the most rapidly rotating member of each sample in Fig. 2.8. We somewhat arbitrarily set our threshold at 4 x 10^{-6} as being a value above the flat region for all modes. The values for the limits of applicability of perturbation theory computed by this method are listed in the column entitled 'Linear Fit' of Table 2.3. We have also examined the slope of each linear fit, and as expected, find that the slope changes gradually where the linear fit is good, and more rapidly as more points are added.

One difficulty with the above approach is that the coefficients of the linear fit change as more rapidly rotating models are added. A more constraining determination of the threshold of perturbation theory might be obtained by using the first few members of the sequence to determine the coefficient of the linear fit. The assumption is that the slope that perturbation theory would predict is correctly computed using the first few slowly rotating members of the sequence. We use the first five members in our rotation sequence to calculate this coefficient. We then use this coefficient to determine perturbation theory frequencies at each of our surface equatorial velocities. As before, we take the differences between the two methods as significant when they are larger than 1%. The results for this method are listed in the column entitled 'Coefficient Fit' of Table 2.3. We compare our pulsation frequencies with those predicted assuming the coefficient computed for the first four members of the sequence is valid at all rotational velocities in Fig. 2.9.

We find the trends for both methods of evaluating the threshold are similar for the two methods, but that the thresholds computed for the coefficient fit are more constrained. This is to be expected because forcing a linear fit to have a certain slope is more confining that merely forcing a fit to be linear. It is interesting that the threshold for perturbation theory occurs at generally higher rotation speeds than the threshold for the validity of a single spherical harmonic. The extrapolation of the linear fit to higher rotation velocities is flatter than our calculation with six angular zones and much flatter than our calculation with only one angular zone.

Our results indicate that perturbation theory is satisfactory to appreciably larger rotation velocities than the results of Reese, Lignières & Rieutord (2006), who found that third order perturbation theory failed for rotation rates above about $0.2\ \Omega_c$. Much of this difference arises from the much tighter constraint they placed on what difference in eigenvalues is significant. They are able to do this because they perform their comparisons using polytropes, which can be numerically integrated very accurately, whereas we use finite difference techniques to generate our more realistic stellar models. A subsidiary consideration is that they can control both the total mass and radius, and thus can arbitrarily scale from one model to the next, whereas our models include the conservation of energy, which removes the radius as an arbitrary parameter. Also, the surface locations at each

Table 2.3: Summary of velocities at which perturbation theory fails to accurately reproduce the mode.

l_0	n	Linear fit	Coefficient fit	1 Y_l^m(max/min)[a]
0	0	-	360	>360/160
0	1	-	240	240/60
0	2	300	270	180/25
1	0	-	-	210/110
1	1	>360	330	210/105
1	2	360	210	180/30
2	0	330	240	75
2	1	330	180	60
2	2	270	120	45
3	0	330	210	70
3	1	330	210	85
3	2	360	330	-

[a]maximum and minimum rotation speeds at which 1 Y_l^m is valid, where more than one criterion exists.

angle of our rotating models are quantized; the surface is regarded to include the full radial zone instead of fractions of zones. Our errors are in line with variations in eigenvalues computed for radial modes at a similar stage of development (e.g., Castor 1971). We believe these errors are reasonable at the present time because the deduced properties of the stars observed will be inaccurate both from the conversion from observed parameters to theoretical parameters and from the uncertainties in the effects of inclination on the relation between the observed and intrinsic properties. The model and parameter inaccuracies will be far greater than the error in the observed frequencies. Physical uncertainties, particularly in the internal angular momentum distribution, are expected to be greater than or equal to the uncertainties in an individual model, particularly for the more rapidly rotating stars in which we are interested ($v > 200$km s^{-1}). We believe that being able to compute the evolution of the rotation law as the star ages may, at this stage, play a more important role than increasing the accuracy of the calculations. Of course, we recognize that improvements in accuracy on all fronts are valuable.

2.6 Conclusions

In this paper, we have attempted to test the validity of two independent assumptions commonly made in calculating stellar oscillation frequencies. These are firstly, that the non-radial modes can
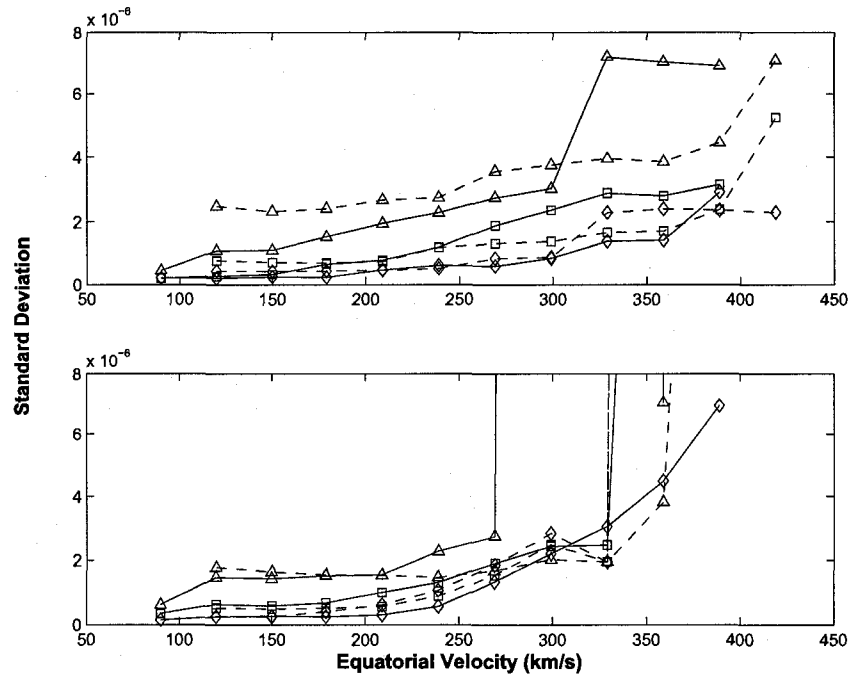
Figure 2.8: Standard deviation from a straight line as more points are included for the $l_0 = 0$ and 1 modes (top) and $l_0 = 2$ and 3 modes (bottom). We take the cut off standard deviation to be 4×10^{-6}. Symbols are as follows: $\diamond$ - fundamental, $\square$ - first harmonic, $\triangle$ - second harmonic. Solid lines represent the even modes (0, 2) and dashed lines represent the odd modes (1, 3).
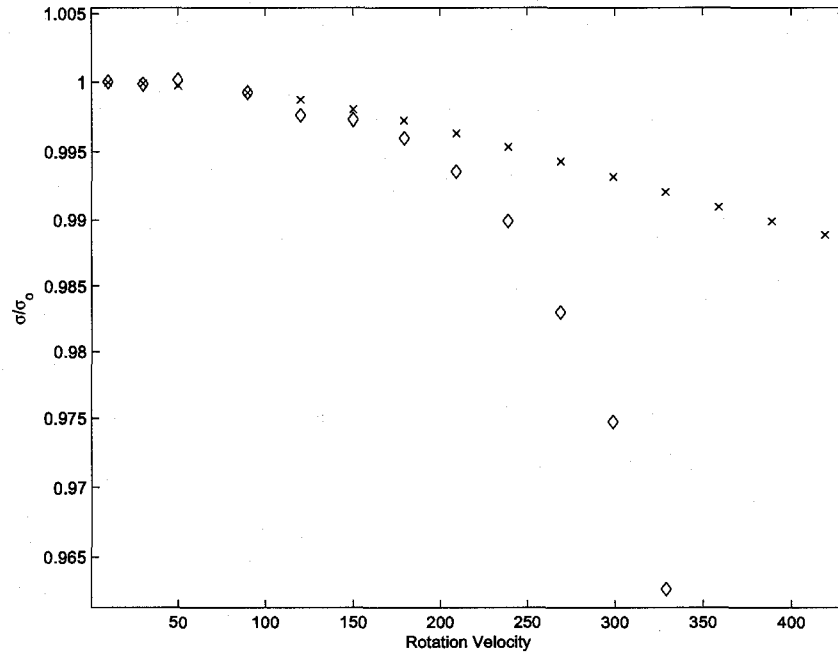
Figure 2.9: Normalized frequencies as calculated with NRO (◇) and using an estimate of the pertur-
bation theory results (x) for the $l_0 = 2$ f mode.

be modelled using a single Y_l^m, and secondly, that the modes can be calculated using second order

perturbation theory out to some limiting (highly uncertain) rotation rate.

We find that when a single spherical harmonic becomes inaccurate is mode dependent, with it

failing at lower rotation velocities for higher order modes. The answer is also different depending on

what property one examines. A single spherical harmonic is sufficient to reproduce frequencies to

within 1% for rotation velocities up to at least 180 km s^{-1}($0.44\Omega_c$), and for some low order modes,

may even be valid up to 390km s^{-1}($0.85\Omega_c$). In contrast, the angular shapes of the eigenfunctions are

extremely sensitive to rotation, and the assumption fails at a maximum surface equatorial velocity of

165 km s^{-1}. In most cases, the assumption fails at much lower rotation velocities, typically around

50-75km s^{-1}. Period differences (large separations) are expected to be of most interest, and these

are also found to be sensitive to the order of the mode. A single spherical harmonic can accurately

predict the difference between the fundamental and first harmonic of the $l_0 = 0$ and 1 mode up to

velocities of around 150km s^{-1}($0.37\ \Omega_c$). The higher order modes are very sensitive to rotation, and

the assumption fails at velocities of around 25-30 km s^{-1}(0.08 Ω_c). One interesting consequence of the limitations of a single spherical harmonic is the impact it may have on mode identification, which is most often based on comparing the variation in pulsation amplitude with color with models computed assuming a single spherical harmonic (e.g., Heynderickx, Waelkens & Smeyers 1994).

We have compared our eigenfrequencies with the relation between eigenfrequency and rotation rate predicted by second order perturbation theory. The relationship is followed reasonably well for models rotating up to surface rotational velocities of about 400 km s^{-1}for very low order modes. The relation fails at lower rotational velocities (approximately 200 km s^{-1}or $\Omega/\Omega_c = 0.58$) for modes with two or three radial nodes. These values are dependent on the difference between the two sets of frequencies tolerated. In these calculations, the limits are determined by the properties of the rotating stellar models rather than the calculations of the eigenfunctions.

Chapter 3

Effects of Uniform and Differential Rotation on Stellar Pulsations[1]

We have investigated the effects of uniform rotation and a specific model for differential rotation on

the pulsation frequencies of 10 $M_\odot$ stellar models. Uniform rotation decreases the frequencies for all

modes. Differential rotation does not appear to have a significant effect on the frequencies, except

for the most extreme differentially rotating models. In all cases, the large and small separations

show the effects of rotation at lower velocities than do the individual frequencies. Unfortunately, to

a certain extent, differential rotation mimics the effects of more rapid rotation, and only the presence

of some specific observed frequencies with well identified modes will be able to uniquely constrain

the internal rotation of pulsating stars.

3.1 Introduction

Observationally detected stellar pulsation frequencies can be used to place constraints on stellar

models, giving us an improved understanding of their interior structure and evolution. The most

successful application has been the Sun, where the large number of observed modes have placed strict

constraints on parameters such as the helium abundance (Y) (Basu & Antia, 2004; Antia & Basu,

2006), the depth of the convection zone (Christensen-Dalsgaard *et al.*, 1989, 1991), and the interior

angular momentum distribution (Eff-Darwich *et al.*, 2002; Couvidat *et al.*, 2003). Observations

of pulsation frequencies of other stars continue to improve, particularly through dedicated satellites

such as WIRE (Hacking *et al.*, 1999), MOST (Walker *et al.*, 2003), CoRoT (Baglin & *et al.*, 2001) and

Kepler (Basri, Borucki & Koch, 2005) as well as ground-based networks such as STEPHI (Belmonte

et al., 1993) and WET (Nather *et al.*, 1990). These improved observations, giving us long term

---

[1]The contents of this chapter have been submitted to the Astrophysical Journal.

coverage and improved accuracy, are the first steps in enabling other stars to be constrained in a similar manner to the Sun. Asteroseismology then, has the potential to answer a number of questions about the interior structure of stars throughout the HR diagram.

One aspect of stellar structure which could be explored using asteroseismology is the internal rotation rate. The Sun is known to rotate differentially in the convection zone, with the angular velocity approximately linearly increasing with radius, with a constant of proportionality depending on the latitude (Schou *et al.*, 1998; Thompson *et al.*, 2003). It is also theoretically possible for stars to rotate with angular velocity increasing or decreasing with distance from the rotation axis, and there is some evidence that the latter may be true in massive main sequence stars, at least at the surface (Stoeckley, 1968). A third possibility is uniform rotation. It has been argued that uniform rotation is unrealistic based on observations of the Praesepe and Hyades clusters (Smith, 1971). Of course, other, less well structured rotation laws are possible. However, there is little evidence in support of a specific rotation law, and the large uncertainties prevent any of the possibilities from being ruled out.

Recently, interferometric observations of Achernar (Domiciano de Souza *et al.*, 2003) found that this star is far more oblate than is possible for a uniformly rotating star. This is true because uniformly rotating stars reach critical rotation before they have sufficient angular momentum to produce such an oblate object. However, Jackson *et al.* (2005) noted that models in which the rotation rate increases inward from the surface can produce the oblateness observed for Achernar and still match the observed $v \sin i$. While further study has proposed that the oblateness may be due to a circumstellar envelope (Carcofi *et al.*, 2008), the original conclusion does raise the interesting question as to whether stars with rotation laws required to produce such an oblate shape could be identified by possible pulsation modes (assuming they exist). We investigate this possibility in this paper.

Differential rotation with rotation rate increasing inwards, as is considered in this paper, will have an impact on the deep interior structure of the star, provided the differential rotation is large enough. Rapid rotation in the outer layers of a star has little to no effect on the gravitational potential and

core structure, as the envelope contains a relatively small fraction of the stellar mass. In fact, many early attempts to model rotating stars assumed that the mass in the envelope was negligible and that the gravitational potential in this region could be modelled using a Roche potential (Sackmann & Anand, 1970). However, it was recognized early on that this assumption was not always valid. Efforts to model a wider variety of rotating stars were made through the implementation of the self-consistent field (SCF) method (Ostriker & Mark, 1968), or through direct, 2D finite difference solutions to Poisson's equation (Clement, 1974, 1978, 1979). These methods allowed stars to be modelled with differential rotation, at least under certain circumstances. Concentrating angular momentum in the center, unlike uniform rotation, can produce enough distortion to affect the core, and consequently the evolution of the star. Only in this case can we produce a model with interior properties significantly different from the uniformly rotating model (Sackmann & Anand, 1970). Even restricting ourselves to this type of differential rotation does not narrow the possibilities significantly. The rotation could be shellular, as proposed by Zahn (1992), or cylindrical (conservative rotation laws). In this paper, we have focused on conservative rotation laws, either with uniform rotation or with rotation rate increasing towards the center of the star. Further discussion of our models can be found in §3.2. In §3.3 we consider the eigenfrequencies of rotating models as well as the large and small separations in §3.4 and §3.5 respectively. Our conclusions are summarized in §3.6.

3.2 Numerical Models

The stellar models are computed using the 2D stellar structure code ROTORC (Deupree, 1990, 1995). The code uses the OPAL opacities (Iglesias & Rogers, 1996) and equation of state (Rogers, Swenson & Iglesias, 1996). Here we consider only 10 $M_\odot$ ZAMS models with X=0.7, Z=0.02. These models solve the conservation equations of mass, momentum, energy, and hydrogen abundance along with Poissons equation for the gravitational potential on a two dimensional finite difference grid with the fractional surface equatorial radius and the colatitude as the independent variables. The surface equatorial radius is determined by requiring that the integral of the density over the volume of the

model equals the stellar mass. The ZAMS models are taken to be time independent and static, except for the imposed rotation law, so that the mass, azimuthal momentum, and hydrogen composition conservation equations drop out.

The only change required in the stellar evolution code for nonuniform cylindrical rotation laws is the addition of an extra term in the total potential (e.g., Tassoul 2000):

$$\begin{aligned} \Psi &= \Phi - \int_0^{\varpi} \Omega^2(\varpi')\varpi'd\varpi' \\ &= \Phi - \frac{\Omega^2\varpi^2}{2} + \int_0^{\varpi} \varpi'^2\Omega(\varpi')\frac{d\Omega(\varpi')}{d\varpi'}d\varpi' \end{aligned}$$

(3.1)

where Ω is the rotation velocity (in radians per second) and ϖ is the distance from the rotation axis ($x sin\theta$, where x is the fractional surface equatorial radius and θ is the colatitude). The extra term is the last term on the right hand side of the equation. Performing the integral is straightforward for an analytically imposed rotation rate distribution in the ZAMS models. The total potential is used only to determine the surface location at each latitude by taking the surface to be an equipotential. Although defining a total potential requires a conservative rotation law, this is the only way in which a conservative rotation law is utilized in the stellar structure code.

We have constructed uniformly rotating ZAMS models with rotation velocities between 0 and 360 km s^{-1}, with an approximate spacing of 30 km s^{-1}. We have also computed a number of differentially rotating models at two values of the surface equatorial rotation velocity, 120 and 240 km s^{-1}. The differential rotation law is as given by Jackson *et al.* (2005):

$$\Omega(\varpi) = \frac{\Omega_o}{1 + (a\varpi)^\beta}$$

(3.2)

where β is a parameter ranging from 0 (uniform rotation) to 2, the maximum allowed for stability. The parameters a and Ω_o are used to impose the desired surface equatorial velocity and shape of the rotation law at small distances from the rotation axis. We have arbitrarily chosen $a = 2$. Figure 3.1 shows the rotation rate as a function of distance perpendicular to the rotation axis for a surface equatorial rotation velocity of 120 km s^{-1} and a surface equatorial radius for a uniformly rotating
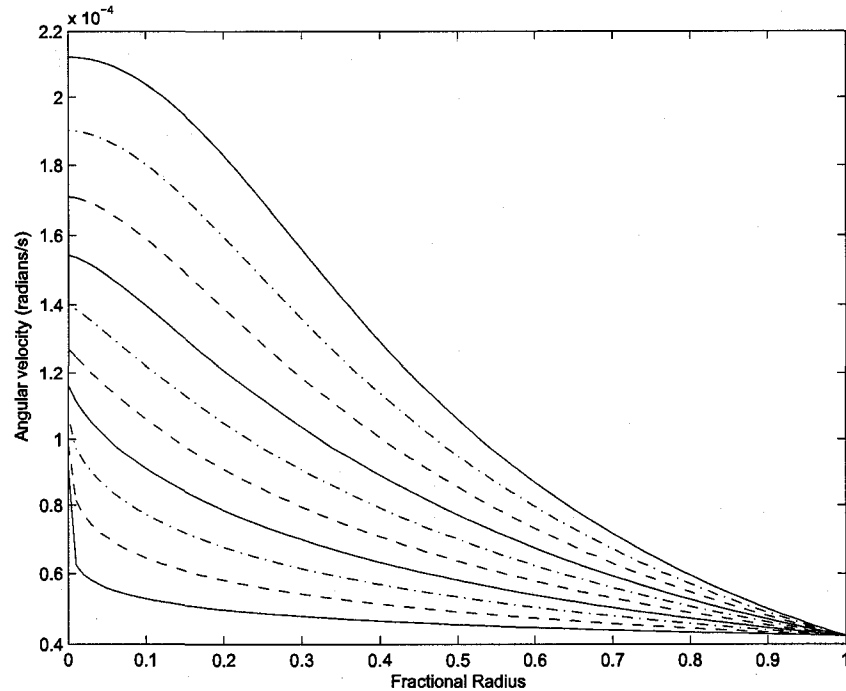
Figure 3.1: Rotation law used in differentially rotating models (Eqn. 3.2). Curves show from bottom to top the rotation law for $\beta = $ 0.2, 0.4, 0.6, 0.8, 1.0, 1.2, 1.4, 1.6, 1.8 and 2.0. for a model with a surface equatorial velocity of 120 km s^{-1}.

model at that speed. Increasing β increases the rotation rate close to the the rotation axis, including in the core of the star. Increasing angular momentum increases structural changes, and thus the structural changes increase with increasing β. It is expected that increasing rotation rate through increasing β may in some ways mimic more rapid uniform rotation.

One major result produced by significant rotation is an appreciable distortion of the surface of the model. We present the surface shape for a set of uniformly rotating models with surface equatorial velocities ranging from 0 to 360 km s^{-1} in Figure 3.2. For each model the equatorial radius is taken to be unity. The ratio between the polar and equatorial radius decreases with increasing rotation, as the polar radius decreases slightly while the equatorial radius increases considerably. Differential rotation in which the rotation rate increases with decreasing distance from the rotation axis amplifies this effect. We present the surface shape for the differentially rotating models in Figure 3.3. The solid curves are for a surface equatorial velocity of 120 km s^{-1}, while the dashed curves denote
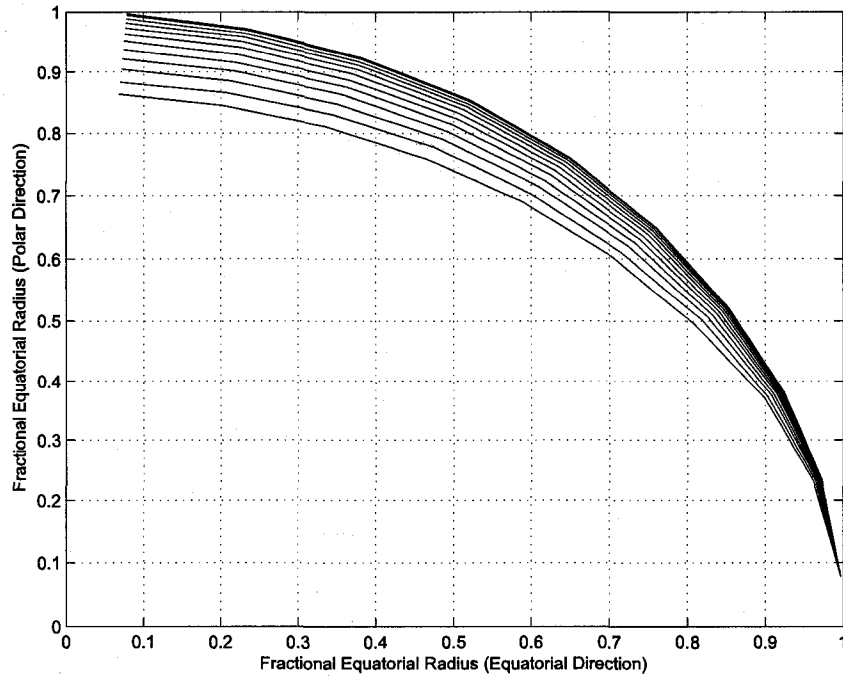
Figure 3.2: Surface shape for uniformly rotating models. The polar radius decreases relative to the equatorial radius as rotation increases from 0 km s^{-1} to 360 km s^{-1}.

a surface equatorial velocity of 240 km s^{-1}. As the parameter β in Equation 3.2 increases, the fractional polar radius decreases. The change in fractional radius with β is greatest at the pole and decreases towards the equator. Note that the fractional polar radius for a model rotating with a surface equatorial velocity of 120 km s^{-1} and a value of β of 1.8 has nearly the same fractional polar radius as a model uniformly rotating at 240 km s^{-1}.

We have increased the radial resolution of the static models by more than a factor of two over that used by Lovekin and Deupree (2008). The intent is to reduce the scatter and uncertainty in the pulsation mode calculations, particularly for the large and small separations. By and large this has been successful.

The determination of the pulsational properties of these models is made using the linear adiabatic pulsation code developed by Clement (1998). We are restricted to input models with conservative rotation laws so that we can write the effective gravity as the derivative of the total potential. The input models are spheroids, which allows us to assume a $e^{i[\omega t + m\phi]}$ time and azimuthal depen-
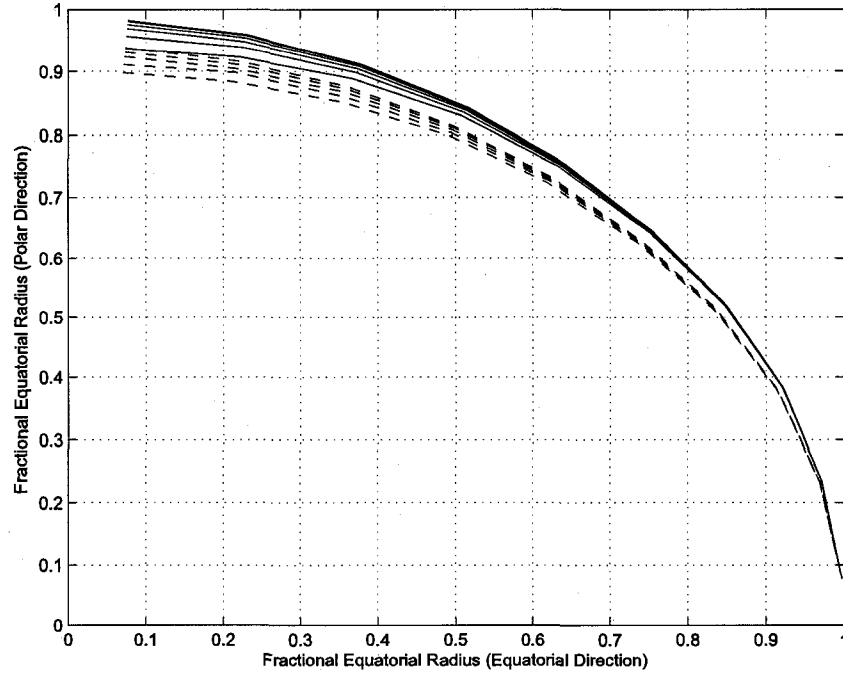
Figure 3.3: Surface shape for differentially rotating models at 120 km s^{-1} (solid) and 240 km s^{-1} (dashed). As the rotation rate close to the rotation axis increases (increasing β), the polar radius decreases relative to the uniformly rotating case.

dence. The linearized equations are thus the three components of the momentum equation, the linearized mass conservation equation, the adiabatic relation between the density and pressure, and the linearized Poissons equation. The dependent variables are the three components of the linear displacements $(\vec{\xi})$, the linear (Eulerian) perturbations of the density $(\delta\rho)$ and pressure (δP), and the linear perturbation of the gravitational potential $(\delta\phi)$:

$$\sigma^2\rho\vec{\xi} + 2i\sigma\rho(\vec{\xi}\times\vec{\Omega}) + \vec{g}\delta\rho - \vec{\nabla}\delta P + \rho\vec{\nabla}\delta\phi = 0 \tag{3.3}$$

$$\delta\rho = -\vec{\nabla}\cdot\rho\vec{\xi} \tag{3.4}$$

$$\delta P = -\Gamma_1 P\vec{\nabla}\cdot\vec{\xi} - \vec{\xi}\cdot\vec{\nabla}P \tag{3.5}$$

$$\nabla^2\delta\phi = -4\pi G\delta\rho. \tag{3.6}$$

In the above equations, $\vec{g}$ is the effective gravity, given by the gradient of the total potential, Ψ and

σ is the pulsation frequency. With the definitions

$$\delta p = \delta P / \rho - \delta \phi \tag{3.7}$$

and

$$A = c^2 \frac{dln\rho}{d\psi} - 1 \tag{3.8}$$

where c is the adiabatic sound speed given by $c^2 = \Gamma_1 P / \rho$, we can solve Equation 3.5 for $\vec{\nabla} \cdot \vec{\xi}$ to

obtain

$$
\begin{aligned}
\vec{\nabla} \cdot \vec{\xi} &= -\frac{1}{c^2}(\delta p + \delta \phi + \vec{\xi} \cdot \vec{g}) \\
&= \frac{1}{r^2} \frac{\partial}{\partial r}(r^2 \xi_r) + \frac{1}{r sin\theta} \frac{\partial}{\partial \theta}(\xi_\theta sin\theta) + \frac{im}{r sin\theta} \xi_\phi.
\end{aligned}
\tag{3.9}
$$

With some manipulation, the three components of the linearized momentum equation are:

$$\sigma^2 \xi_r + 2i\sigma\Omega\xi_\phi sin\theta - \frac{\partial \delta p}{\partial r} = \frac{Ag_r}{c^2}(\delta p + \delta \phi + \vec{\xi} \cdot \vec{g}) \tag{3.10}$$

$$\sigma^2 \xi_\theta + 2i\sigma\Omega\xi_\phi cos\theta - \frac{1}{r}\frac{\partial \delta p}{\partial \theta} = \frac{Ag_r}{c^2}(\delta p + \delta \phi + \vec{\xi} \cdot \vec{g}) \tag{3.11}$$

$$\sigma^2 \xi_\phi = 2i\sigma\Omega(\xi_r sin\theta + \xi_\theta cos\theta) + \frac{im}{r sin\theta}\delta p. \tag{3.12}$$

Equation 3.4 can be shown to be

$$\delta\rho = -\vec{\nabla} \cdot \rho\vec{\xi} = \frac{\rho}{c^2}(\delta p + \delta\phi - A\vec{\xi} \cdot \vec{g}) \tag{3.13}$$

so that Poisson's equation becomes

$$\nabla^2 \delta\phi = 4\pi G \frac{\rho}{c^2}(\delta p + \delta\phi - A\vec{\xi} \cdot \vec{g}) \tag{3.14}$$

We now have the necessary equations. Equation 3.10 gives us an equation in which the only

radial derivative is that of δp, and we can use Equation 3.12 to eliminate the azimuthal displacement (and the imaginary parts). Equation 3.9 provides an expression with the radial derivative of the radial displacement. Poisson's equation can be rewritten as two equations, one of which defines a new variable as the radial gradient of the gravitational potential perturbation, and the second is Poissons equation written in terms of this new variable and the gravitational potential perturbation itself. Equation 3.11, with Equation 3.12 substituted to remove the azimuthal displacement, can be solved as is because it does not involve any radial derivatives. One does need the radial derivative of ξ_θ, but this can be obtained by taking the radial derivative of Equation 3.11. All the equations are derived assuming a conservative rotation law, but there is nothing in the framework to limit the application to uniform rotation.

Using Equations 3.10, 3.11, 3.12 and 3.14, we can calculate the pulsation properties of the stellar models on a 2D finite difference grid. This is done through a change of variables, factoring out the behavior of ξ_r, ξ_θ, δp and $\delta\phi$ near the boundaries to eliminate singularities. The coefficients of these equations can be put in a band-diagonal matrix and solved. NRO can include up to nine angular zones in the eigenfunction solution. This gives the solution at N angles, where N is the number of angular zones, which can subsequently be decomposed into the contributions of individual spherical harmonics through the use of Fourier transforms. Throughout this paper, we have used N = 6. Based on the calculations of Lovekin & Deupree (2008a), six spherical harmonics is sufficient to accurately calculate the eigenfrequencies for the most rapidly rotating models discussed here. Indeed, we have performed a few test calculations with N = 8 and have found that the effect on the frequencies is small, typically a few hundredths of a percent.

As discussed in Lovekin & Deupree (2008a), NRO, combined with stellar structure models from ROTORC, allows us to calculate the pulsation frequencies for rotating stars without making any *a priori* assumptions about the structure, except that the rotation law is conservative for NRO. For further discussion of the method of solution used by NRO, refer to Clement (1998) or Lovekin & Deupree (2008a).

With spherical stellar models, the radial and angular components of the perturbations separate,

and the angular part can be expressed as a spherical harmonic with specific values of the quantum numbers, l and m.

For rotating stars, the eigenfunction solution is not a single spherical harmonic, and l is not a valid quantum number. Indeed, NRO uses l only to specify the parity of the mode being calculated, and includes the first k even or odd spherical harmonics, where k is the number of angles included. We identify modes using a quantum number l_o, which is the l of the mode in the non-rotating model to which a given mode can be traced. For spheroids, m remains a valid quantum number. As in Lovekin & Deupree (2008a), we restrict ourselves to axisymmetric modes ($m = 0$) and modes with small radial quantum number (n).

3.3 Relative frequencies

In this paper we consider low order axisymmetric modes for $l_o = 0$, 2 and 3 ($n = 0$-3) and $l_o = 1$ ($n = 1$-4). These modes are expected to have the highest amplitudes and the smallest cancellation effects across the visible surface of the star, and are hence expected to be the most easily visible. Our structural models cover velocities from 0 to 360 km s^{-1} and for two velocities, 120 and 240 km s^{-1}, we have calculated differentially rotating models with β varying from 0 to 2.0. Tracing the individual modes becomes very difficult above rotation velocities of 360 km s^{-1} and for some higher values of β, and this represents a practical limit to our study. Although the frequencies can be calculated at these velocities, the resulting eigenfunctions are a mix of six spherical harmonics, and no single mode dominates. As it is very difficult to reliably assign a value of l_o to these modes, we exclude them from our analysis. It is probably feasible to trace the modes accurately, but this could require an extremely fine rotational velocity grid (1-5 km s^{-1}). We decided not to pursue this for this exploratory work. For differentially rotating models, the limits are $\beta = 1.8$ for the 120 km s^{-1} model and $\beta = 1.0$ for the 240 km s^{-1} model. Based on the curves shown in Figure 3.1, it appears that the limit is related to the angular velocity near the rotation axis. The curve representing $\beta = 1.0$ has approximately half the value at the center of the $\beta = 2.0$ curve. Therefore, if we double the velocities everywhere, the limiting β should move from 1.8 at 120 km s^{-1} to 1.0 at 240 km s^{-1},

which corresponds to approximately the same angular velocity near the rotation axis.

3.3.1 Uniform Rotation

The trends produced by tracing a given mode through increases in rotation velocity are illustrated in Figure 3.4 for the $l_o = 2$ mode, which shows the eigenfrequencies normalized by the non-rotating frequency for each mode. Overall, the trends we find for frequency agree with those calculated by previous work (Lignières, Rieutord & Reese, 2006). These authors find that the frequencies decrease as one increases the rotation rate, with higher frequency modes decreasing more than lower modes. As discussed in Lovekin & Deupree (2008a), our results at low to moderate rotation rates are also consistent with the frequency trends predicted by second order perturbation theory (see for example, Saio 1981).

We have increased the radial resolution of the outer 30% of the radius of the static models by more than a factor of two over that used by Lovekin & Deupree (2008a). This produces a radial zoning finer than that currently allowed by the pulsation code, so further increases in radial resolution in the 2D structure models will only be effective if the pulsation code is modified to allow more radial zones. The intent of the modified zoning is to reduce the scatter and uncertainty in the mode calculations evident in Lovekin & Deupree (2008a). Figure 3.4 shows that a reasonable estimate of our accuracy for the frequencies is a very few tenths of a percent, although there are still a few frequencies, most commonly but not exclusively for the higher radial orders and higher rotation rates, which do not fit within this limit. One might expect the radial resolution near the rotation axis and at mid latitudes to be less than for lower rotation rates because the fractional radius at these latitudes compared to the equator is lower. The accuracy of the small separation appears well within a μHz, while the large separation does show variations on the order of one μHz, particularly at higher rotation velocities and for higher radial order modes. This is compatible with the notion that the radial resolution near the surface could continue to benefit from refinement. However, these uncertainties do not disguise trends in the results, even in the large separation, with respect to rotation rate or the rotation law, and we consider these trends significant.
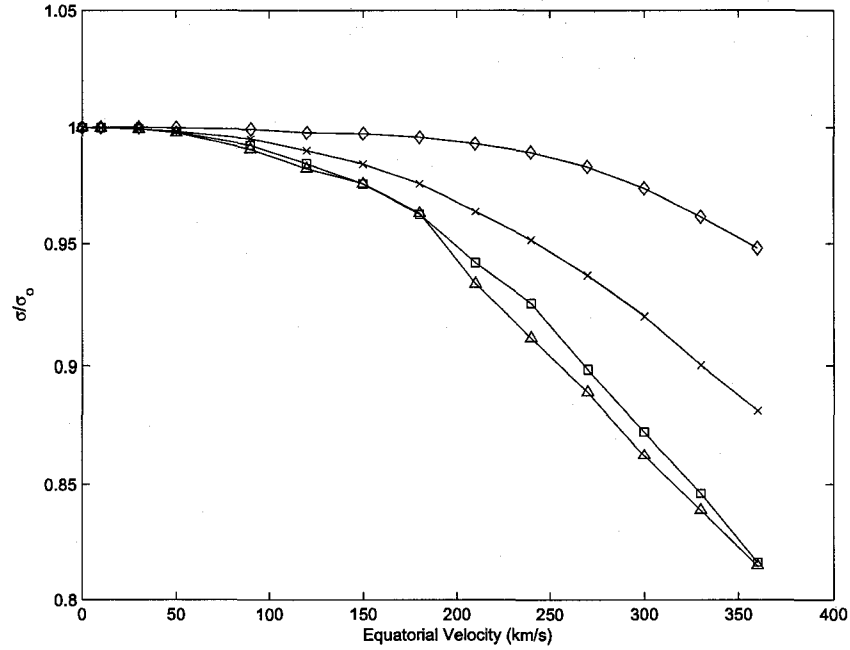
Figure 3.4: The first four harmonics of the $l_o = 2$ mode for a uniformly rotating 10 $M_\odot$ model as a function of rotation rate. The four curves represent the frequencies for the f (diamond), p_1 (X), p_2 (square) and p_3 (triangle) modes.

One interesting line of inquiry is whether there is some analog to the period - mean density relation which allows interpolation of eigenfrequencies as functions of models and rotation rates. Specifically, we have examined if there is a physically meaningful radius which can be used in the period - mean density relation

$$Q = P\sqrt{\frac{M}{R^3}} \qquad (3.15)$$

(where M and R are in solar units) that would allow Q to be approximately constant as a function of rotation rate. The comparatively small changes in the eigenfrequencies shown in Figure 3.4 suggest that the surface equatorial radius, with its fairly rapid increase as a function of rotation, will not keep Q approximately constant, and it does not. The same is true for an average radius, defined as either a straight average or the effective radius required to contain the total volume of the model. The polar radius would be more promising because it only slowly varies with rotation rate, but it actually decreases slightly as the rotation rate increases. This is the wrong direction to keep Q constant because the frequency decreases as well. Because the polar radius decreases slightly and
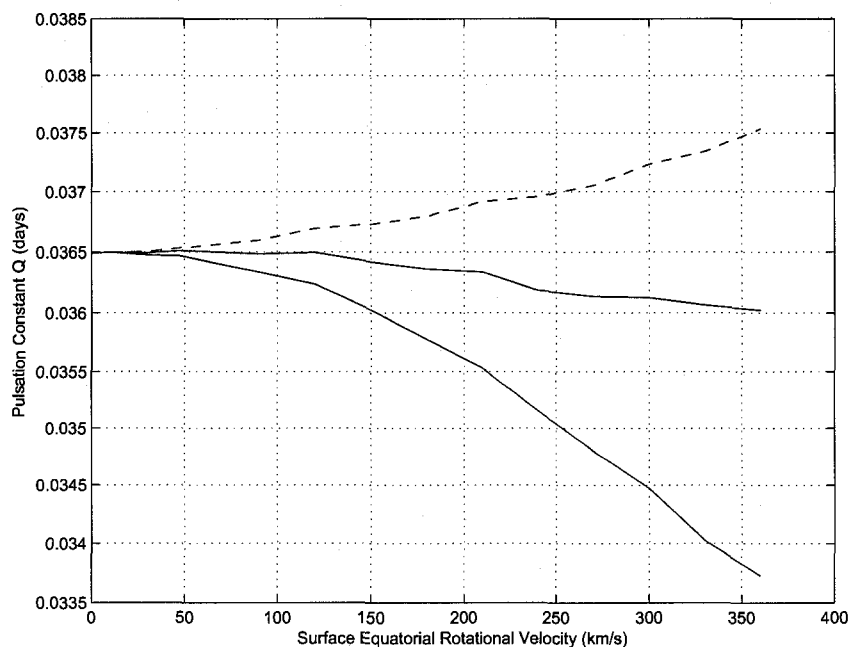
Figure 3.5: Plot of a quantity proportional to the pulsation constant as a function of surface equatorial rotation velocity for uniformly rotating models (solid curve). For comparison, we show a suitably scaled curve which is proportional to the inverse of the pulsation frequency (dashed curve).

the equatorial radius increases appreciably with increasing rotation, one might guess there would be some latitude at which the radius increases at a rate that nearly offsets the rate of period increase. This is true, and occurs at a colatitude of 40 degrees. It is not obvious that this has any physical significance because it is difficult to associate any specific meaning to the radius at this latitude. We present the pulsation constant for two definitions of an effective radius in Figure 3.5. One way is to use the radius of a sphere with the same volume as the model. The other uses the radius at a colatitude of 40°. For comparison we show a "pulsation constant" that would exist if the mean density did not change as a function of rotation rate. Interestingly, the variation in the pulsation constant is significantly larger than if the mean density is not changed.

The frequencies can also be changed by the mass or evolutionary state of the star, producing trends that could potentially be confused with rotational effects. We wish to determine how closely the frequencies of a rotating model can be mimicked by a non-rotating model. First we calculated the Q values for each model in the 10 and 12 $M_\odot$ non-rotating models. For each mode, we then

took the mean of the Q of the two models. We used this average Q for the radial fundamental mode and the frequency of the radial fundamental mode for the model rotating at 150 km s^{-1} to calculate a mean density. This corresponds to the mean density of a non-rotating model of unknown mass and radius pulsating in the radial fundamental mode with the same frequency as the 10 M$_\odot$ model rotating at 150 km s^{-1}. The mean density found this way and the average Q's for the other l_o's can be used to predict the other frequencies of this presumed non-rotating model. When these frequencies are compared to the calculated frequencies for the rotating model, the differences are significant. Using Q to calculate the frequencies in this way forces the radial fundamental mode to have the same frequency, so the differences between frequencies should be solely a result of rotation. The frequencies predicted for the $l_o = 0$ and 2 modes are larger by 1-5%, with the differences increasing for higher order modes. At the same time, the frequencies predicted for the $l_o = 1$ and 3 modes are smaller, by as much as 15 % for the $l_o = 1$ p_1 mode. As the radial order increases, the differences between the rotating model and the non-rotating calculation decreases for the $l_o = 1$ modes, but increases for the $l_o = 3$ modes. The size and direction of these trends implies that the pulsation spectrum of a rotating model is unlikely to be confused with the pulsation spectrum of a more massive non-rotating model. It also suggests that rotation must be included in the calculations if observations indicate it might be present even at this moderate amount.

We have also evolved a single non-rotating model, and compared the ZAMS model with one part way through the main sequence evolution (X$_c$ = 0.47). In this case, the frequencies decreased sufficiently, even for a model with a large remaining core hydrogen fraction, that confusion seems unlikely.

3.3.2 Differential Rotation

We have studied the change in the frequencies of 10M$_\odot$ ZAMS models differentially rotating at 120 km s^{-1} and 240 km s^{-1}. Overall, the frequencies increase for $l_o = 0$ and 1, and decrease for $l_o = 2$ and 3, a trend seen at both 120 km s^{-1} and 240 km s^{-1}. Our results for $l_o = 0$ are shown in Figure 3.6 for the fundamental, 1H, 2H and 3H modes for a model rotating at 120 km s^{-1}. In this case, the
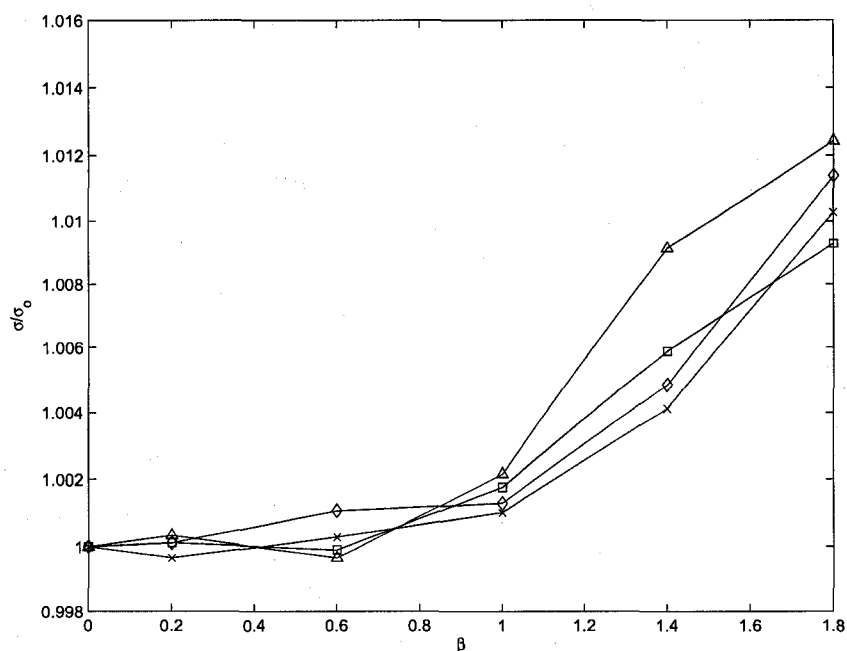
Figure 3.6: The fundamental and first three overtones of the $l_o = 0$ mode for a model rotating at 120 km s^{-1}as a function of the differential rotation parameter β (see Equation 3.2). The four curves represent the frequencies for the fundamental (diamond), 1H (x), 2H (square) and 3H (triangle) modes.

frequency changes are largest for the 3H modes, but are noticeable for all modes by $\beta \approx 1$. Similar trends are found for the other values of l_o considered here. Still, the differences remain relatively small, and it seems unlikely that even extreme differential rotation with this surface rotation velocity will be detectable using the values of the eigenfrequencies alone.

The frequency results for the 240 km s^{-1}model, shown in Figure 3.7 for $l_o = 0$, are slightly more promising. Although we were unable to reliably identify modes above $\beta = 1.0$, the frequencies already differ by more than 1% by $\beta = 1.0$ for the 1H mode, and it seems the differences would be noticeable by $\beta = 0.4$. If this trend continues, as seems likely at least for the F and 1H modes, the frequency differences should be large enough to be detectable in these more rapidly rotating stars. As noted above, for some modes differential rotation causes the frequencies to increase as in Figures 3.7 and 3.8, while for others the frequencies decrease, as in Figure 3.9. These plots do not include the 3H mode, as we found that the scatter in this mode remained a significant fraction of the variation,
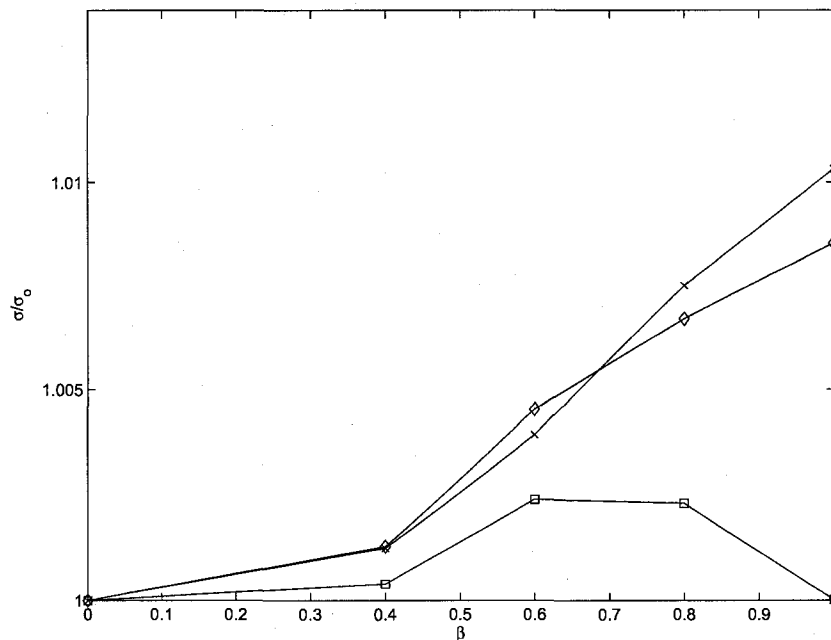
Figure 3.7: Relative frequencies of the $l_o = 0$ modes versus differential rotation parameter β for a model rotating at 240 km s^{-1}. The curves show the relative frequencies for the fundamental (diamond), 1H (x) and 2H (square) modes.

despite the improved radial zoning, and so have chosen not to include it in our discussion.

The effects of differential rotation compared with uniform rotation are shown in Figure 3.9 for the $l_o = 2$ p_2 mode. Differential rotation can change the frequencies by about a percent above and beyond the difference predicted based on surface equatorial velocity alone. The differences are small; about 1% for the most extreme differentially rotating model at 120 km s^{-1}. Based on the frequencies we have calculated, it may be possible to discriminate between uniform and this type of differential rotation, given the right combination of properly identified frequencies. Since frequencies increase relative to the uniformly rotating case for some l_o, and decrease for others, these differences could be used to constrain the rotation. This would require a star with a few positively identified modes, some of which were either $l_o = 0$ or 1, and some of which were either $l_o = 2$ or 3. The number of modes required and the challenges presented by accurate mode identification in massive main sequence stars may make this extremely difficult in practice.
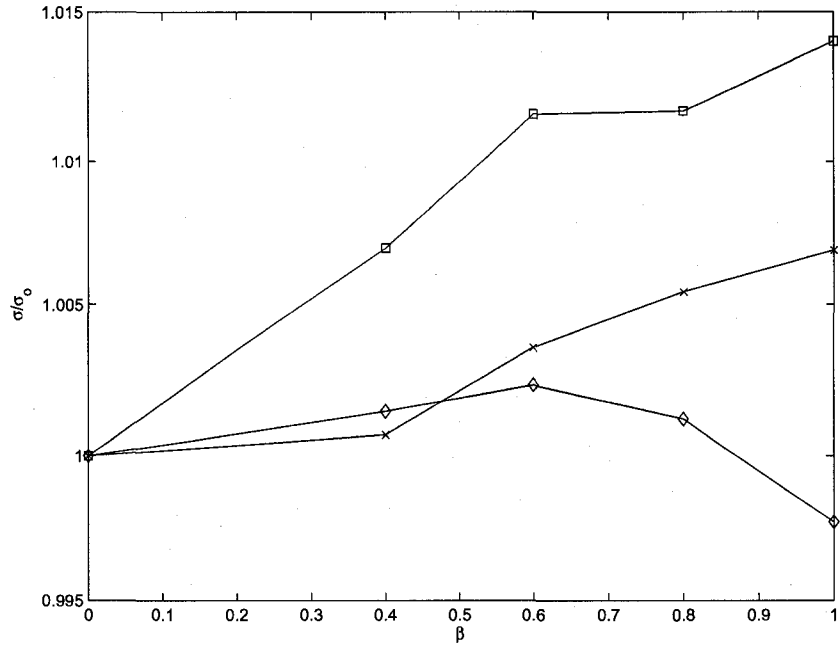
Figure 3.8: Relative frequencies of the $l_o = 1$ modes versus differential rotation parameter for a model rotating at 240 km s^{-1}. Shown are the p_1 (diamond), p_2 (x) and p_3 (square) modes.
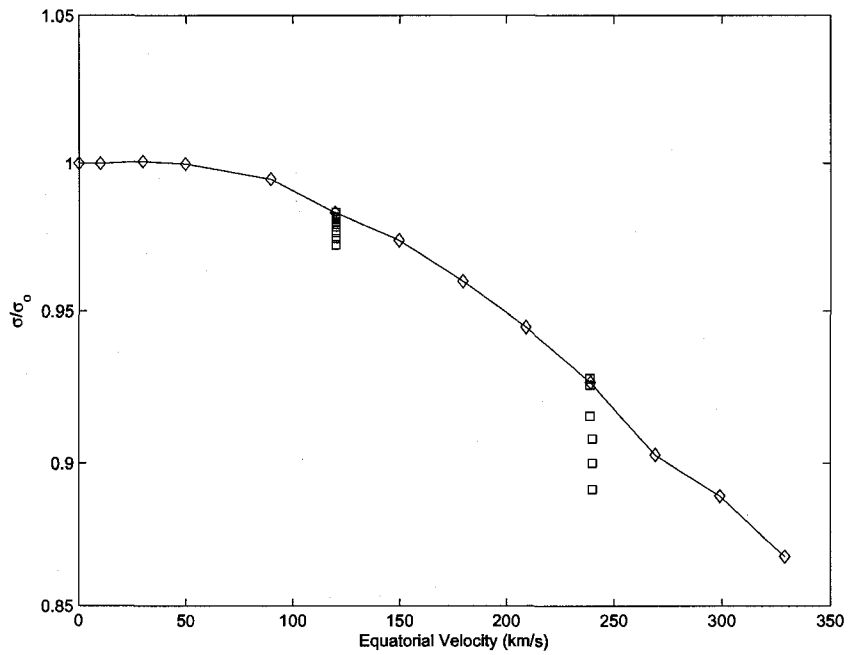
Figure 3.9: The relative effects of differential rotation for the $l_0 = 2$ p_2 mode. The frequencies for differentially rotating models as a function of β at 120 km s^{-1}and 240 km s^{-1}(squares) are superimposed on the uniformly rotating frequencies (diamonds).

3.4 Large Separations

If one considers two stellar models that are in the same evolutionary phase, and appear reasonably close to each other in the HR diagram, the frequencies can be approximately determined from the relevant pulsation constant, Q. As the mass and radius change with position in the HR diagram, so will the frequencies. It is expected that for small changes in mass and radius the frequency separations (either frequency differences or ratios) will change, like Q, much more slowly than the individual frequencies. As a result, the large and small separations are probably more useful than individual frequencies as they are less sensitive to small changes in the models.

3.4.1 Uniform Rotation

The large separation, defined as

$$\Delta\nu_l = \nu_{l,n+1} - \nu_{l,n} \tag{3.16}$$

can provide information about the outer layers of the stellar envelope. The large separation for the $l_o = 0$ mode is shown as a function of rotation rate in Figure 3.10. We note that the overall trend of the large separation for this mode is to decrease as the rotation rate increases. At other l_o the trend is the same and the large separation decreases for every pair of modes considered. The magnitude of the decrease in large separation does increase slightly with increasing l_o, as can be seen by comparing Figures 3.10 and 3.11. For nonrotating ZAMS models, both the frequencies and the large separations decrease as the mass (hence the radius, luminosity and effective temperature) increases. The decrease in the large separation occurs not only because the frequencies decrease, but also because the period ratios increase for increasing ZAMS mass. However, for stars observed approximately equator on, rotation decreases the the perceived luminosity and effective temperature. This offset between the perceived luminosity and temperature and the large separation may be useful as a rotation discriminant. Of course, stars observed nearly pole on show an increase in perceived luminosity and effective temperature, which is in line with the decreasing large separation as the rotation rate increases. Any discriminant of rotation may only be a matter of degree for low
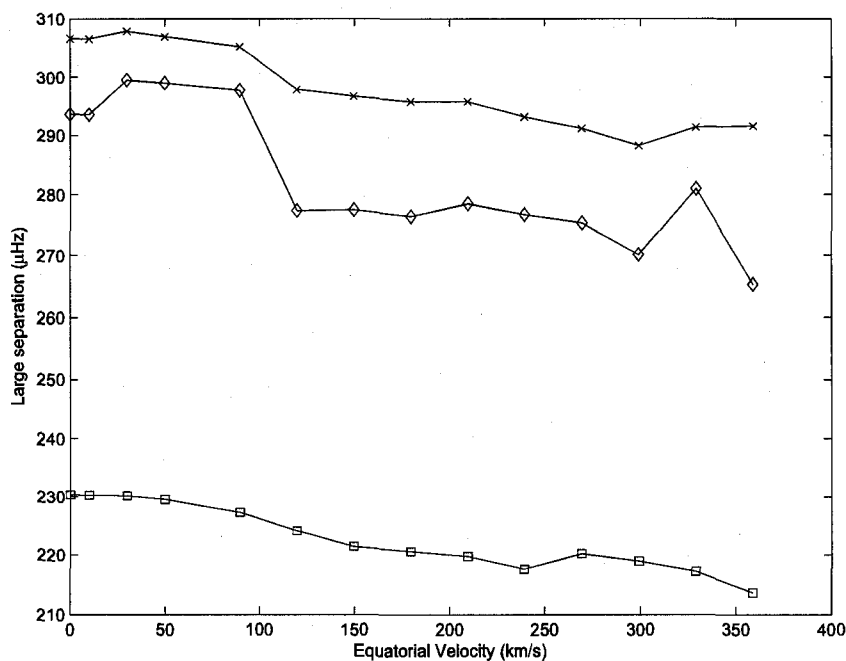
Figure 3.10: The large separation between the 3H and 2H (square), the 2H and 1H (x), and 1H and F modes (diamonds) for modes with $l_o = 0$.

inclination objects.

We noted in section 3.3.1 that the decrease in the frequencies with increasing rotation cannot be explained purely by the decrease in the mean density (i.e., a constant Q). The mean density decreases faster than the pulsation periods increase as the rotation rate increases. Interestingly, the decrease in the large separation for $l_o = 0$ in Figure 3.10 is almost entirely offset by the mean density so that $\Delta\nu(\rho_\odot/\rho)^{1/2}$ is nearly constant, as discussed by Ulrich (1986) and Reese *et al.* (2008). The mean density does not offset the steeper decline in the large separation for the $l_o = 2$ modes shown in Figure 3.11.

3.4.2 Differential Rotation

The large separations provide information about the region near the surface of the star, while the frequencies are more global properties. As discussed above, the separations are less sensitive to small changes in the mass or radius of the star, but since they probe the surface region, may provide information about changes in this region as a result of rotation. A comparison of Figures 3.2 and
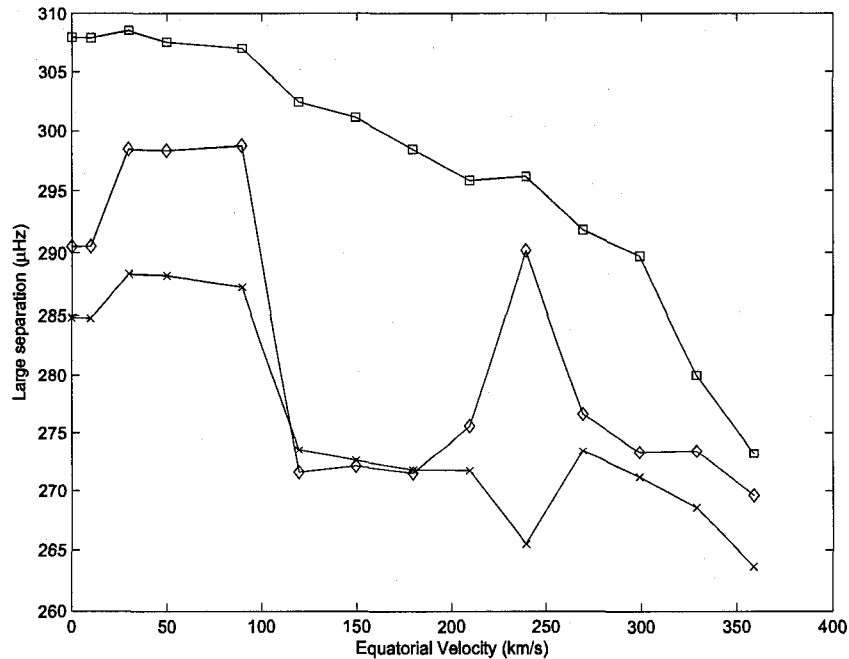
Figure 3.11: The large separation for the $l_o = 2$ modes as a function of rotation velocity. Shown are the separations between the p_1 and f modes (diamonds), the p_2 and p_1 modes (x) and the p_3 and p_2 modes (squares).

3.3 shows that the polar radius is significantly more affected by differential rotation than the radius at lower latitudes. This kind of effect may be detectable using the large separations. Indeed, based on the results in the previous section, we expect there to be significant differences in the period differences, as we have found that differential rotation can sometimes introduce a significant shift in only one or two of the harmonics.

The large separation for the $l_o = 0$ modes of a differentially rotating model with surface equatorial velocity of 120 km s^{-1} are shown in Figure 3.12. The large separations shown in this plot show very little change with increasing β, much less than the differences shown in Figure 3.10. The same lack of variation is seen for all modes. Given that the large separation probes the surface regions, this might be regarded as somewhat surprising because changing the β does change the surface configuration, particularly near the rotation axis.

At 240 km s^{-1}, the large separations, shown in Figure 3.13, are again quite constant over the region shown. Most separations either remain constant or show a slight increase, at least to $\beta = 0.6$,

Figure 3.12: The large separation for the $l_o = 0$ modes of a differentially rotating model with surface equatorial velocity of $120\,\mathrm{km\ s^{-1}}$, plotted as a function of differential rotation parameter β. Symbols are the same as Figure 3.10.

at which point some of the higher order separations decrease slightly. Again, this is different from the trend seen in the uniformly rotating models. Particularly at high β, the separations moving in different directions may allow constraints to be placed on observed stars. The differences begin to become noticeable at $\beta \approx 0.6$ for most of the high order modes considered. However, for most modes the large separation never differs by more than a few μHz. As for the frequencies, it seems that the large separations are unlikely to produce any very refined constraints on the internal rotation rate, at least for this particular rotation law.

3.5 Small Separation

Asymptotic theory (Tassoul, 1980), which predicts that the large separation should be approximately constant as n gets large, also predicts near degeneracy between modes with the same value of $n + l/2$:

$$\nu_{l,n} \simeq \nu_{l+2,n-1} \qquad (3.17)$$

Figure 3.13: The large separation of the $l_o = 0$ modes for a differentially rotating model with surface equatorial velocity of 240 km s^{-1}. Symbols are the same as Figure 3.10.

The deviations from this degeneracy are defined as the small separation:

$$d_{l,n} = \nu_{l,n} - \nu_{l+2,n-1} \simeq -(4l+6)\frac{\Delta\nu}{4\pi^2\nu_{l,n}}\int_0^R \frac{dc}{dr}\frac{dr}{r} \qquad (3.18)$$

where c is the sound speed. The sound speed changes most rapidly in the core of the star, so the integral on the right hand side of Equation 3.18, and hence the small separation, is dominated by the structure in the core.

3.5.1 Uniform Rotation

At slow uniform rotation, the size and shape of the convective core is nearly unaltered by the rotation, and one would expect the effects on the small separation to be minimal. Figure 3.14 shows this to be true, but also shows that the small separation for higher n increases markedly with rotation rate once the rotation exceeds approximately 150 km s^{-1}. There are slight changes to both the shape and relative size of the convective core with rotation, although the absolute mass and radius of the
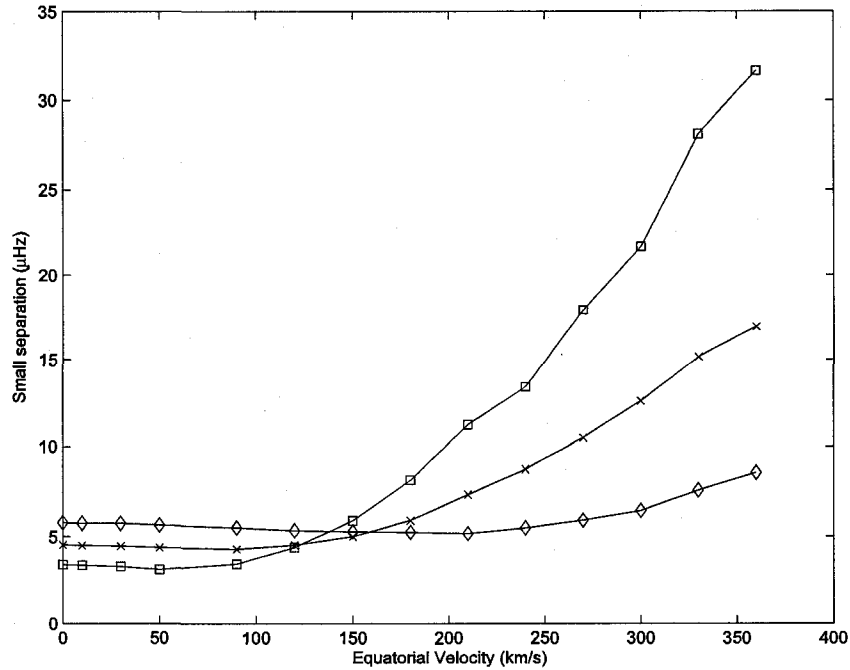
Figure 3.14: Small separation for the $l_o = 0$ and 2 modes as a function of surface equatorial velocity. Shown are the separations between the $l_o = 0$, 3H - $l_o = 2$, p_2 modes (squares), $l_o = 0$, 2H - $l_o = 2$, p_1 modes (x) and $l_o = 0$, 1H - $l_o = 2$, f modes (diamonds).

core change only slightly. It is not obvious why the small separation increases so markedly.

Small separations are frequently used as probes of the core structure of stars, and can be used to constrain overshooting and core composition (Soriano & Vauclair, 2008). Their results indicate that convective core overshooting causes a slight decrease in the small separations, with the effect becoming more pronounced as the star evolves. This slight trend is opposite to that produced by at least moderate rotation, which appreciably increases the small separation. Clearly, this is a situation in which caution must be exercised when using observed modes to constrain conditions deep in the stellar interior.

3.5.2 Differential Rotation

For differentially rotating models, the overall trend is the same, with small separations increasing with increasing differential rotation. However, Figures 3.15 and 3.16 show that the variation in small separation is much less than for uniformly rotating models. The trends are consistent with
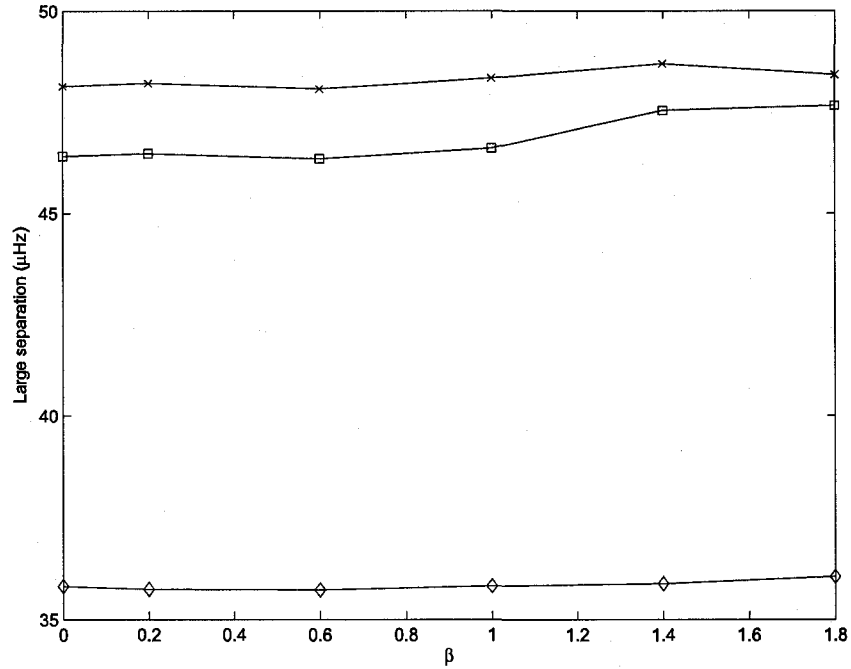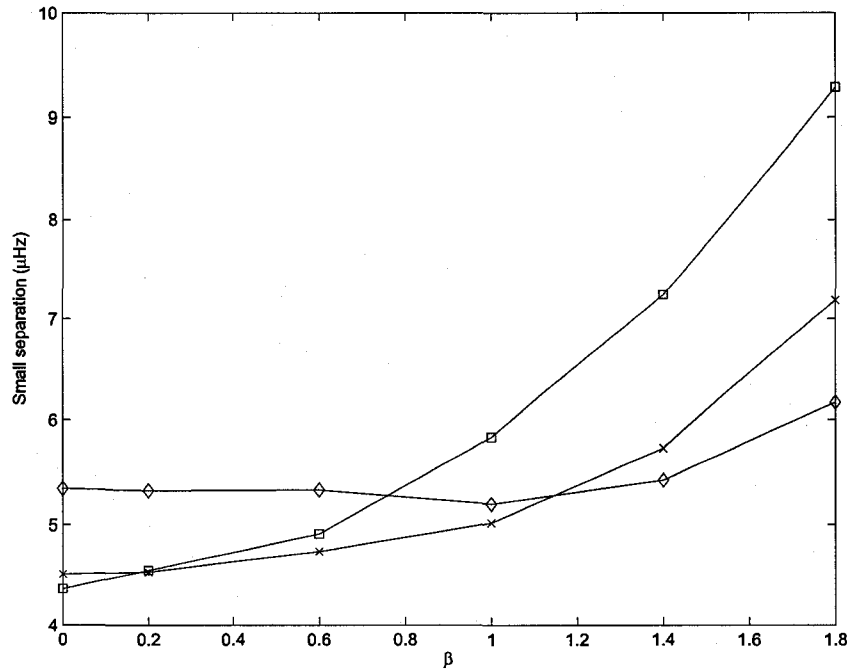
Figure 3.15: Small separations for the even modes for a differentially rotating model with surface equatorial velocity of 120 km s^{-1}, plotted as a function of differential rotation parameter β. Symbols are defined as in Figure 3.14.

the relationship between the effects of β and those of increasing the uniform rotation rate as shown in Figure 3.9. The effects of increasing β on the convective core mimic to some extent those of increasing the uniform rotation rate, although high values of β do make the convective core more oblate. The different effects of β on the large and small separations is understandable in that increasing β increases the rotation and its effects near the rotation axis, and this certainly includes the convective core. However, this trend of increasing β producing similar trends to increasing uniform rotation rate does not give us confidence that we have a useful tool for diagnosing a rotation law of the kind we have considered through the small separation.

3.6 Conclusion

We have investigated the effects of uniform and differential rotation on pulsational eigenfrequencies. For uniformly rotating models, we have found that the frequencies decrease as rotation rate increases
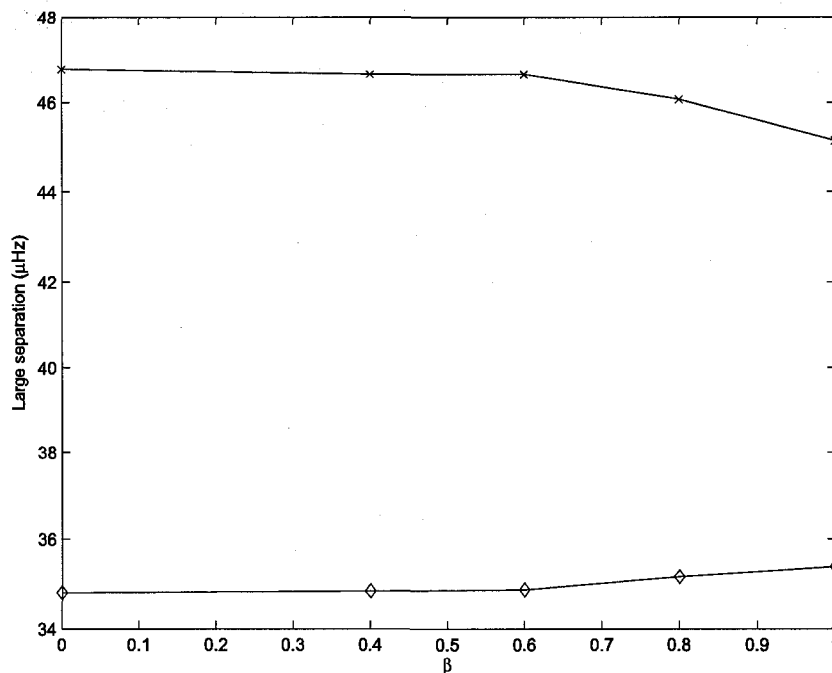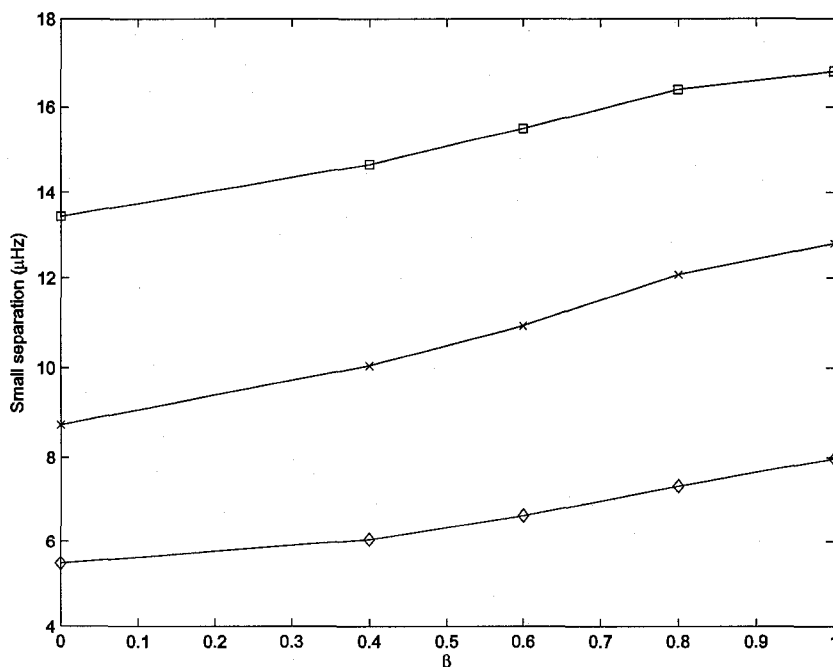
Figure 3.16: Small separations for the even modes of a differentially rotating model with surface equatorial velocity of 240 km s^{-1}. Symbols are defined as in Figure 3.14.

for all values of l_o and n considered here, although the rate of decrease varies with the mode in question. While this frequency behavior is expected assuming the period-mean density relation applies, the frequency changes are much smaller than the period-mean density would suggest. We do find a pulsation constant being approximately constant if we use the surface radius at a colatitude of about 40° in the period-mean density relation, although this radius does not represent the mean density.

For the differential rotation law considered here, we find the frequencies at a given velocity may either increase or decrease, depending on l_o, with increasing differential rotation, relative to the uniformly rotating model. However, the overall effects in all cases are comparatively small, with maximum differences typically on the order of 1% when compared to the uniformly rotating case.

Uniform rotation decreases the large separation by several μHz (< 10) over the entire range of rotation (0 - 360 km s^{-1}) considered here. The large separation was virtually unchanged ($< 1\ \mu$Hz) from that of uniform rotation for the range of differential rotation parameters considered here, despite

the noticeable change in the surface shape. Although this change in shape is noticeable, it is still considerably smaller than the change produced by uniform rotation. Both uniform and differential rotation increase the small separation. The small separation can change markedly over the range of uniform rotation considered, while the dependence of the small separation on the rotation profile is more modest but not inconsistent with the other effects produced when comparing uniform and differential rotation. The effects of rotation on the frequencies and separations are generally large enough that rotation must be considered in the asteroseismology of these upper main sequence stars. While the precise rotation rate at which one must be concerned with rotation depends on the level of accuracy achievable, it is certainly no larger than 100 km s^{-1} for our 10 M$_\odot$ ZAMS models.

Although we have shown there can be significant differences in the pulsation properties of rotating stars, it is not clear that these results can actually be used to constrain the interior rotation rate. Given the possible combinations of effects from rotation rate and distribution, the mass of the star, convective overshoot, evolutionary stage, etc, it seems unlikely that pulsation properties will give a unique solution, particularly if the number of observed modes is modest or cannot be properly identified. However, we have found that some combinations of modes constrain some of these properties.

Chapter 4

Effects of Rotation on Photometric Mode Identification of Pulsating Stars[1]

Mode identification is essential for observed pulsation frequencies to be used to study stellar interiors. In this paper we investigate the effects of rotation on photometric mode identification. We use 2D modelling of stellar structure and pulsation, combined with plane parallel NLTE model atmospheres to calculate photometric amplitudes for $10M_\odot$ ZAMS models with rotation rates from 0 to 240 km s^{-1}. We have examined the effects of changing inclination angle on the photometric amplitudes. In non-rotating stars, the effects of changing inclination angle are noticeable, but small enough that they are unlikely to affect mode identification. In stars rotating moderately rapidly, however, we find the inclination effects in some modes are sufficiently large that the relative amplitude as a function of wavelength is not unique. It may be impossible to ever rule out $l = 2$ pulsation for uniformly rotating stars. For $l_o \neq 0$, these results are unaffected by the radial order of the mode. The $l_o = 0$ mode shows larger variation in photometric amplitudes for the 1H mode than for the F mode, but not large enough to cause additional ambiguity in mode identification.

4.1 Introduction

Asteroseismology has great potential to add to our understanding of the interior structure of stars, but in order to utilize this, we must be able to accurately identify the observed modes. A complete mode identification would include all three quantum numbers (radial order n, latitudinal order l, and azimuthal order m). In solar type pulsators, a large number of modes can be observed, and regular patterns in the frequency spectrum can help with mode identification (Daszyńska-Daskiwicz,

---

[1]The contents of this chapter have been submitted to the Astrophysical Journal.

2008). Unfortunately, for more massive main sequence pulsators, such as δ Scuti and β Cephei stars, only a few modes are observed, and other approaches to mode identification must be used. This can be done using the line profile variations in spectroscopic observations (Balona, 1986a,b, 1987, 1989). These spectroscopic observations, however, require very high dispersion spectra with a high signal-to-noise ratio (Balona & Evers, 1999). This type of spectroscopy is far more time consuming than photometric observations, so reliable mode identification techniques using photometric observations would be advantageous.

A method for identifying the degree (l) of a mode from bolometric observations was originally developed by Dziembowski & Goode (1992), and later extended to multicolor photometry by Stamford & Watson (1981). This technique has since been expanded upon and used by several groups (Watson, 1988; Cugier *et al.*, 1994; Heynderickx *et al.*, 1994). These authors derived an expression for the photometric amplitude of a pulsating star as a function of wavelength, l and m. Using this technique for a variety of theoretical and observational spectra, it is possible to determine l, as the amplitude will vary as a function of wavelength, with the pattern of variation depending on l. It is also possible to perform photometric mode identification using color-phase observations. However, for β Cephei stars, the phase differences are small, and the wavelength data provide more information (Balona & Evers, 1999).

Photometric mode identification has the potential to be particularly useful for main sequence pulsators, such as β Cephei stars. Observationally, these stars are often multi-periodic, and these are thought to be low degree modes (Stankov & Handler, 2005). A few β Cephei stars are also known to be rapid rotators (Slettebak, 1949), an effect neglected by most previous work. Rotation has been considered by Daszyńska-Daskiwicz *et al.* (2002), although they focused on the effects produced by coupling of modes in rotating stars. Rotation is known to affect the variation of eigenfunctions across the surface of the star (Clement, 1998; Lovekin & Deupree, 2008a). As rotation increases, higher order spherical harmonics begin to make important contributions to the shape of the eigenfunction. Thus, the horizontal variation of an $l = 0$ mode in the non rotating star can look like an $l = 2$ mode in a sufficiently rapidly rotating model. How much this effect changes the photometric amplitudes

used in mode identification is unknown.

In this paper, we use a 2D stellar structure code to calculate accurate stellar models, including deformation produced by rotation at velocities from 0 to 240 km s^{-1}. Here, we use the structure models and pulsation frequencies for $l \leq 3$ calculated by Lovekin & Deupree (2008b). We have applied these perturbations to our stellar models and calculated spectra for the perturbed models at maximum compression and expansion. These spectra were combined with response functions for various filter systems to calculate photometric amplitudes for pulsation modes. Our numerical models are discussed in more detail in §4.2. The effects of stellar inclination are discussed in §4.3, and the effects of rotation are discussed in §4.4. These effects are considered for higher order harmonics in §4.5, and our conclusions are summarized in §4.6.

4.2 Numerical Methods

Our stellar models are calculated using the 2D stellar evolution code ROTORC (Deupree, 1990, 1995), allowing us to self-consistently model the surface and structure of the star for rotation rates from zero up to near-critical rotation. This code has recently been updated to allow for the calculation of differentially rotating models (Gillich *et al.*, 2008). As in Lovekin & Deupree (2008a,b), we focus on uniformly rotating 10 M$_\odot$ ZAMS models with X=0.7, Z=0.02. We use the OPAL opacities (Iglesias & Rogers, 1996) and equation of state (Rogers, Swenson & Iglesias, 1996) in these calculations. These models are fully 2D, with 10 angular zones from pole to equator and up to 581 radial zones. Using these models, we calculated uniformly rotating stellar models with surface equatorial velocities 0-360 km s^{-1} (Lovekin & Deupree, 2008b). Here we will utilize uniformly rotating models with surface equatorial velocities of 0, 120 and 240 km s^{-1} from that work.

We calculated linear perturbations to the static structure with a 2D linear, adiabatic pulsation code, NRO (Clement, 1998). This code solves the linear adiabatic perturbation equations on a 2D spherical grid. The solution is expressed in terms of 5 variables, related to the radial and latitudinal displacement perturbation, the pressure and gravitational potential perturbations, and the radial derivative of the gravitational potential perturbation. In this way, all of the relevant linearized

equations can be expressed in the general form

$$\partial_r y_i = f(y_i, \partial_r y_{j \neq i}, \partial_\theta y_i).$$

(4.1)

The coefficients of these perturbed equations can be put in a band-diagonal matrix and solved. NRO can include up to nine angular zones in the eigenfunction solution, performing one radial integration for each angle included. This gives the solution at N angles, which can subsequently be decomposed into the contributions of individual spherical harmonics through the use of Fourier transforms. Throughout this paper, we have used N = 6. Based on the calculations of Lovekin & Deupree (2008a), six spherical harmonics are sufficient to accurately calculate the eigenfrequencies for the most rapidly rotating models discussed here. We have calculated photometric amplitudes for axisymmetric ($m = 0$) modes with $l_o \leq 3$.

One of the effects of rotation is that a given mode is no longer composed of a single spherical harmonic, but a linear combination of several. As such, the angular quantum number l is no longer valid as a way of identifying modes. However, a given mode of a rotating model can be traced backwards to a specific mode in the equivalent non-rotating model. We designate modes using l_o, the l value of the specific mode in the non-rotating model.

The perturbations calculated by NRO are applied to the surface properties (T_{eff}, $R(\theta)$, $\log g_{eff}$) calculated by ROTORC. We use the scaled Lagrangian displacement perturbations (ξ_r, ξ_θ) and Eulerian perturbation to the gravitational potential. These perturbations are then simply scaled to physical units before being added to the static stellar structure variables. The Eulerian pressure perturbation is calculated from the displacement perturbation

$$\delta P = -\Gamma_1 P (\nabla \cdot \xi) - \xi \cdot \nabla P,$$

(4.2)

and the Lagrangian temperature perturbation is calculated from the pressure perturbation using

$$\frac{\delta P}{P} = \frac{\Gamma_2 - 1}{\Gamma_2} \frac{\delta T}{T}$$

(4.3)

where Γ_1 and Γ_2 relate to the adiabatic response of the pressure to changes in the density and temperature respectively (eg., Cox & Giuli 1968). We solve for the Eulerian temperature perturbation and apply it to the static temperature. Following Stamford & Watson (1981) and Heynderickx *et al.* (1994), we have assumed the temperature perturbation is equal to the effective temperature perturbation, $\delta T/T = \delta T_{eff}/T_{eff}$ at the appropriate optical depth ($\tau = 2/3$). Dupret *et al.* (2002) have taken non-adiabatic effects into account and have shown that this is not necessarily true, particularly deep within the atmosphere. This is done by assuming that the atmosphere remains in radiative equilibrium rather than using the diffusion approximation. This improves the treatment of the temperature in the atmosphere. Our static models use the Eddington approximation, and lack the zoning at the surface to be able to effectively apply the approach suggested by Dupret *et al.* (2002). Because we are making a relative comparison, we believe the effects of using the adiabatic approximation should not be too severe.

We have calculated the surface properties of the perturbed structure model at maximum compression and expansion. The pulsation code, NRO, is a linear code, and so does not provide any information on the amplitude of the pulsations. We have chosen to scale the amplitudes by fixing the value of $\delta r/r$ at the pole. Typically, we set $\delta r/r = 0.01$, although for some models this has been raised or lowered to keep the perturbations large enough to be noticeable and yet still small enough to be within the linear regime. The variation in the surface properties of the perturbed models can be used to generate spectral energy distributions (SEDs) using a spectral synthesis code, described briefly below. A more detailed discussion can be found in Lovekin (2005) and Lovekin *et al.* (2006). This code takes plane-parallel NLTE atmospheres produced by the PHOENIX code (Hauschildt & Baron, 1999) and calculates a synthetic SED for a deformed star. We then use the log of the ratio of the fluxes at these two phases in selected photometric filters to calculate the photometric amplitudes. These photometric amplitudes are normalized by the amplitude in the bluest filter.

Our model atmospheres are generated using PHOENIX, which self-consistently solves the radiative transfer equation and the NLTE statistical equilibrium (SE) rate equations for many species and overlapping transitions (Hauschildt & Baron, 1999). Short *et al.* (1999) have greatly increased the

number of species and ionization stages treated in SE by PHOENIX. Atomic data for the energy levels and b-b transitions have been taken from Kurucz (1994) and Kurucz & Bell (1995). We have generated the resulting intensity as a function of angle relative to the surface normal for the wavelength region 3000-10000 Å with $\Delta\lambda = 0.02$ Å, giving a resolution of R $= \lambda/\Delta\lambda = 150\,000$.

The surface variations as a function of colatitude, from ROTORC and NRO, and the intensity grid produced by PHOENIX are used as inputs for our atmospheric integrator code (CLIC). We divide the surface of the model into a mesh of 200 colatitudinal (θ) zones and 400 longitudinal (ϕ) zones. For each mesh zone, the effective temperature and surface gravity are determined from the ROTORC model and the perturbations. The appropriate atmospheric intensities are read in from a grid of models in T_{eff} and log$g$. CLIC then interpolates among these models to determine the intensity in the direction of the observer from each grid zone. To determine the total flux, we must evaluate the integral

$$F_\lambda = \int_\theta \int_\phi \frac{I_\lambda(\xi(\theta,\phi))}{d^2} dA_{proj} \tag{4.4}$$

where θ is the colatitudinal coordinate, ϕ is the longitudinal coordinate, $\xi(\theta,\phi)$ is the angle between the local surface normal and the line of sight to the observer, d is the distance to the object, dA_{proj} is the projected surface area element as seen from the direction of the observer, I_λ is the intensity at a given wavelength, and F_λ is the flux at a given wavelength. For more details on the method of solution of this integral, refer to Lovekin *et al.* (2006).

The output of this integration is a set of 10 spectra at inclinations from $i = 0$ to 90°. Although CLIC is capable of calculating Doppler broadening, the effects are not important when considering the flux in broad-band filters, as is done here. A test comparing the flux ratio in one filter with and without Doppler shifting showed no difference, so we have neglected Doppler effects in the spectra used in this work.

The uncertainty in our spectral calculation is approximately 6 %, and is dominated by numerical errors in the interpolation. This error corresponds to a difference in the logarithmic flux ratio of 0.025. We have neglected amplitude curves with an amplitude less than this in the bluest filter. Amplitudes this low were most commonly found for the $l_o = 2$ modes, where typically only a few

amplitude curves are included. The $l_o = 1$ and 3 modes, when viewed close to equator on also have very low amplitudes, as the models have nearly the same spectra at maximum expansion and compression because of the asymmetry about the equator.

We have calculated the photometric pulsation amplitude at maximum compression and expansion for the Walraven (Walraven & Walraven, 1960), Strömgren (Strömgren, 1956), and Johnson (Johnson, 1965) filter systems. The filter response functions for these filter systems were taken from the Asiago Database on Photometric Systems (ADPS) (Moro & Munari, 2000). For simplicity, we have chosen to show results in the Walraven filter systems only. Previous research (eg., Heynderickx *et al.*1994) seems to indicate that this filter system provides more information for mode identification.

4.3 Inclination Effects

Using the codes described above, we have calculated photometric amplitudes as a function of inclination of the star. For non-rotating stars of course, there is no preferred axis, as the star is spherically symmetric. However, non-radial pulsation does introduce a distinct axis to the stellar model. This is still somewhat arbitrary, as a given spherical harmonic with one axis can be represented mathematically in terms of a linear combination of spherical harmonics with a different axis. As discussed in Heynderickx *et al.* (1994), a particular choice of polar axis does not imply a particular pulsation axis, and so they were justified in choosing the polar axis to coincide with the direction to the observer. Throughout their paper, they consider pure spherical harmonics, and do not take into account the effect of changing the viewing angle on the resulting photometric amplitudes. We assume the pulsation axis coincides with rotation axis, but the direction to the observer is free to change. The effects of this change are addressed in this section.

4.3.1 Non-Rotating Model

The angle at which a model is viewed will produce changes in the observed photometric amplitudes, the exact amount depending on the mode. As a first step towards disentangling this relationship, we first consider the dependence of the relative photometric amplitudes on the changing angle of

inclination in a non-rotating, pulsating 10 $M_\odot$ ZAMS model. In this case, the range of photometric amplitudes produced by changing inclination is small for $l_o = 0\text{-}2$, as shown for the Walraven filter system in Figure 4.1. For the radial mode, as one might expect, there are no differences at all as a function of inclination. At $l_o = 1$, there are slight differences, but the effects are less than 0.5% at the reddest wavelengths. This is small enough that they are unlikely to cause any confusion, or even be noticeable when comparing theory and observations in practical situations. For the $l_o = 2$ mode, the differences are larger, around 2%, which may be large enough to be detectable, but are unlikely to cause any confusion with other modes. Figure 4.1 only shows the $l_o = 2$ modes for $i = 70, 80$ and $90°$, as at lower inclinations the flux ratios were too low to be reliable (< 0.025), based on previous calculations (Gillich *et al.*, 2008). Including all inclinations would increase the variation in photometric amplitudes, but the variation remains small enough to avoid ambiguity in mode identification. The $l_o = 3$ mode also shows significant variation with inclination, with variation as large as that between $l_o = 0$ and 1. However, the slope of this curve at the reddest wavelengths should be sufficient to distinguish it from these modes. Figure 4.1 shows the $l_o = 3$ mode at $i = 0$ and $70°$, rather than at pole and equator, as the equator appears to be a special case. For the odd modes, which are antisymmetrical at the equator, the two spectra $180°$ out of phase are nearly identical because the northern hemisphere at maximum compression looks like the southern hemisphere at maximum expansion. The resulting differences in the photometric amplitude should be zero. Numerically, the cancellation is not quite exact, but the resulting ratios are too small to be reliable. Thus, odd modes viewed nearly equator on ($i \sim 90°$) are not considered further. It appears that for non-rotating stars, the inclination effects, while present, do not pose a problem for photometric mode identification. This is true for all three filter systems considered.

We have compared our results for the Walraven filters with the results of Heynderickx *et al.* (1994) for β Cephei stars. The primary difference in approach is that their calculations were done using LTE atmospheres, while our calculations use non-LTE atmospheres. Overall, the trends for the $l_o = 0, 1$ and 2 modes look quite similar. At the reddest wavelengths (V band), our amplitudes are within a few percent of those found by Heynderickx *et al.* (1994). There are differences at

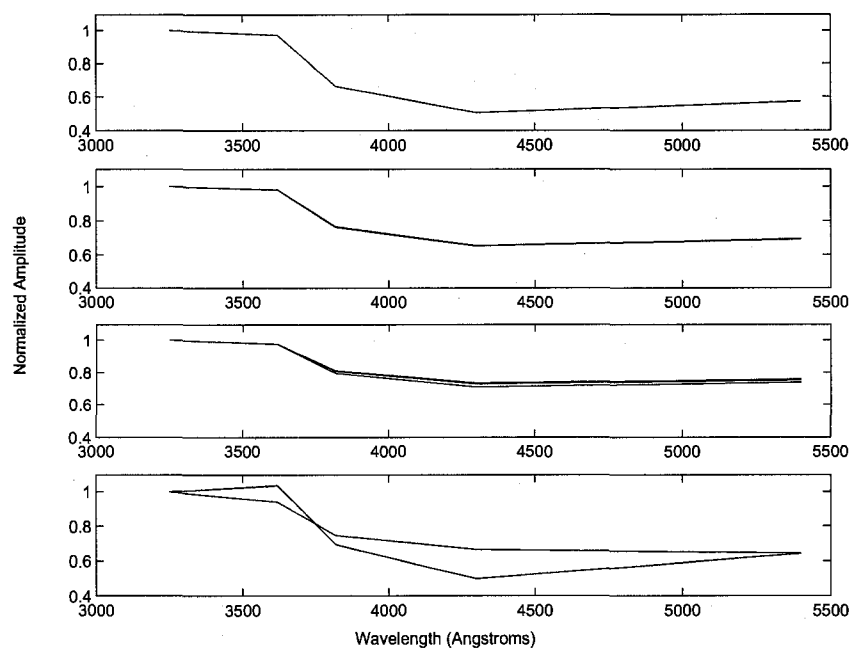Figure 4.1: The Walraven photometric amplitudes for a non-rotating 10 $M_\odot$ model. Shown are the maximum and minimum amplitudes as a function of inclination for (from top to bottom) $l_o = 0$, $l_o = 1$, $l_o = 2$ at $i = 70$, 80 and 90° (see text for discussion) and $l_o = 3$. For non-rotating stars, the inclination effects are generally small, and are unlikely to cause any confusion in photometric mode identification.

bluer wavelengths. We find a slightly lower amplitude in the U band (3670 Å), about 5 %. The largest difference occurs in the B band, centered at 4295 Å. In this filter, we find our amplitudes are about 15 % lower than the Heynderickx *et al.* (1994) results. This region of a NLTE spectrum for a uniformly rotating stellar model with $T_{eff} \sim 25800$ K is shown in Figure 4.2. This region is dominated by H-γ. Previous work (Lovekin *et al.*, 2006) indicates that we have sufficient resolution over the stellar model surface, as well as in temperature to produce accurate synthetic spectra, so we do not believe resolution is the source of the differences. Since the differences in this wavelength region occur in both rotating and non-rotating stars, it is likely not a result of rotation. It is possible that the differences arise from differences between LTE and NLTE spectral calculations. In our NLTE models, the lower atomic energy level which forms the line is less populated than in LTE, so there will be less absorption, and hence more flux in the NLTE models. For photometric mode identification, we look at the ratio of two spectra, so systematic differences between LTE and NLTE should have no effect. If the amount of absorption changes with temperature, this could explain the differences between the NLTE and the LTE results. Indeed, we have found that as the temperature increases, the departure coefficients increase, and the level populations become closer to the LTE populations. This means that lines produced at lower temperatures will have more flux than the LTE model at the same temperature. The difference in flux between nonLTE and LTE will increase as the temperature decreases (models at higher temperatures will be closer to the LTE flux than models at lower temperatures). When the ratio of the fluxes is considered, the ratio of the nonLTE fluxes will be lower than the ratio of the LTE fluxes. This is indeed what we find when we compare our amplitude ratios in the Walraven V band with those calculated by Heynderickx *et al.* (1994). Also visible in this region are a few emission lines, which would not be present in the LTE spectra.

The $l_o = 3$ mode was omitted by Heynderickx *et al.* (1994), who found that "the wavelength dependence for $l = 3$ is markedly different from the wavelength dependence for the other values of l". This trend appears in our results as well. Their observations showed no stars with wavelength dependence compatible with that of the $l_o = 3$ modes, and so they did not include these curves in their analysis.
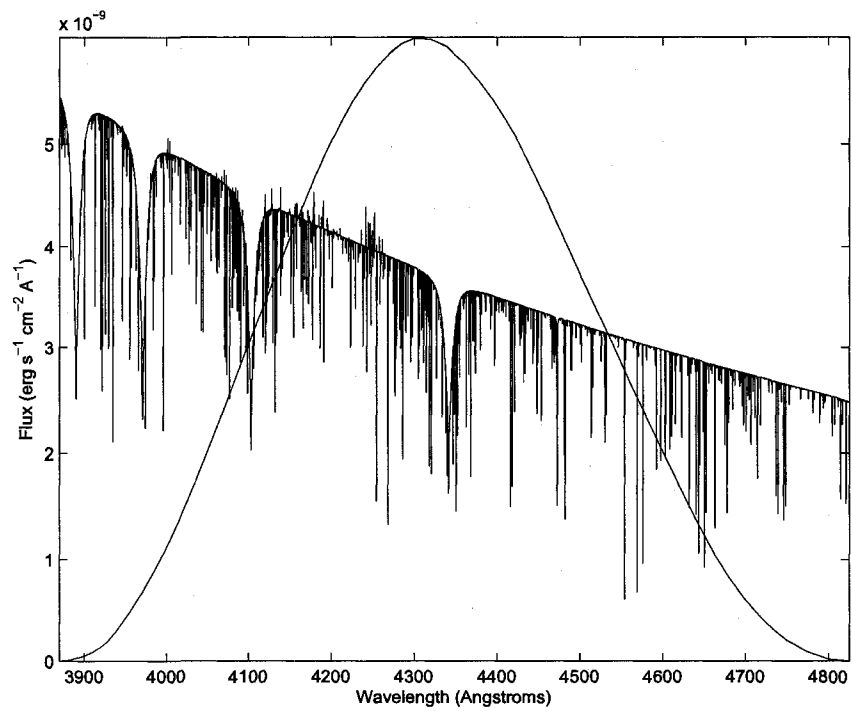
Figure 4.2: The NLTE spectrum in the region of the Walraven B band at a temperature of 25800 K. Overplotted is the filter response function for the B band.

4.3.2 Uniformly Rotating Models

As rotation is introduced, the initially pure spherical harmonic pulsation modes become contaminated by spherical harmonics of higher or lower l. One of the results of this will be to increase the variation in photometric amplitudes produced by changing inclination angle. This has the potential to make mode identification more complicated, as a given mode could have a range of photometric amplitudes, and could potentially overlap the patterns of other modes.

At 120 km s^{-1} ($0.3\Omega_c$, where Ω_c is the rotation rate at which gravity is balanced by the centrifugal force at the equator), the spread in photometric amplitude produced by changing the angle of inclination shown in Figure 4.3 is generally not much larger than in the non-rotating case. For the $l_o = 0$ and 1 modes, there is a slight variation in amplitude, about 2 % and 1 % respectively in the Walraven filters. In some filter systems, this spread may be large enough to be noticeable when comparing theory and observations, but it is not large enough to cause any ambiguity in mode identification.

The variation in amplitude as a function of inclination for the $l_o = 2$ and 3 modes is much larger. For the $l_o = 2$ mode, the normalized photometric amplitude as a function of inclination ranges from 0.5 to 0.7 at the redder wavelengths, which covers nearly the entire photometric amplitude variation of the other modes. Observed close to pole on, the $l_o = 2$ mode would be mistaken for a $l_o = 0$ mode, but viewed closer to equator on, this mode would mimic an $l_o = 1$ mode. The agreement between the $l_o = 2$ and $l_o = 1$ modes is closest for $i = 60°$, at which inclination the observer is looking almost directly at the node for this particular $l_o = 2$ mode ($\theta \sim 53°$).

The $l_o = 3$ mode, although it also covers a large range of amplitudes does not appear likely to produce confusion, because the photometric amplitudes as a function of wavelength have a different slope from the other three modes considered here, as shown in the bottom panel of Figure 4.3. At intermediate inclinations ($i = 40°$), the amplitude ratios for the $l_o = 3$ mode are approximately parallel to the $l_o = 0$ and 1, but the amplitude ratio is sufficiently higher than the $l_o = 0$ and lower than the $l_o = 1$ to keep the modes distinct. This is shown in Figure 4.3 for the Walraven filters, but occurs in all three filter systems.
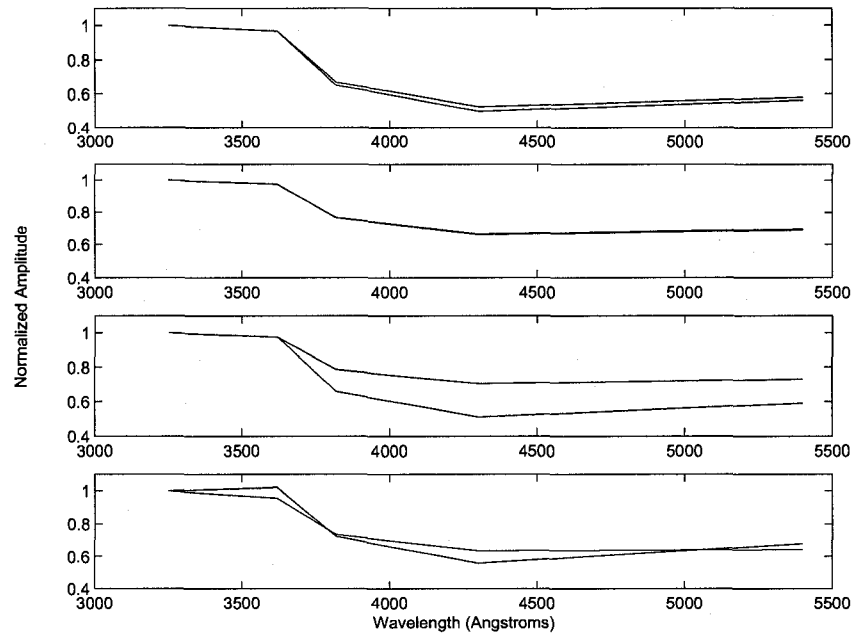
Figure 4.3: The maximum range in inclination of the Walraven photometric amplitudes for a 10 $M_\odot$ model uniformly rotating at 120 km s^{-1}. Shown are the range of amplitude ratios produced by changing inclination angle for, from top to bottom, the $l_o = 0$, $l_o = 1$, $l_o = 2$ and $l_o = 3$ modes. Although the variation in both the $l_o = 2$ and 3 modes overlaps with the $l_o = 0$ and 1 modes, only the $l_o = 2$ could be confused, as the $l_o = 3$ mode has a very different slope.

At 240 km s^{-1}, the results are quite similar to those at 120 km s^{-1}. The spread in photometric amplitude with inclination has increased, particularly for the $l_o = 0$ mode, up to nearly 8 %. As can be seen from Figure 4.4, it is only at this velocity that the inclination effects become significant for the $l_o = 0$ mode. The horizontal variation of the radial eigenfunction for the $l_o = 0$ mode has become significantly contaimnated with higher order spherical harmonics, and the pulsational amplitude differs by as much as 20 % relative to the pure spherical harmonic Lovekin & Deupree (2008a), and even differs by as much as 10-20 % relative to the $l_o = 0$ mode at 120 km s^{-1}. Given this degree of horizontal variation in the eigenfunction, it is not at all surprising that there is a large amount of variation with inclination relative to the more slowly rotating cases.

The $l_o = 0$ and 1 modes are still sufficiently separated in amplitude that confusion between them seems unlikely. There is increased overlap between the $l_o = 0$ and 2 modes as the variation in the $l_o = 0$ modes has increased. As for the 120 km s^{-1} model, the $l_o = 1$ and 3 modes overlap, but unlike at 120 km s^{-1} model, at 240 km s^{-1}, there is the possibility of misidentification because the shapes of the relative amplitude curves are similar. The $l_o = 3$ mode viewed close to equator on ($i = 80°$) is very close to the $l_o = 1$ mode. At lower inclinations, the $l_o = 3$ amplitudes remain in the same range, but, as for the 120 km s^{-1} model, the shape of the curve differs from that of the $l_o = 1$ mode, so misidentification seems unlikely. As for the other two velocities considered, these trends, shown in Figure 4.4, are common to all three filter systems.

As with the model at 120 km s^{-1}, it appears that the $l_o = 2$ mode cannot be distinguished from the other modes, except perhaps in the case of a nearly pole on $l_o = 3$ pulsator. At the more rapid rotation rate however, even the $l_o = 3$ become subject to ambiguity at some inclinations.

4.4   Rotational Effects

As discussed above, rotation increases the variation in photometric amplitudes produced by changing the inclination angle of the star. This is more pronounced in some modes than in others. For example, the $l_o = 1$ mode shows very little variation with changing inclination angle for the rotation rates considered here. In contrast, the amplitude of the $l_o = 2$ mode can vary by nearly 20 %
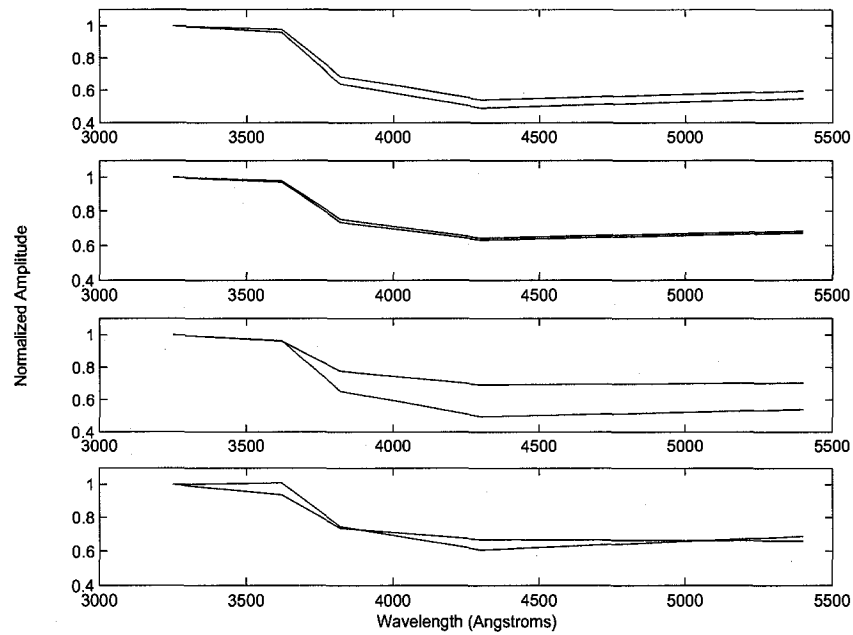
Figure 4.4: The Walraven photometric amplitudes for a 10 $M_\odot$ model uniformly rotating at 240 km s^{-1}. Shown are the maximum and minimum amplitude ratios for (from top to bottom) the $l_o = 0$, $l_o = 1$, $l_o = 2$ and $l_o = 3$ modes. In this case, there is more scope for confusion of mode identification, as the variation in the $l_o = 2$ mode overlaps with all other modes, and the amplitude curve of the $l_o = 3$ mode now follows that of the $l_o = 1$ mode at high inclinations.
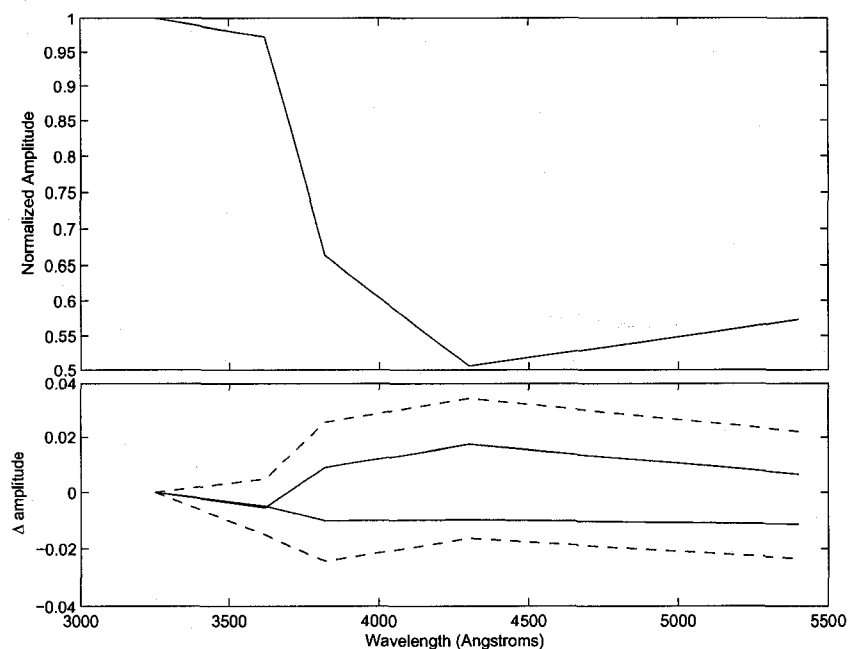
Figure 4.5: Top: The photometric amplitude for the $l_o = 0$ mode in the nonrotating model. Bottom: Maximum and minimum variation in photometric amplitude relative to the nonrotating model for the l_o mode at 120 km s^{-1} (solid) and 240 km s^{-1} (dot-dashed).

with changes in inclination angle. The question remains: for a given inclination and mode, how does the photometric amplitude vary with stellar rotation rate? If the variation in photometric amplitude is large enough with respect to stellar rotation, it may be possible to use photometric mode identification to constrain stellar rotation. Or, depending on the pattern of variation, an increased rotation rate may result in misidentification of modes using photometric techniques. Although we will attempt to discuss the effects of rotation as independent from inclination, in reality the two effects are tightly coupled, and both must be included to understand the resulting photometric amplitudes.

The top panel of Figure 4.5 shows the photometric amplitude for the $l_o = 0$ mode in the nonrotating model, while the bottom panel shows the maximum and minimum variation for models rotating at 120 and 240 km s^{-1}. This figure makes it clear that faster rotation rates increase the variation in photometric amplitudes that could be observed for a given mode. Even with this increase, the amplitude variations of the $l_o = 0$ and 1 modes do not overlap, as illustrated in Figure 4.6.
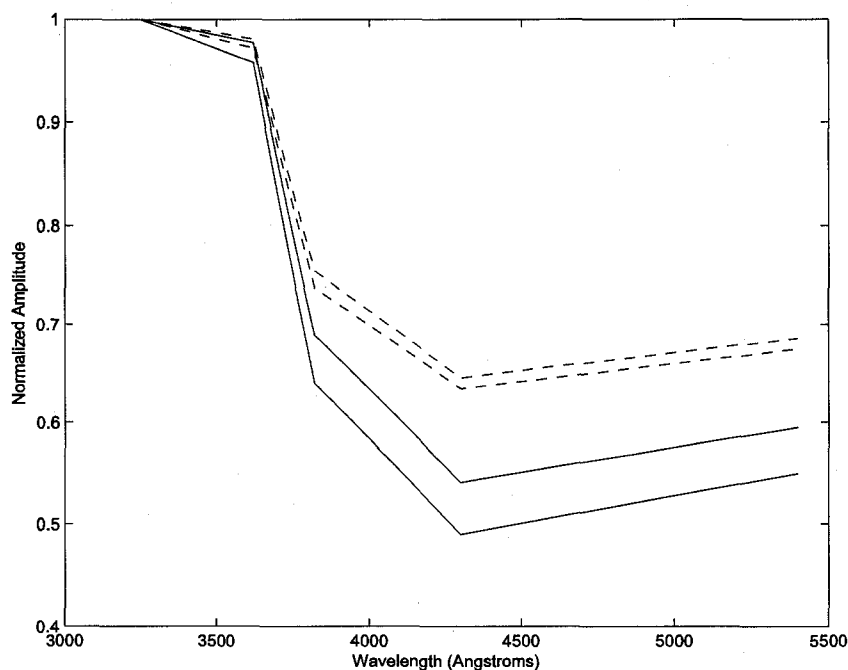
Figure 4.6: Walraven photometric amplitudes of the $l_o = 0$ (solid) and 1 (dashed) modes at 240 km s^{-1}. Although the range covered by the $l_o = 0$ mode has increased significantly, the $l_o = 1$ mode does not vary appreciably with inclination, and the two remain distinct.

As we can decompose the discrete finite difference variations in the horizontal variation of the displacements into six component spherical harmonics, we can easily determine the relative contribution of each spherical harmonic. We do this based on the horizontal variation in the radial displacement. At 120 km s^{-1}, the $l_o = 0$ and 1 modes are still dominated by the $l = 0$ and 1 spherical harmonics, with relative contributions of 89 and 87 % respectively. As illustrated in Figure 4.7, this is enough to slightly distort the mode, but the horizontal variations are still easily recognizable. The contribution from the next most important spherical harmonic is the $l = 2$ (6.1 %) and the $l = 5$ (8.7 %) respectively. At 240 km s^{-1}, one mode still remains easily identifiable as dominant, with relative contributions of 70 % and 59 % for the $l = 0$ and 1 spherical harmonics respectively. The next most important contribution to these two modes comes from the $l = 4$ (13 %) and $l = 7$ (16 %) spherical harmonic, respectively. Although the shapes are now very distorted, (see Figure 4.8,) this is not enough to significantly alter the photometric amplitudes.

Although the photometric amplitude ratio for the $l_o = 1$ mode shows an increased range at 240

Figure 4.7: The horizontal variation of the radial eigenfunction for a model rotating at 120 km s^{-1}. Shown are the $l_o = 0$ (top left), $l_o = 1$ (top right), $l_o = 2$ (bottom left) and $l_o = 3$ (bottom right) modes. The horizontal variation of the radial displacement from our models is shown with a solid line, and for comparison, the pure spherical harmonics are shown with a dashed line. Although the horizontal variations are somewhat distorted, they are still clearly recognizable as the first four spherical harmonics.
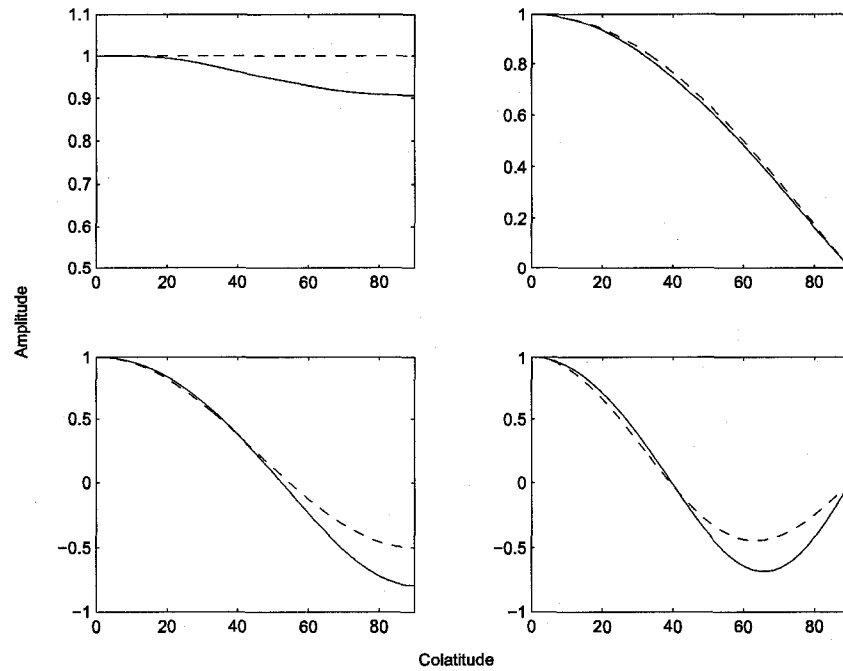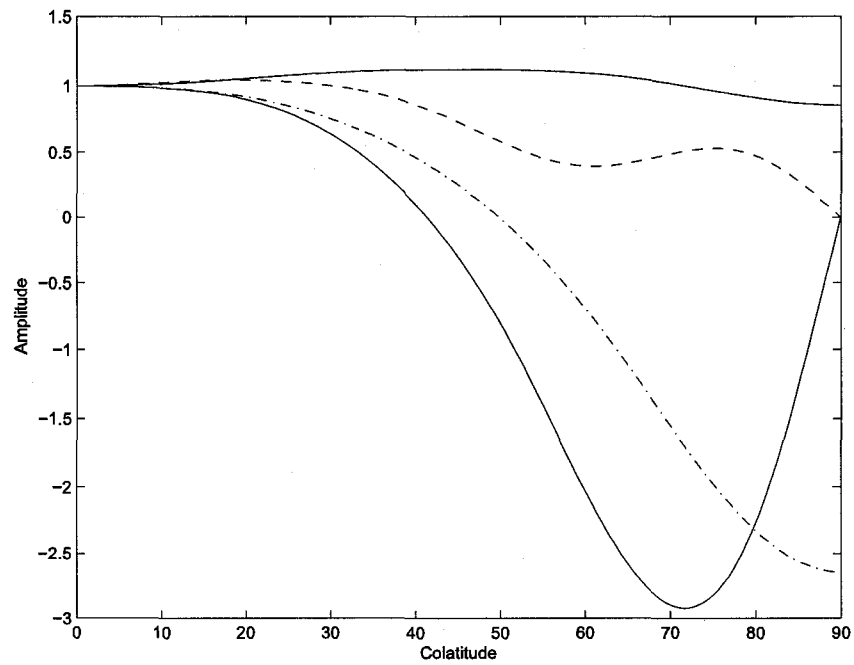
Figure 4.8: The horizontal variation of the radial eigenfunction for a model rotating at 240 km s^{-1}. Shown are the shapes of the $l_o = 0$ (top solid), $l_o = 1$ (dashed), $l_o = 2$ (dot-dashed) and $l_o = 3$ (lower solid) modes. At this velocity, the shapes of the mode are more distorted than at 120 km s^{-1}.

km s^{-1}, the pulsation amplitude is still easily identifiable as produced by an $l_o = 1$ mode, despite the contribution of the $l = 1$ spherical harmonic dropping below 60 %. In an effort to determine how low the contribution must drop before the effects are noticeable in the amplitude ratios, we have also calculated this mode for a model rotating at 360 km s^{-1}. Figure 4.9 shows the amplitude ratios for the $l_o = 1$ mode in the Walraven filter system as a function of increasing rotational velocity. At 360 km s^{-1}, the variation of amplitude with wavelength deviates somewhat from the lower velocity models, but is within the same range. In fact, the variation now looks quite similar to that of the $l_o = 3$ mode at 240 km s^{-1} at high inclination angle (cf. Figure 4.11). Despite the similarities in amplitude ratio, the $l_o = 1$ mode is not dominated by a single spherical harmonic at 360 km s^{-1}. Instead, the mode is composed of nearly equal contributions from the $l = 1$ (19 %), $l = 9$ (26 %) and $l = 11$ (25 %) spherical harmonics, vs. $l = 1$ (51 %), $l = 7$ (21 %) and $l = 3$ (15 %) at 240 km s^{-1}. The contributions of the $l = 5$ and 9 components are also fairly significant, at 10 and 13 % respectively. Clearly, the contribution from the dominant spherical harmonic has to drop significantly before there is a visible effect on photometric amplitudes. Despite the lack of a single dominant spherical harmonic, the combination of spherical harmonics at 360 km s^{-1} still retains the general character of an $l_o = 1$ mode, and this is probably why there is so little difference in the photometric amplitudes.

As with the inclination effects, the situation becomes more complicated when the $l_o = 2$ mode is taken into consideration. In this case, the minimum photometric amplitudes for the 120 km s^{-1} and 240 km s^{-1} models (at $i = 0°$ and $i = 50°$) coincide with the $l_o = 0$ amplitude curves at $i = 90°$. The shape of these curves is also quite similar, leaving us with no obvious technique for discriminating between these two modes. Similarly, the maximum photometric amplitude for the $l_o = 2$ mode overlaps with the $l_o = 1$ mode. In this case, the overlap is not as close as with the $l_o = 0$ mode, and extremely precise photometric observations may be able to distinguish between the two, although this seems unlikely. Nevertheless, the amplitudes of both the $l_o = 0$ and 1 modes remain inside the range of possible amplitudes for the $l_o = 2$ modes (Figure 4.10), and misidentification of the degree of the mode is certainly possible.
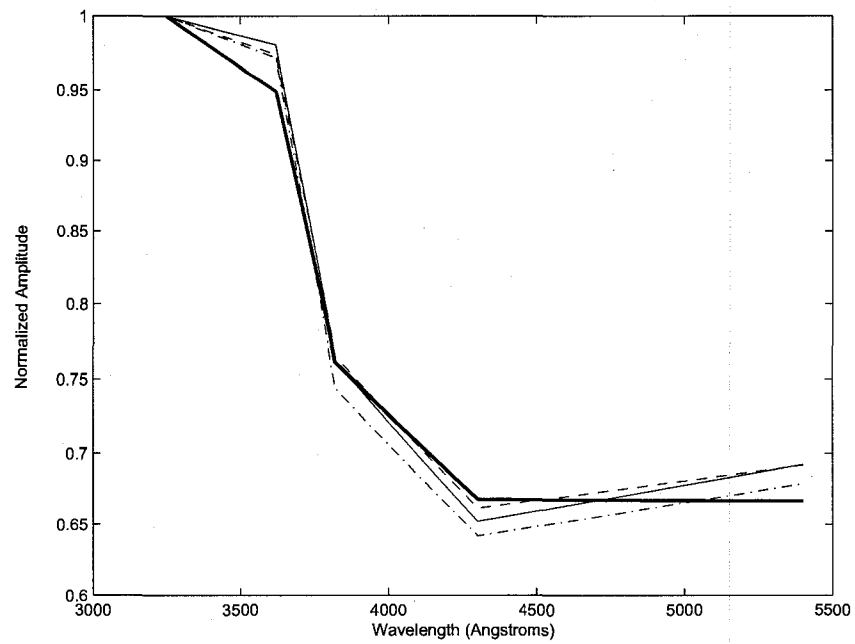
Figure 4.9: Walraven amplitude ratios for the $l_o = 1$ mode for surface equatorial rotation velocities of 0 km s^{-1} (solid), 120 km s^{-1} (dashed), 240 km s^{-1} (dot-dashed) and 360 km s^{-1} (heavy solid). There is a clear progression from 0-240 km s^{-1}, while the 360 km s^{-1} model breaks with the trend and shows a different profile. All of these models are shown at a typical inclination of $i = 50°$.
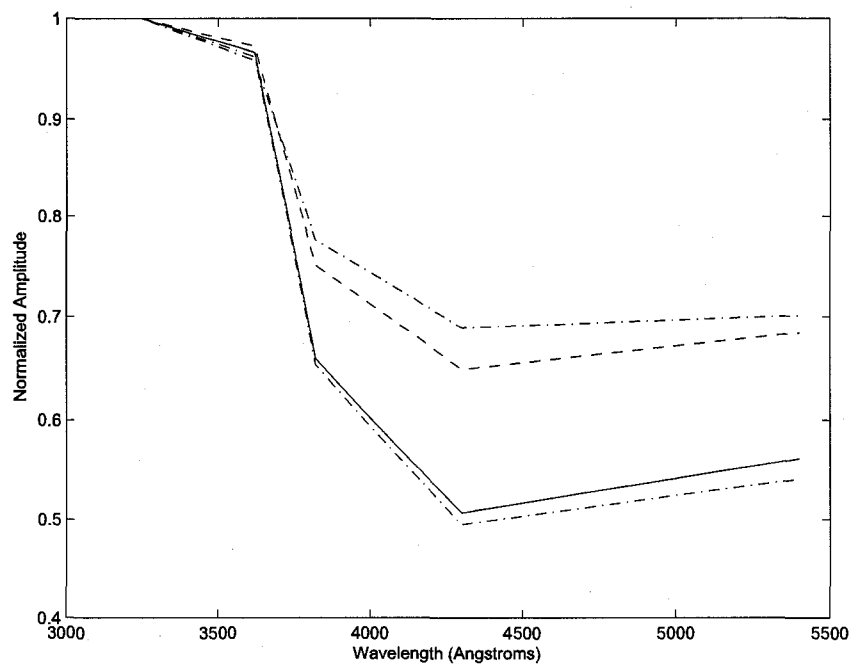
Figure 4.10: The amplitude ratios for the $l_o = 0$ (solid) and 1 (dashed) modes at $i = 50°$ compared to the maximum and minimum for the $l_o = 2$ mode (dot-dashed) at 240 km s^{-1}. The close overlap between these modes makes misidentification using this technique quite possible.
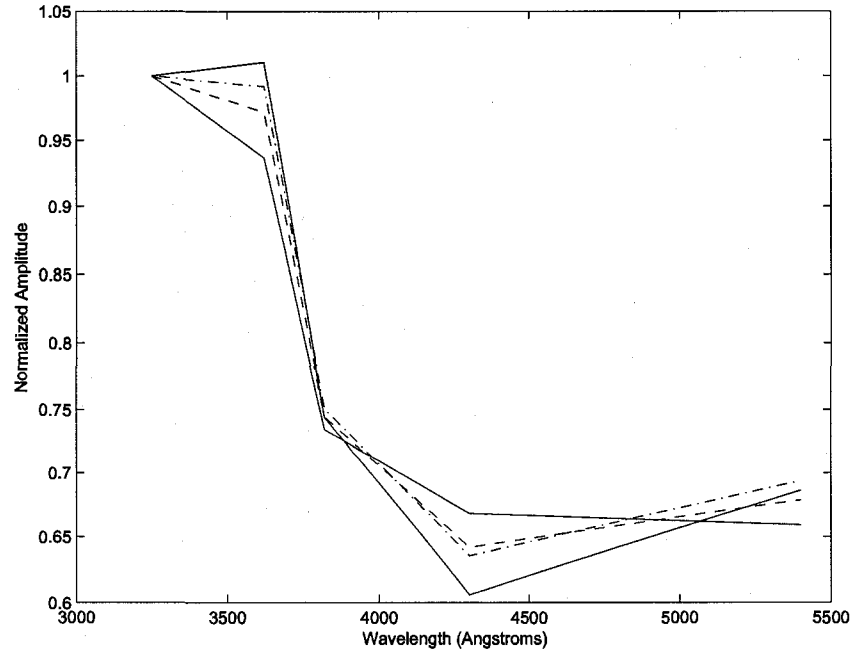
Figure 4.11: The maximum and minimum amplitude ratio for the $l_o = 3$ mode (solid), as well as at $i = 20°$ (dot-dashed) at 240 km s^{-1}. At this rotation speed, the low inclinations begin to mimic the shape of the $l_o = 1$ amplitude ratio (dashed), shown here at $i = 50°$.

The $l_o = 3$ modes also overlap with the $l_o = 0$, 1 and 2 modes, but the shape of these curves appears to be sufficiently different that discrimination is still possible. This is certainly true at 120 km s^{-1}, but may be less so at 240 km s^{-1}. In this case, the $l_o = 3$ mode at low inclinations begins to mimic the $l_o = 1$ mode, as shown in Figure 4.11. The agreement is not exact, but appears somewhat closer than at 120 km s^{-1}.

When the effects of rotation and inclination are considered all together, as in Figure 4.12, the extent to which misinterpretation is probable becomes apparent. As discussed above, the range of photometric amplitudes for the $l_o = 2$ modes neatly brackets the curves for all other modes, and this is the primary source of confusion. The $l_o = 0$ and 1 modes remain distinct from each other, and while the $l_o = 3$ modes are also in the same region, the shape is sufficiently distinct, except at the very highest rotation rates, to avoid confusion.

When rotation and inclination effects are taken into account, we find that there is scope for misidentification of modes, particularly the $l_o = 2$ modes. Unfortunately, due to the large spread
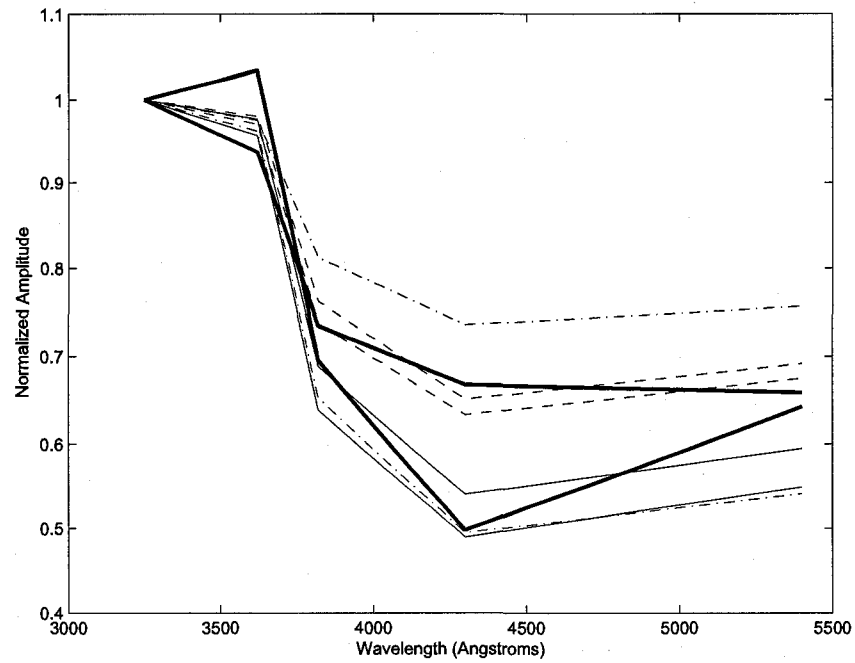
Figure 4.12: The minimum and maximum photometric amplitude in the Walraven filters for each mode over the range of surface equatorial velocity considered here. This shows the largest and smallest amplitude curve for each mode when both rotational and inclination effects are taken into account, so the curves shown are a mixture of rotation rates. Shown are $l_o = 0$ (solid), $l_o = 1$ (dashed), $l_o = 2$ (dot-dashed) and $l_o = 3$ (heavy solid).

in photometric amplitude ratios with inclination in the rotating models, it is virtually impossible to rule this mode out, unless the shape of the mode identifies it as an $l_o = 3$ mode. In the case of a non-rotating star, the spread in photometric amplitude ratio remains small enough for all modes that unambiguous mode identification is possible.

4.5 Higher Order Radial Harmonics

In this paper, we have addressed photometric identification using the variation in photometric amplitude as a function of wavelength. Mode identification can also be performed using other combinations of observables. When mode identification is performed using the photometric amplitude vs. wavelength, it is often assumed that the results are independent of radial order n. Nonadiabatic observables, such as the ratio of color to light amplitude vs. phase, may be able to discriminate between p_1 and p_2 modes, at least in the case of radial modes (Cugier *et al.*, 1994). For non-rotating stars this is a reasonable assumption, as the horizontal variation depends only on l and m. Although the absolute amplitude of the mode varies, when these are normalized the resulting variation as a function of wavelength should be independent of n. For rotating stars this may not be the case. In some cases, particularly for very rapid rotation, the horizontal variation of the mode at a given rotation rate does vary with radial order, and this effect may be reflected in the photometric amplitudes.

To test this, we have calculated photometric amplitudes for the p_1 modes for a model rotating at 120 km s^{-1}. In section 4.4 we showed that increased rotation, and the accompanying distortion in the eigenfunction, produced some spread in the photometric amplitudes. Generally, the modes each retain their distinct character. Therefore, even for the level of distortion seen in Figure 4.13, we expect the effects on the photometric amplitudes to be minimal. The resulting spread is largest for the $l_o = 0$ mode (see Figure 4.14) where the distortion in the horizontal variation is also largest. Although this variation is comparatively large, it is unlikely to result in ambiguity. The model could perhaps be interpreted as rotating more rapidly than it actually is, but the variation is not large enough to overlap with the $l_o = 1$ mode. The variation for the other modes considered here is
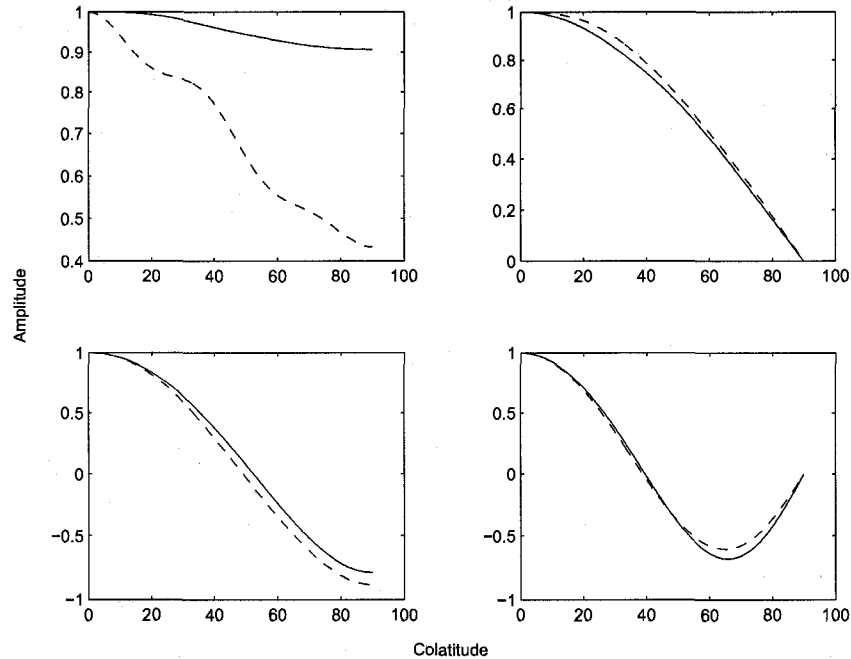
Figure 4.13: Horizontal variation in the radial eigenfunction for the $l_o = 0$ (top left), $l_o = 1$ (top right), $l_o = 2$ (bottom left) and $l_o = 3$ (bottom right) modes in a model rotating at 120 km s^{-1}. Shown are the shapes for the f mode (solid) and p_1 (dashed). Unlike non-rotating models, the horizontal variation depends on n as well as l.

minimal, with the $l_o = 3$ (shown in Figure 4.15) a typical case.

Although the difference in photometric amplitude ratio between the f and p_1 mode is minimal, rotation can impede identification of the radial order of the mode in other ways. Radial order is often determined from the basic properties of the star and an estimate of the fundamental period. However, as discussed in Collins (1966); Hardorp & Strittmatter (1968); Maeder & Peytremann (1970); Linnell & Hubeny (1994); Gillich *et al.* (2008), rotation can change the apparent location in the HR diagram. This may result in large uncertainties in the fundamental parameters of the star if the star is rotating sufficiently rapidly, which in turn may make the identification of the radial order uncertain. Based on the variation of deduced effective temperature and luminosity calculated by Gillich *et al.* (2008), a model rotating at 100 km s^{-1} could produce a difference in the pulsation frequency of the fundamental mode of about 5 % relative to that one would obtain for a spherical model with the same luminosity and effective temperature. At higher rotation rates, where the variation in deduced luminosity and effective temperature is larger, this difference would increase as
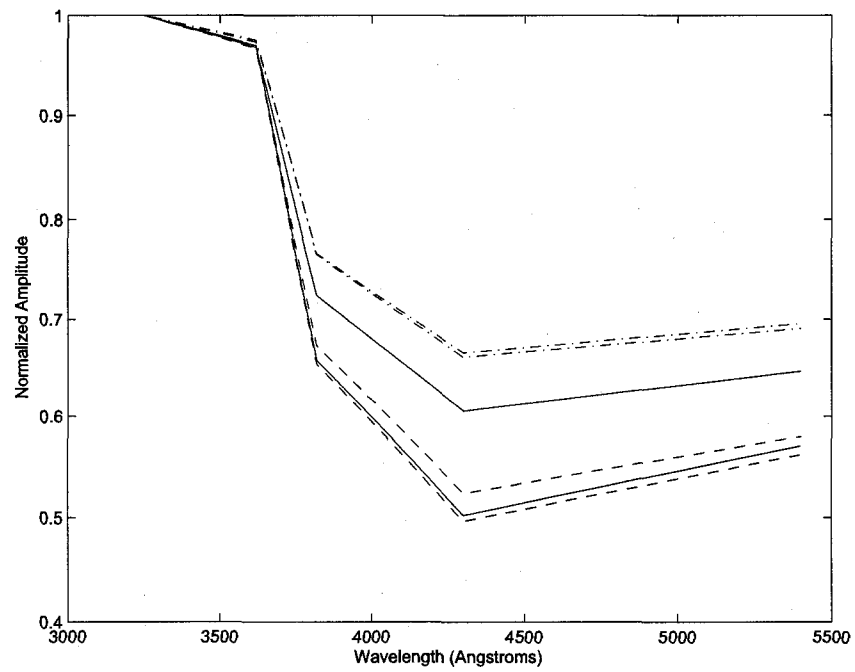
Figure 4.14: The amplitude variation for the $l_o = 0\,p_1$ mode (solid) in a model rotating at $120\,\mathrm{km\ s^{-1}}$ in the Walraven filter system. The dashed lines show the maximum and minimum values for the f mode. The variation in amplitude for the p_1 mode is larger than the f mode. The dot-dashed lines show the amplitude range for the $l_o = 1\,f$ mode.
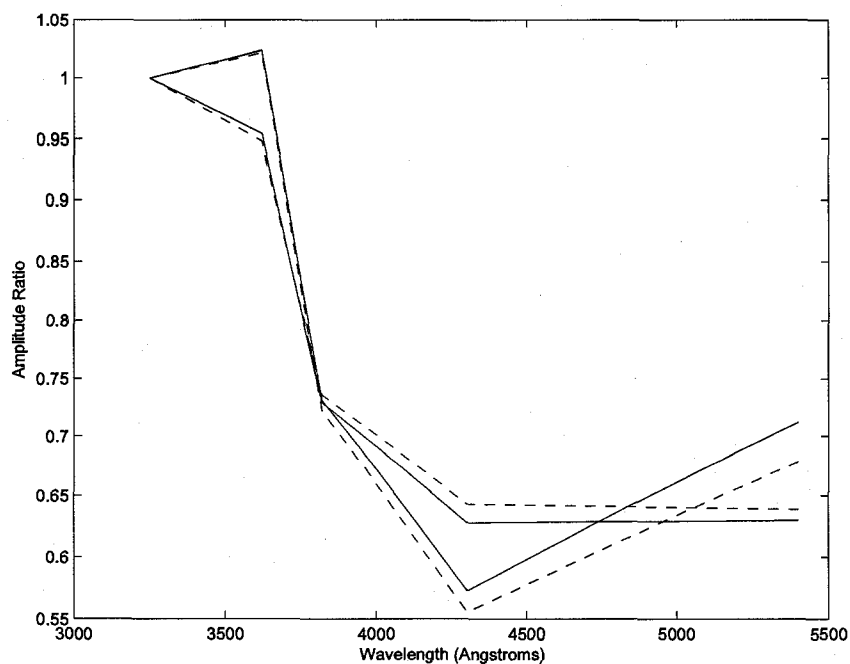
Figure 4.15: The amplitude variation for the $l_o = 3 \ p_1$ mode for a model rotating at 120 km s^{-1}. The dashed lines show the minimum and maximum amplitudes for the f mode in the same model.

well.

4.6 Conclusion

We have found that the spread in photometric amplitude produced by changing inclination is greater than has perhaps been considered previously, although it is not large enough by itself to cause misidentification of the modes in non-rotating stars using the photometric amplitudes. For the $l_o = 0$ and 1 modes, the differences produced by inclination are probably not large enough to be of any concern. The $l_o = 2$ mode produces some variation, but not enough to cause ambiguity in mode identification. The effects for the $l_o = 3$ mode are larger, and cover some of the same range as the $l_o = 0$ and 1 modes. However, the variation of the amplitudes of this mode with wavelength are sufficiently different that the risks of misidentification should be minimal.

Rotation increases the spread in photometric amplitude as a function of inclination so that mode identification becomes compromised. In particular, the amplitude variation in the $l_o = 2$ mode

is large enough that it could be identified as the $l_o = 0$ or 1 modes, depending on the angle of inclination. As with the non-rotating case, the variation of the amplitude with wavelength for the $l_o = 3$ mode follows a different pattern, and this mode should not be confused with other modes at moderate rotation rates. At higher rotation rates (240 km s^{-1}), the $l_o = 3$ mode at low inclinations begins to look like the $l_o = 1$ mode.

We have also considered the effects of rotation on the photometric amplitudes of the p_1 modes in the model rotating at 120 km s^{-1}. Although the horizontal variation of the radial eigenfunction is found to vary with increasing radial quantum number n, the increasing contamination by higher order spherical harmonics is not large enough to significantly affect the photometric mode identification, except in the case of the $l_o = 0$ mode.

Chapter 5

Conclusions

I have investigated the interplay between rotation and stellar pulsation. In Chapter 2 I have shown that six spherical harmonics are needed to accurately calculate eigenfunctions and eigenfrequencies in stellar models rotating at velocities up to 400 km s^{-1} for a 10 M$_\odot$ ZAMS model. Current techniques generally assume that, for slowly rotating models, the eigenfunction can be modelled using a single spherical harmonic. This assumption is expected to be true for slowly rotating stars, and I find that it is, although the exact rotation limit depends on the pulsation mode. For some non-radial modes, one spherical harmonic is sufficient up to at most 165 km s^{-1}, although typically more spherical harmonics are required at rotation velocities of 50-70 km s^{-1}. The eigenfrequencies are somewhat less influenced by rotation, and a single spherical harmonic can be used to calculate pulsation periods up to 180 km s^{-1}, and for some low order modes, the approximation is valid as high as 390 km s^{-1}.

My results show that second order perturbation theory, the most common method for calculating pulsation frequencies in a rotating star is consistent with our results to at least 400 km s^{-1} for low order modes. For higher order modes, perturbation theory and our results diverge at surface equatorial velocities of around 200 km s^{-1}.

The actual behaviour of the eigenfunctions under the influence of rotation is discussed in Chapter 3. I have found that for uniformly rotating models the frequencies decrease as rotation rate is increased, while for differentially rotating models, the frequencies can either increase or decrease with respect to those of uniformly rotating models with increasing differential rotation. For differential rotation, the chage is small, typically around 1% for the most extreme differential rotation models calculated.

I also calculated large and small separations for these models. In some cases, there are indications that it may be possible to use these properties to constrain the internal angular momentum

distribution of the star. However, given the degeneracy of effects from rotation rate and angular momentum distribution, convective overshoot, evolutionary stage, metallicity, etc., it seems unlikely that the very limited pulsation frequencies one expects to be available will give a unique solution.

Constraining the internal angular momentum distribution at all will not be possible without accurate mode identification. One way to do this uses photometric techniques, commonly photometric amplitudes as a function of wavelength. The details of the variation depend on the mode observed, and the variation can be used to identify the l value of a pulsation mode. This assumes that the pulsation mode is a pure spherical harmonic, and as shown in Chapter 2, the exact horizontal shape of the eigenfunction can be quite sensitive to rotation. I have found that the rotational distortion of the eigenfunction has little effect on the photometric amplitudes of the $l_o = 0$ and 1 modes. Unfortunately, the photometric amplitudes of the $l_o = 2$ mode in rotating stars covers a wide range of of values, and this mode can easily be confused with the $l_o = 0$ or 1 mode, even at relatively low rotation. Rotation also causes the photometric amplitudes in the $l_o = 3$ mode to spread over a wide range of values. At slow rotation however, the slope of the variation with wavelength is significantly different from the other modes, so it should still be possible to identify an $l_o = 3$ mode separately, just by the shape. At higher rotation rates, this is no longer true at all inclination angles, and the photometric amplitudes of the $l_o = 3$ mode at low inclinations begins to mimic those of the $l_o = 1$ mode.

If observed modes are to be used to constrain the structure and evolution of rotating stars, we must be able to understand the pulsation characteristics and identify the modes. Unfortunately, the results presented here indicate that understanding pulsation in rotating stars is perhaps even more complicated than previously thought. Although rotation can have a significant effect on the pulstaion frequencies, it is not clear that the changes produced are unique. Photometric mode identification is also complicated by rotation and misidentification of a given mode is likely. These effects all need to be taken into consideration when interpreting observations of rotating stars, but unfortunately they collectively seem to make the situation more complicated.

Although this work has shown some promising hints that pulsation can be used to constrain

stellar rotation, there is still much work to be done in this area. The work shown in Chapter 4 covers only uniformly rotating models. As the horizontal variation in the radial eigenfunctions of the differentially rotating models becomes more complicated at lower rotation rates than the uniformly rotating models, the influence on photometric amplitudes may be greater.

This study has, for the sake of simplicity, been entirely restricted to axisymmetric modes. Observationally, nonaxisymmetric modes have been observed in many stars, and it would be interesting to test our expectation that these results hold for $m \neq 0$. Also, all of these models have been 10 $M_{\odot}$ ZAMS models, which represents the low mass end of the β Cephei range. Although the results presented here are not expected to depend significantly on mass, an extension of this work to other masses is needed to verify this. These 10 $M_{\odot}$ ZAMS models are suitable for a general comparison to β Cephei stars, evolved main sequence models would be more realistic. This would present many challenges, as evolution is known to significantly complicate the pulsation spectrum (see e.g., Daszyńska-Daszkiewicz *et al.*, 2002).

Finally, it is desirable to investigate non-adiabatic effects in these modes with the same level of capability for treating rotation as we have done here for adiabatic modes. Given that these stars have significant variation across the surface, it is thought that certain modes may be driven more strongly in some regions of the star than others. This may result in a rotating star having different amplitudes than it's non-rotating countepart, or perhaps even a completely different pulsation spectrum. The effects related to pulsational instability can only be investigated with a non-adiabatic pulsation code.

To really understand a star, we would ideally know its mass, actual luminosity and effective temperature, composition, rotation rate (v_{eq}), and its angular momentum distribution. Observations will give us the metallicity, acceleration due to gravity, effective temperature, luminosity (a function of distance and inclination), $v \sin i$, and for pulsating stars, a collection of frequencies. If one can determine i, based on these observations, one can find the actual luminosity, as well as the surface equatorial velocity, v_{eq}. In some cases, i can be determined through spectral line fitting, and there are indications that the rotation profile can be determined this way as well, although it is not clear that both can be determined simultaneously. However, for most stars, asteroseismology remains our

most likely tool for determining the inclination i and the angular momentum distribution assuming that the requency spectrum is unique for a given rotation rate. Doing so remains a complex process, governed by the interplay of many different factors. In this work, I have found both some hints that this may be possible, as well as factors which make the process more difficult. Clearly, much further work in this field is needed before we can understand rotating stars as well as we do non-rotating stars.

Bibliography

Antia, H.M. & Basu, S. 2006. ApJ, 644, 1292

Baglin, A., Auvergne, M., Catala, C., Michel , E. & The COROT Team, 1998. ESA Special Publication, 464, 395

Basri, G., Borucki, W. J. & Koch, D. 2005. New Astronomy Rev., 49, 478

Basu, S. & Antia, H.M. 2004. ApJL, 606 L85

Balona, L.A. 1986. MNRAS, 219, 111

Balona, L.A. 1986. MNRAS, 220, 647

Balona, L.A. 1987. MNRAS, 224, 41

Balona, L.A. 1989. Progress in Seismology of the Sun and Stars, Lecture notes in Physics, 367

Balona, L.A. & Evers, E.A. 1999. MNRAS, 302, 349

Belmonte, J.A., *et al.*, IAU Colloq. 137: Inside the Stars, 40, 739

Breger, M. 2007. Comm. Asteroseis., 150, 25

Castor, J.I. 1971. ApJ, 166, 109

Carcofi, A.C., Domiciano de Souza, A., Maghalhães, A.M., Bjorkman, J.E. & Vakili, F. 2008. ApJL, 676, L41

Chandrasekhar, S. 1964. ApJ, 139, 664

Chandrasekhar, S. & Lebovitz, N.R. 1962. ApJ, 135, 248

Christensen-Dalsgaard, J., Gough, D.O. & Thompson, M.J. 1989 MNRAS, 238, 481

Christensen-Dalsgaard, J., Gough, D.O. & Thompson, M.J. 1989 ApJ, 378, 413

Clement, M.J. 1964. ApJ, 140, 1045

Clement, M.J. 1965. ApJ, 141, 210

Clement, M.J. 1969. ApJ, 156, 1051

Clement, M.J. 1972. ApJ, 175, 135

Clement, M.J. 1974. ApJ, 194, 709

Clement, M.J. 1978. ApJ, 222, 967

Clement, M.J. 1979. ApJ, 230, 230

Clement, M.J. 1986. ApJ, 301, 185

Clement, M.J. 1998. ApJS, 116, 57

Collins, G.W. 1963. ApJ, 138, 1134

Collins, G.W. 1966. ApJ, 146, 914

Couvidat. S., García, R.A., Turck-Chiéze, S., Corbard, T., Henney, C.J. & Jiménez-Reyes, S. 2003. ApJL, 597, L77

Cowling, T.G. 1941. MNRAS, 101,367

Cox, J.P. & Giuli, R.T. 1968. New York, Gordon and Breach

Cox, J.P. *Proceedings of the Solar and Stellar Pulsation Conference*, eddited by A.N. Cox & R.G. Deupree (LASL, Los Alamos) p 127.

Cox, J.P. 1980. *Theory of Stellar Pulsation*, Princeton University Press

Cox, J.P. & Stellingwerf, R.F. 1979. PASP, 91, 319

Cugier, H., Dziembowski, W.A. & Pamyatnykh, A.A. 1994. A&A, 291, 143

Daflon, S., Cunha, K., de Araujo, F.X., Wolff, S., Przybilla, N. 2007. AJ, in press [arXiv:astro-ph/0707.3934]

Daszyńska-Daskiewicz, J., Dziembwoski, W.A., Pamyantnykh, A.A. & Goupil, M.-J. 2002. A&A, 392, 151

Daszyńska-Daskiewicz, J. 2008. CoAst, 152, 140

Demarque, P. 1960. ApJ, 132, 366

Demarque, P. 1962. AJ, 67, 270

Demarque, P. Mengel, J.G. & Sweigart, A.V. 1972. ApJ, 173, L27

Deupree, R.G. 1990. ApJ, 439, 357

Deupree, R.G. 1995. ApJ, 357, 175

Deupree, R.G. 1998. ApJ, 499, 340

Domiciano de Souza, A., Kervella, P., Jankov, S., Abe, L., Vakili, F. di Folco, E. & Paresce, F. 2003. A&A, 407, L47

Dupret, M.A. 2001. A&A, 366, 166

Dupret, M.-A., De Ridder, J., Neuforge, C., Aerts, C. & Scuflaire, R. 2002. A&A, 385, 563

Dziembowski, W.A. & Goode, P.R. 1992, ApJ, 394, 670

Dziembowski, W.A., Moskalik, P. & Pamyatnykh, A.A. 1993. MNRAS, 265, 588

Eff-Darwich, A., Korzennik., S.G., & Jiménez-Reye, S.J. 2002, ApJ, 573, 857

Endal, A.S. & Sophia, S. 1976. ApJ, 210, 184

Endal, A.S. & Sophia, S. 1978. ApJ, 220, 279

Endal, A.S. & Sophia, S. 1979. ApJ, 232, 531

Espinosa, F., Pérez Hernández, F. & Roca Cortés, T. 2004. Proceedings of the SOHO 14 GONG 2004 Worshop, ed. D. Danesy, ESA SP-559, 424

Faulkner, J., Roxburgh, I.W. & Strittmatter, P.A. 1968. ApJ, 151, 203

Frémat, Y., Zorec, J., Hubert, A.M. & Flquet, M. 2005. A&A, 440, 305

Frost, E.B. 1902 ApJ, 15, 340

Gillich, A. 2007. MSc Thesis.

Gillich, A., Deupree, R.G., Lovekin, C.C., Short, I. & Toque, N. 2008. ApJ, 683, 441

Hacking, P., *et al.*, 1999. ASP Conf. Ser. 177, 409.

Hardorp, J. & Strittmatter, P.A. 1968. ApJ, 151, 1057

Harris, W.E. & Clement, M.J. 1971. ApJ, 167, 321

Hauschildt, P.H. & Baron, E. 1999. J. Comp. App. Math., 109, 41

Hayashi, C. 1961. Pub. Ast. Soc. Japan, 13, 450

Henyey, L.G., Lelevier, R. & Levée, R.D. 1955. PASP, 67, 154

Heyney, L.G., Forbes, J.E. & Gould, N.L. 1964. ApJ, 139, 306

Heynderickx, D., Waelkens, C. & Smeyers, P. 1994. A&AS, 105, 447

Hurley, M., Roberts, P.H. & Wright, K. 1966. ApJ, 143, 535

Hoyle, F. & Schwarzschild, M. 1955. ApJ, 121, 776

Iben, I. J. 1965. ApJ, 141, 993

Iben, I. J. 1967. ARA&A, 5, 571

Iben, I.J. & Ehrman, J.R. ApJ, 135, 770

Iglesias, C.A., Roger, F.J. & Wilson, B.G. 1987, ApJ, 322, L45

Iglesias, C.A., Roger, F.J. & Wilson, B.G. 1990. ApJ, 360, 221

Iglesias, C.A. & Rogers, F.J. 1996. ApJ, 464, 943

Jackson, S. 1970. ApJ, 161, 579

Jackson, S., MacGregor, K.B. & Skumanich, A. 2005. ApJS, 156, 245

MacGregor, K.B., Jackson, S., Skumanich, A. & Metcalfe, T.S. 2007. ApJ, 663, 560

Johnson, H.L. 1965. Comm. Lunar and Planetary Lab, 53

Kippenhahn, R., Thomas, H.C. & Wiegert, A. 1965. Zeitschrift fur Astrophysik, 61, 241

Kurucz, R.L. 1994. CD-ROM 22, Atomic Data for Fe and Ni (Cambridge: SAO)

Kurucz, R.L. & Bell, B. 1995. CD-ROM 23, Atomic Line List (Cambridge: SAO)

Kushwaha, R.S. 1957. ApJ, 125, 242acro

Lane, J.H. 1870. American Journ. of Sci. and Arts, 2nd series, 4, 57

Lee, U. & Osaki, Y. 1982. PASJ, 34, 39

Lesh, J.R. & Aizenman, M.L. 1978. ARA&A, 16, 215

Lignières, F., Rieutord, M. & Reese, D. 2006. A&A, 455, 607

Linnell, A.P. & Hubeny, I. 1994. ApJ, 434, 738

Lovekin, C.C. 2005. MSc Thesis

Lovekin, C.C., Deupree, R.G. & Short, C.I. 2006. ApJ, 643, 460

Lovekin, C.C. & Deupree, R.G. 2008. ApJ, 679, 1499

Lovekin, C.C. & Deupree, R.G. 2008. Submitted to ApJ.

Maeder, G. & Peytremann, E. 1970. A&A, 7, 120

Michel, E., Baglin, A., Samadi, R., Baudin, F. & Auvergne, M. 2007. Comm. Asteroseis., 150, 341

Monaghan, J.J. & Roxburgh, I.W. 1965. MNRAS, 131, 13

Moro, D. & Mnari, U. 2000. A&AS, 147, 361

Moskalik, P. & Dziembowski, W.A. 1992. A&A, 256, L5

Nather, R.E., Winget, D.E., Clemens, J.C., Hansen, C.J. & Hine, B.P. 1990. ApJ, 361, 309

Ostriker, J.P. & Mark, J.W.-K. 1968. ApJ, 151, 1075

Pekeris, C.L. 1938. ApJ, 89, 188

Pesnell, W.D. 1990. ApJ, 363, 227

Reese, D., Lignières, F. & Rieutord, M. 2006. A&A, 455, 621

Reese, D., Lignières, F. & Rieutord, M. 2008. A&A, 481, 449

Reiners, A. 2003. A&A, 408, 707

Rogers, F.J., Swenson, F.J. & Iglesias, C.A. 1996. ApJ, 456, 902

Roxburgh, I.W. 1964. MNRAS, 128, 157

Roxburgh, I.W., Griffith, J.S. & Sweet, P.A. 1965. ZAp, 61, 203

Sackmann, I-J. & Anand, S.P.S. 1969. ApJ, 155, 257

Sackmann, I-J. & Anand, S.P.S. 1970. ApJ, 162, 105

Saio, H. 1981. ApJ, 244, 299

Saio, H. & Cox, J.P. 1980. ApJ, 236, 549

Schou, J. *et al.*1998. ApJ, 505, 390

Schwarzschild, M. 1947. ApJ, 106, 427

Schwarzschild, M. & Härm, R. 1958. ApJ, 128, 348

Short, C.I., Hauschildt, P.H. & Baron, E. 1999. ApJ, 525, 375

Short, C.I. & Hauschildt, P.H. 2005. ApJ, 618, 926

Slettebak, A. 1949. ApJ, 110, 498

Smith, R.C. 1971. MNRAS, 151, 463

Soriano, M. & Vauclair, S. 2008. A&A, in press (arXiv:astro-ph/0806.0235)

Soufi, F., Goupil, M.J. & Dziembowski, W.A. 1998. ApJ, 334, 911

Suran, M.D. 2007. Ap&SS, 457

Stamford, P.A. & Watson, R.D. 1981, Ap&SS, 77, 131

Stankov, A. & Handler, G. 2005. ApJS, 158, 193

Stellingwerf, R.F. 1978. AJ, 83, 1184

Stellingwerf, R.F. 1979. ApJ, 227, 935

Sterken, C., Jerzykiewicz, M. & Manfroid, J. 1986. A&A, 169, 166

Stoeckley, T.R. 1968. MNRAS, 140, 141

Stoeckley, T.R. & Buscombe, W. 1987. MNRAS, 227, 801

Strömgen, B. 1956. Vistas in Astronomy, 2, 1336

Sweet, P.A. & Roy, A.E. 1953. MNRAS, 113, 701

Tassoul, J.-L. *Theory of Rotating Stars*, Princeton University Press, 1978.

Tassoul, M. 1980. ApJS, 43, 469

Tassoul, J.-L. *Stellar Rotation*, Cambridge University Press, 2000.

Thompson, M.J., Christensen-Dalsgaard, J., Miesch, M.S. & Tommre, J. 2003. ARA&A, 41, 599

Ulrich, R.K. 1986. ApJ, 306, L37

von Zeipel, H. 1924. MNRAS, 84, 665

Walker, G., *et al.*, 2003. PASP, 115, 1023

Walraven, T., & Walraven, J. H. 1960. Bull. Astron. Inst. Netherlands, 15, 67

Watson, R.D. 1988. Ap&SS, 140, 255

Yoshida, S. & Eriguchi, Y. 2001. MNRAS, 322, 389

Zahn, J.-P. 1992. A&A, 265, 115